A MECHANICAL INVESTIGATION OF FLAPPING-WING FLIGHT THROUGH REDUCED-ORDER MODELING

by

Joseph Elsmere Reade

A dissertation submitted in partial fulfillment
of the requirements for the degree

of

Doctor of Philosophy

in

Mechanical Engineering

MONTANA STATE UNIVERSITY
Bozeman, Montana

July 2024

©COPYRIGHT

by

Joseph Elsmere Reade

2024

All Rights Reserved

TABLE OF CONTENTS

1. INTRODUCTION 1

2. DEFORMABLE BLADE ELEMENT AND UNSTEADY VORTEX LATTICE FLUID-STRUCTURE INTERACTION MODELING OF A 2D FLAPPING WING 6

Contribution of Authors and Co-Authors 6
Manuscript Information 7
Introduction 8
Theory 10
Structural Model 10
Deformable Blade Element Model 11
Unsteady Vortex Lattice Fluid Model 12
Simulation 13
Simulation Parameters 13
Model Comparison 13
Conclusion 16

3. INVESTIGATION OF CHORDWISE FUNCTIONALLY GRADED FLEXURAL RIGIDITY IN FLAPPING WINGS USING A TWO-DIMENSIONAL PITCH-PLUNGE MODEL 18

Contribution of Authors and Co-Authors 18
Manuscript Information 19
Introduction 20
Theory 21
Structural Model 21
Fluid Model 22
Force moments and power 24
Numerical Simulation 25
Results 25
Natural frequencies & mode shapes 26
Flapping with hovering kinematics 28
Deviations from hovering kinematics 28
Pitch amplitude 28
Plunge amplitude 30
Pitch-plunge phase 30
Discussion 31
Optimal lift production 31
Trade-offs between power & force 31

TABLE OF CONTENTS – CONTINUED

Implications for robotics 32
Computational economy and model assumptions 32
Conclusion 33

4. QUASI-3D DEFORMABLE BLADE ELEMENT AND UNSTEADY VORTEX LATTICE REDUCED-ORDER MODELING OF FLUID-STRUCTURE INTERACTION IN FLAPPING WINGS 38

Contribution of Authors and Co-Authors 38
Manuscript Information 39
Introduction 41
Mathematical Modeling 42
Flapping Kinematics 42
Reduced-Order Modeling 43
High-Fidelity Computational Model 45
Numerical Simulation Parameters 46
Results 48
Parametric Study 52
Discussion 53
Computational Efficiency 53
Application of ROMs 53
ROM Limitations 53

5. REDUCED-ORDER MODELING AND OPTIMIZATION OF A FLAPPING-WING FLIGHT SYSTEM 56

Contribution of Authors and Co-Authors 56
Manuscript Information 57
Introduction 59
Methods 61
Structural Modeling 61
Fluid Modeling 63
Implementation and Optimization 64
Simulation Parameters 64
Optimization 65
Results 67
Parameter Trends 67
Energetic Losses 68
Frequency Response 72
Discussion 75

TABLE OF CONTENTS – CONTINUED

Biological Comparison 76
Multimodal Excitation 79
Energy Recycling 81
FWMAV Design 81

6. CONCLUSION 93

REFERENCES CITED 97

LIST OF TABLES

Table Page

2.1 Physical properties of the wing used for simulation 13

2.2 Flapping Kinematics Parameters 13

2.3 DBET Simulation Parameters 14

2.4 UVLM Simulation Parameters 14

2.5 Influence of wing flexibility on mean vertical force for both fluid solvers 15

3.1 Wing parameters 25

3.2 Peak deflection, mean lift, mean power and peak leading edge force for various taper ratios assuming normal flapping kinematics. Rigid wing is assumed to have uniform thickness 28

3.3 Discretization Parameters 36

4.1 Wing parameters 47

4.2 DBET and UVLM simulation parameters. 47

4.3 High-fidelity modeling parameters. 48

5.1 SLM fixed parameters 64

5.2 UVLM simulation parameters 65

5.3 Evolved parameters and bounds 65

5.4 Optimization constraints 67

5.5 Selected individuals 73

5.6 Nonlinear resonant frequency 75

5.7 Genetic algorithm parameters 92

LIST OF FIGURES

Figure Page

2.1 Diagram of flexible wing undergoing prescribed rigid body pitching (θ) and plunging (Z) 10

2.2 Free body diagram of differential aerodynamic forces acting at the location of dm for DBET model. Wing shown in undeformed configuration 11

2.3 Schematic of panel for UVLM fluid model. d_{bv} and d_{cp} are the distance of the bound vortex and control point from the panel leading edge,respectively. ds is panel width 12

2.4 Convergence study for the DBET fluid model showing the dependence of the solution on number of blade elements. the y-axis shows the maximum wingtip deflection for the current parameters as a fraction of the maximum wingtip deflection at convergence 14

2.5 Convergence study for the UVLM fluid model showing the dependence of the solution (top) on number panels and (bottom) number of wakes. The y-axis shows the maximum wingtip deflection for the current parameters as a fraction of the maximum wingtip deflection at convergence 14

2.6 Aerodynamic normal force $\boldsymbol{F}_N$ for a rigid wing predicted by BET and UVLM solvers 15

2.7 (Top) Wingtip deflection and (Bottom) aerodynamic normal force $\boldsymbol{F}_N$ for a flexible wing predicted by BET and UVLM solvers 15

3.1 (A) Reference frames and pitch-plunge motion, (B) Free-body diagram of forces acting on the wing and gravity vector to show orientation. Cartesian grad applies to both panels. The black circle in both panels indicates where the wing would meet insect body 23

3.2 Wing discretization used by UVLM 24

LIST OF FIGURES – CONTINUED

Figure Page

3.3 Wing discretization with exponential thickness distribution. Nodes 2, ..., N_e+1 may experience vertical displacement and rotation, while the leading-edge node is clamped. Wing thickness is exaggerated 25

3.4 First natural frequency (solid line) and frequency ratio (dashed line) as a function of chordwise wing taper. Approximate airfoils indicating the taper are shown at the bottom of the figure, with taper ratios of 0.2, 0.6, and 1 from left to right. Flapping frequency is assumed to be 25 Hz 26

3.5 The bending mode used to calculate wing deflection. Mode shapes presented in this plot are normalized by the maximum value at the trailing edge 26

3.6 Comparison of lift, power, leading edge force, and wing tip deflection for several taper ratios using kinematics in Table 3.1. 27

3.7 Study of pitch amplitude. The flexible and rigid wing values are represented by the solid and dashed lines, respectively 29

3.8 Study of plunge amplitude. The flexible and rigid wing values are represented by the solid and dashed lines, respectively 29

3.9 Study of pitch-plunge phase offset. The flexible and rigid wing values are represented by the solid and dashed lines, respectively 31

3.10 Dependence of mean lift, mean power and peak deflection on chordwise panel discretization. The red line indicates the number of panels used in this work 34

3.11 Dependence of mean lift, mean power and peak deflection on time step discretization. The red line indicates the number of panels used in this work 35

3.12 Dependence of the wing's first natural frequency on the number of elements. The red line indicates the number of elements used in this work 35

3.13 Lift coefficient over a single wing beat 36

LIST OF FIGURES – CONTINUED

Figure Page

4.1 Development of an $x - y - z$ coordinate system that rotates with the wing's rigid body motion. $\mathbf{R}$ is a position vector between the wing's fixed point of rotation O and a differential mass dm. Per our coordinate system convention, gravity g acts in the $-X$ direction. 43

4.2 Free-body diagram showing differential aerodynamic forces acting upon an individual blade element. 44

4.3 Panel discretization used by the 2D UVLM solver. 45

4.4 Background mesh (outlined) and overset mesh (light gray) of the fluid domain in Star-CCM+. The rectangular wing is seen in the dark gray within the overset mesh. The wing-fixed coordinate system is shown in pink, with an origin at the wing root's leading edge. The background mesh must be large enough to accommodate flapping kinematics and encompass pertinent flow features, while the overset mesh must accommodate the out-of-plane deformation of the wing. 46

4.5 Bilaterally coupled workflow between Abaqus FEA and Star-CCM+. This cycle continues at every time step described by CFD. 46

4.6 Geometry and vibration modes of the rectangular wing used in numerical simulation. The first mode represents a chordwise-bending mode, and the second represents a chord-wise torsional mode. Red indicates positive out-of-plane motion, green indicates no motion and black indicates negative out-of-plane motion. Mode shapes are arbitrary in magnitude, which is why a colorbar is omitted. 47

4.7 Deflection of the wing's trailing edge at tip and root locations along the wing's span. 49

4.8 Contour map showing out-of-plane deformation of the flexible wing as a function of wingbeat period T. 49

LIST OF FIGURES – CONTINUED

Figure Page

4.9 Aerodynamic forces predicted by each model with respect to the wing-fixed reference frame. UVLM and DBET models do not resolve spanwise flow, so no F_y component is shown for these models. 50

4.10 Aerodynamic moments predicted by each model with respect to the wing-fixed reference frame. 51

4.11 Aerodynamic forces predicted by each model with respect to the inertial reference frame. Gravity acts in the +X direction. 51

4.12 Parameter study showing the effect of wing flexibility (parameterized by the wing's first natural frequency) and mass on peak deflection, mean lift, and average power. The corresponding time-series data for lift and deflection is shown for the 60 mg wing at natural frequencies of 40, 55, and 73 Hz in Figs. 7 and 11. 52

5.1 System-level model configuration. Note that only one wing is explicitly modeled, and the other is accounted for via symmetry arguments. XYZ denotes a globally fixed Cartesian coordinate system and xyz denotes a wing-fixed Cartesian reference frame. 62

5.2 Population results for evolved parameters. Clockwise from top left: pitching stiffness k_ϕ, transmission ratio λ, thorax force amplitude $F_{T,0}$, thorax stiffness k_T. Red dots indicate individual solutions. Colored background is relative density of solutions 69

5.3 Angular equivalent of evolved parameters. Left: angular stiffness k_θ. Right: applied moment amplitude $M_{\theta,0}$. Red dots indicate individual solutions. Colored background is relative density of solutions 69

5.4 (Left) Population distribution, efficiency vs braking power percent of total power. Red dots indicate individual solutions, colored background is relative density of solutions. (Right) Braking power percent of total power, relative to phase delay between thorax velocity and applied load. 70

LIST OF FIGURES – CONTINUED

Figure Page

5.5 Efficiency vs aerodynamic power P_{aero} as a percentage of the total input power P_{in}. Red dots indicate individual solutions, colored background is relative density of solutions 71

5.6 (Left) Energetic efficiency as a function of kinematic amplitudes, and (Right) of aerodynamic power and roll-pitch phase..... 72

5.7 Relation between maximum kinematic responses and flapping frequency (left) and non-dimensional flapping frequency (right). Vertical black line on the left indicates the flapping frequency used in the GA 74

5.8 Mean lift production (top) and efficiency (bottom) as a function of flapping frequency, dimensional (left) and non-dimensional (right). Vertical black line on the left indicates the flapping frequency used in the GA..... 76

5.9 Hawkmoth wing kinematics in hovering flight for (a) roll (stroke angle) and (b) pitch (called AoR in the comparison study). Dashed blue indicates data from the SLM for 'common' moth, set over results from ([Zheng et al., 2013]). To account for upstroke-downstroke asymmetry, SLM data has been translated vertically so that the mean lies midway between the extrema of the experimental data. In (b), the angle from ([Zheng et al., 2013]) is given at three spanwise locations due to wing twist, denoted 0.4R, 0.6R and 0.8R, where R is the wing length 77

5.10 Roll-pitch phase as a function of the linear natural frequencies (left) and natural frequency ratio and flapping frequency ratio (right). Each dot is a member of the population discussed in section **??**..... 80

5.11 Discretization of a blade into panels. Top section shows bound vortex and control point placement on a panel. 88

ABSTRACT

Micro air vehicles are a class of unmanned aerial vehicle far smaller than conventional vehicles. Due to their maneuverability and small form-factor, these craft show great promise in a myriad of applications, ranging from artificial pollination to mapping cave systems to search-and-rescue. When established platforms like multirotors are reduced down to these sizes, aerodynamic scaling effects has a deleterious impact on vehicle performance.

To overcome this, we turn to insect flight for inspiration. Flying insects utilize flapping wings to achieve flight, and do so efficiently. Capable of migrating huge distances and performing advanced aerobatics, insects have many adaptations that help them fly. Highly-flexible wings yield aerodynamic and energetic benefits while reducing the reducing the weight the insect needs to carry. Potential energy storage in the thorax enables them to recoup effort spent driving their wings, and fly farther.

Despite the benefits afforded by flapping wings, they are still not fully understood. Study of flapping-wing flight is challenging owing to the high-speed, large-amplitude wing motion and aeroelastic deformation of the wings, making measurement of aerodynamic forces difficult. Computational methods allow us to overcome these obstacles. High-fidelity modeling enables accurate prediction of the airflow and pressures acting on the wing, and of the fluid-structure interaction present, however the large computational cost makes them unsuited for parametric studies.

In this work, a reduced-order model is developed to study the fluid-structure interaction in flexible flapping wing systems. Bulk aerodynamic forces are accurately predicted with short solutions times, enabling parametric studies to be conducted. The effect of variable rigidity is investigated in 2D and 3D wings, and results compared to high-fidelity methods. Thorax dynamics are added in order to study elastic energy recycling. We find that moderate levels of wing flexibility improve the performance of flapping wings by lowering the energetic requirements, and that optimized system parameters can reduce power consumption through elastic energy recycling and resonance excitation.

1

INTRODUCTION

Micro air vehicles (MAVs) are a type of unmanned aerial vehicle (UAV) notable for their reduced size [Kurtulus, 2011]. In addition to retaining the benefits of regular UAVs over traditional manned aircraft, the small size of MAVs opens of a number of potential applications [Ward et al., 2017]. Chiefly, operation in congested/constrained environments, such as leak detection in refineries or agricultural and environmental monitoring [Abdullah et al., 2021; Chen and Li, 2019]. The compactness and low cost also enables them to be rapidly deployed in large numbers, a strong advantage when time is critical, such as in search-and-rescue in ruined urban environments after natural disasters [Gao et al., 2024].

MAVs face several design challenges, especially at smaller sizes [Pines and Bohorquez, 2006]. At low length scales and velocities, conventional airfoils perform poorly due the scale effect. At the higher Reynolds numbers, or ratio of inertial forces to viscous forces, where conventional aircraft operate, airflow over the top of the wing is turbulent, and resistant to large-scale separation [Winslow et al., 2018; Traub and Coffman, 2019]. In the flight regime inhabited by MAVs, particularly for the applications described, the flow over the airfoil is largely laminar and low energy, making it more likely to separate over large areas of the wing. This reduces lift and increases drag, lowering the efficiency and lifting capability of the wing.

Flying insects, first appearing over 300 million years ago [Goldsworthy and Wheeler, 1989], are capable of remarkable feats, considering their size and simplicity. Despite flapping flight being possibly the most energetically costly form of locomotion [Neville, 1965], insects are capable of traveling vast distances. Swarms of desert locust (*Schistocerca gregaria*) can travel 150 km in a day, and have flown for 20 continuous hours over water, utilizing air

currents to extend their range [Cressman, 2016]. Furthermore, many flying insects are highly maneuverable [Greeter and Hedrick, 2016]. To achieve this flight performance, insects have evolved a number of adaptations. Insect wings are typically quite flexible. Not only does this reduce the overall weight, but flexible wings have been shown to reduce energy requirements, and potentially outperform rigid wings in force production [Mountcastle and Combes, 2013; Lang et al., 2022; Vanella et al., 2009]. Wing flexibility impacts the leading-edge vortex (LEV) [Addo-Akoto et al., 2021], a flow structure present in flapping wing flight which aids in lift-generation [Ellington et al., 1996]. Many insects utilize indirect flight muscles (IFMs) to drive the flapping motion of their wings [Dickinson and Tu, 1997; Fernandes et al., 1991; Kobayashi and Ishikawa, 1993]. Rather than pulling on the wing directly, these muscles attach to the walls of the thoracic exoskeleton and exist in opposing pairs. The IFMs compress the thorax cyclically, and this deformation is transmitted through the wing hinge into the wing. The hinge allows small deformations in the thorax to produce large-amplitude rotations, generating the flapping motion and aerodynamic forces required for flight [Hollenbeck and Palazotto, 2013]. An insect's thoracic exoskeleton behaves as a spring, storing elastic potential energy when it is deformed. Throughout the flapping cycle, energy is stored elastically in the compressed thorax, decelerating the wing, and released back into the system at stroke reversal to re-accelerate the wing. As with wing flexibility, the thorax compliance reduces the overall energetic requirement of flight placed on the insect [Gau et al., 2019a]. Additionally, insects are believed to flap near resonant frequencies of the system, utilizing the magnification at resonance to further decrease the effort required to generate the flapping kinematics.

In the development of MAVs, scientists and engineers look to insect flight for inspiration. The flapping-wing micro air vehicle (FWMAV) is a subclass of MAV that appropriately uses flapping wings to generate the aerodynamic forces, lift and thrust, to sustain flight. By using flapping wing and relying on different aerodynamic phenomena, FWMAVs can avoid the

scaling problems that are faced by fixed-wing craft operating at low Reynolds numbers. In addition to increased vehicle performance, flexible flapping wings can increase vehicle safety and durability. Conventional multirotors rely on rigid sharp-edged propellers spinning at thousands of revolutions per minute [Nguyen et al., 2020b]. These pose a risk to nearby people, and are likely to sustain damage in the event of a collision. Asymmetric damage may require replacement of the rotor as mass imbalances combined with high RPM lead to vibration [Ghalamchi et al., 2019]. Small rotor-craft intended for operation in confined spaces will often have additional structure surrounding the blades or the entire craft [Edgerton et al., 2019]. Such as structure adds additional weight and may decrease thrust efficiency. In contrast, a flexible flapping wing is better able to bend out the way when colliding with an obstacle, and is less likely to splinter into fragments than a propeller rotating at high-speed. FWMAVs are inherently less dangerous in a collision [Zufferey et al., 2021; Silva and Bueno, 2024], being less likely to sustain damage and being safer to nearby people. FWMAVS are an area of active research and development [Wood et al., 2013; Ryu and Kim, 2017], and many of the above characteristics have led to FWMAVs being studies as potential candidates for extra-planetary exploration, e.g. on Mars where the low-density atmosphere results on very low Reynolds numbers [Bluman et al., 2017]. While they have clear advantages, the development and adoption of FWMAV platforms is hampered by several design challenges. One such hurdle is the complex physics involved. The flexibility of the wing means it deforms under aerodynamic and inertial loading, and the deformed shape of the wing affects how the air flows around it. This fluid-structure interaction (FSI) complicates the multiphysics problem. Unlike fixed-wing aircraft, and to a lesser extent rotor-craft, the flow around flapping wings is highly unsteady.

Studying flapping wings via physical experimentation is made difficult by several factors. The high-speed large-amplitude rotation makes actuation difficult. Physical testing in fluid flows where the velocity or length scales would be an issue are often dynamically

scaled, sometimes changing the working fluid so lower velocities can be used. However, when considering flexible structures, dynamic scaling cannot be done in the same way. Changing the fluid density to maintain the Reynolds number at low velocities will alter the relative significance of aerodynamic and inertial loads in deforming the wing, impacting results. Computational study is often more practical, but still faces difficulties. In many cases, analysis of fixed-wing aircraft and rotor-craft can assume steady or quasi-steady flow, greatly reducing the effort and time required to reach a solution. In flapping wing flight, a significant portion of the force production may be due to unsteady effects such as vortex-shedding [Ellington, 1984]. Simulating multiple wingbeats to develop the flow is computationally expensive, but may be necessary. In the case of flexible wings, deformation may significantly alter the aerodynamics, requiring further computational effort. Despite these issues, numerical methods have been used successfully to study flapping wings [Zuo et al., 2007; Maeda et al., 2010]. High-fidelity methods are popular, chiefly computational fluid dynamics (CFD), to estimate aerodynamic performance, as unsteady and viscous effects are accounted for. In the case of a flexible wing where the deformation is unknown *a priori*, finite element analysis (FEA) is used to estimate wing deflection, which may be one-way or two-way coupled with the fluid solver. While these methods are often considered the gold-standard for computational study, the extremely long times need to reach a solution make them infeasible for use cases requiring either fast results or a large number of simulations, such as parametric or optimization studies. For this reason, researchers often turn to reduced-order models (ROMs) to study flapping wing flight [Long and Fritz, 2004; Fitzgerald et al., 2011]. In reduced-order models, the problem complexity is reduced by identifying physics and variables that have negligible impact on the relevant results. These components are removed from the method while retaining the most essential features, lowering computational complexity and cost without sacrificing accuracy unduly [Fernandez-Escudero et al., 2019; Valdez et al., 2020]. Because the importance of different physical phenomena is dependent

on the problem at hand, a ROM will not be as widely applicable as the high-fidelity methods discussed earlier [Kou and Zhang, 2016]. The vastly increased speeds attainable by ROMs, however, make them an attractive tool, and they have been widely used in the study of flapping wing flight.

This dissertation focuses on the use of reduced-order modeling to study flapping wings, both rigid and flexible. The impact of system flexibility on energetics and force production are examined through parametric studies. The results help further our understanding of flapping wing flight and may aid in design principles for the development of FWMAV platforms. Reduced-order models are confirmed as a valuable tool in investigating flapping wing flight, and exploring the design space for FWMAVs, accelerating the development process by reducing the reliance on more costly high-fidelity methods.

6

DEFORMABLE BLADE ELEMENT AND UNSTEADY VORTEX LATTICE FLUID-STRUCTURE INTERACTION MODELING OF A 2D FLAPPING WING

Contribution of Authors and Co-Authors

Manuscript in following chapter

Author: Joseph Reade

Contributions: Development of vortex lattice model

Author: Mark Jankauski

Contributions: Development of blade element model and structural model

Manuscript Information

J. Reade, M. Jankauski

International Design Engineering Technical Conferences

Status of Manuscript:
____ Prepared for submission to a peer-reviewed journal
____ Officially submitted to a peer-reviewed journal
____ Accepted by a peer-reviewed journal
_X_ Published in a peer-reviewed journal

ASME
December 2019
Volume 141, Issue 6
DOI: 10.1115/DETC2020-22638

Proceedings of the ASME 2020 International Design Engineering Technical Conferences & Computers and Information in Engineering Conference
IDETC/CIE 2020
August 16-19, 2020, St. Louis, USA

IDETC2020-16019

DEFORMABLE BLADE ELEMENT AND UNSTEADY VORTEX LATTICE FLUID-STRUCTURE INTERACTION MODELING OF A 2D FLAPPING WING

Joseph Reade
Graduate Researcher
josephreade.school@gmail.com

Mark A. Jankauski
Assistant Professor
mark.jankauski@montana.edu

ABSTRACT

Flapping insect wings experience appreciable deformation due to aerodynamic and inertial forces. This deformation is believed to benefit the insect's aerodynamic force production as well as energetic efficiency. However, the fluid-structure interaction (FSI) models used to estimate wing deformations are often computationally demanding and are therefore challenged by parametric studies. Here, we develop a simple FSI model of a flapping wing idealized as a two-dimensional pitching-plunging airfoil. Using the Lagrangian formulation, we derive the reduced-order structural framework governing wing's elastic deformation. We consider two fluid models: quasi-steady Deformable Blade Element Theory (DBET) and Unsteady Vortex Lattice Method (UVLM). DBET is computationally economical but does not provide insight into the flow structure surrounding the wing, whereas UVLM approximates flows but requires more time to solve. For simple flapping kinematics, DBET and UVLM produce similar estimates of the aerodynamic force normal to the surface of a rigid wing. More importantly, when the wing is permitted to deform, DBET and UVLM agree well in predicting wingtip deflection and aerodynamic normal force. The most notable difference between the model predictions is a roughly 20° phase difference in normal force. DBET estimates wing deformation and force production approximately 15 times faster than UVLM for the parameters considered, and both models solve in under a minute when considering 15 flapping periods. Moving forward, we will benchmark both low-order models with respect to high fidelity computational fluid dynamics coupled to finite element analysis, and assess the agreement between DBET and UVLM over a broader range of flapping kinematics.

INTRODUCTION

Over the past decade, flying insects have become a popular model organism for bio-inspired flapping wing micro air vehicles (FWMAVs) [1]. Unlike rotor based aircraft, which suffer inefficiencies that preclude their flight at reduced length scales and low Reynolds numbers, FWMAVs can scale down almost indefinitely due to the unsteady aerodynamic mechanisms enabled by their flapping wings [2]. This makes FWMAVs a desirable platform for tasks that require the vehicle to operate in congested environments, for example infrastructure monitoring of piping networks. Nonetheless, while researchers have developed successful insect-scale FWMAVs, there remain several design challenges that must be overcome before such vehicles are suitable for widespread applications. Some of these challenges include reducing energetic expenditures, implementing reliable on-board control systems and improving aircraft durability. A better understanding of insect flight, in particular the flapping wing, can guide engineering design to surmount many of these challenges.

As an insect wing flaps, it deforms from both aerodynamic and inertial forces [3]. Wing deformation has been shown to provide numerous advantages to flight, including improving aerodynamic force production [4] and reducing energetic costs [5]. In some insects, wing deformation provides a sensing modality as well. Hawkmoth *Manduca sexta* wings are imbued with mechanoreceptors called campaniform sensilla, and recent studies show the feedback encoded by these receptors facilitate the insect's attitude control system [6]. The insect wing may therefore behave both as a sensor and an actuator in some contexts. Despite the significance of wing flexibility to flapping wing flight, however, the mathematical models used to predict flap-

Copyright © 2020 by ASME

ping wing fluid-structure interaction (FSI) remain limited.

The most common flapping FSI models utilize finite element analysis (FEA) coupled to computational fluid dynamics (CFD) to estimate wing deformation and to resolve the flow field surrounding the flexible structure [7–9]. While such models are instrumental to improving the knowledge of flexible wing dynamics, they are often computationally inefficient, sometimes taking hours or days to solve. With respect to FEA, the periodic rotations of the wing give rise to centrifugal softening, which cause the structural stiffness matrix to become time-varying [10, 11]. As a result, the stiffness matrix must be updated at each interval of analysis, which in turn increases the time required to solve for wing deformation. With respect to CFD, upwards of tens of thousands of equations must be solved to resolve the entire flow field surrounding a flapping wing [12]. Moreover, the CFD mesh must generally be restructured as the wing passes through it. Clearly, both fluid and structural solvers require considerable computational resources, and these computational requirements become nearly intractable when fluid and structure are coupled.

To reduce these computational requirements, the flapping wing is often simplified to a two-dimensional problem. A flapping wing in two dimensions emulates a pitching, plunging airfoil, where the length of the airfoil is the mean chord width of the insect wing. While some of the physics associated with flapping in three-dimensions are lost, the two-dimensional pitch-plunge model has been used to garner many insights into flapping wing flight. Yin and Luo utilized a 2D FSI model to study the effect of wing inertial forces on deformation and the resulting aerodynamic forces during hover [13]. Tian et al. extended this work to address the influence of wing flexibility during forward flight [14]. Sridhar and Kang used a 2D FSI model to investigate energy expenditures in flapping fruit flies [15]. Despite the two-dimensional idealization, however, these FSI models are still computationally expensive because of their reliance on CFD and FEA. Studies investigating broad ranges of wing kinematics, flexibility or other parameters may be challenged by these high-order methods depending on the desired number of variables considered.

To enable parametric studies of flapping wings, many researchers have turned to more efficient structural and fluid modeling. While modal reduction is almost exclusively used to reduce the demands of the structural solver [10, 11, 16], the fluid models employed to supplement CFD are more varied. The two most common tend to be based upon blade element theory (BET) and unsteady vortex lattice method (UVLM). BET functions by discretizing a wing into chord-wise airfoils, or "blade elements". Differential forces are estimated via airfoil theory for each blade element and are summed over the entire to wing to estimate total aerodynamic forces. While BET is among the most widely used models for flapping wing flight, it is typically restricted to rigid wings with only a handful of exceptions. Wang et al. developed an economical flapping wing FSI model using a blade element aerodynamic approach, however their model permits only wing twisting and not bending [17]. Schwab et al. developed and experimentally validated a BET-based FSI model, however it was applicable only to single-degree-of-freedom flapping that did not generate lift [18, 19]. This model was later extended to 3D kinematics, but considered only unilateral coupling between fluid and structure [20]. Thus, it remains to be seen if BET can concurrently model bilateral fluid-structure coupling as well as lift-generating 2D flapping.

The other common reduced-order fluid model is UVLM. UVLM is a numerical method that discretizes the wing into panels, each to which a vortex is bound. By estimating the strength of each bound and shed vortex, one can estimate the pressure distribution over a wing. Fitzgerald et al. derived a UVLM-based 2D flapping FSI model, and found that UVLM made flow predictions similar to those made by direct numerical simulation for the deforming wing [21]. They utilized a structural model composed of two rigid links connected by a torsional spring. Mountcastle and Daniel utilized a similar 2D UVLM FSI model with additional links to determine the effect of structural flexibility on flapping wing lift generation [22]. They found that the additional force generation attributed to wing flexibility was sensitive to the relative phase of pitch and plunge. Despite the success of UVLM in flapping wing FSI models, it still requires more computational time relative to BET. It is presently unknown if BET and UVLM produce similar results when modeling flexible wings.

Based upon this literature review, there remains a need for a 2D pitch-plunge flapping wing FSI model that (1) is reduced order to facilitate broad parametric studies and (2) able to accommodate arbitrary planar geometries with spatially varying properties. The objective of the present work is to develop this model. We put forward two candidate approaches – the first based on BET, which we refer to as deformable blade element theory (DBET) owing to its capacity to account for deformation, and the second based on UVLM, which is typically considered a higher-fidelity fluid solver relative to BET. This manuscript presents the first effort towards a tiered "family of models" for flexible pitching-plunging airfoils. Moving forward, we intend to benchmark both of these reduced-order FSI models with respect to high-fidelity, high computational demand CFD. This "family of models" approach will illustrate the trade-offs between solution accuracy and economy within the context of 2D flapping wing FSI.

The remainder of the paper is organized as follows. First, we derive the equation of motion governing the wing dynamics via the Lagrangian formulation. We then outline the DBET and UVLM fluid models used to estimate aerodynamic forces acting on the flexible wing. Next, compare the two models and how they predict wing deformation and aerodynamic force production. We conclude by discussing the implications and future directions of our modeling efforts.

Copyright © 2020 by ASME

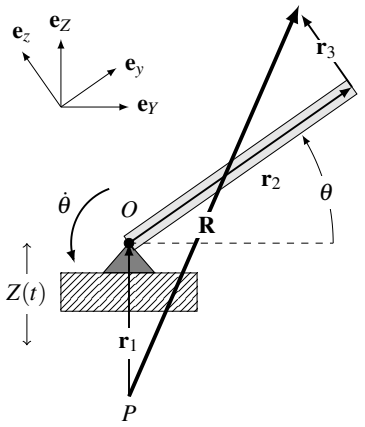


FIGURE 1. Diagram of flexible wing undergoing prescribed rigid body pitching (θ) and plunging (Z).

THEORY

Here, we derive a mathematical model to predict the elastic deformation of a pitching, plunging flexible wing. We first define the rigid body kinematics of the wing, and determine the equation of motion governing the deflection of the wing via the Lagrangian formulation. We then describe the DBET and UVLM fluid models used to estimate fluid loading on the wing surface and to calculate aerodynamic forces.

Structural Model

First, we establish a rotating, translating coordinate frame that moves with the rigid body motion of the wing (Fig. 1). Consider a fixed point P and a translating point O about which the wing is free to rotate. We define O as the origin of the wing-bound reference frame. The displacement of O is described by the prescribed plunging motion of the wing $Z(t)$. Then, the reference frame bound to O is subjected to a positive counter-clockwise rotation by a pitching angle $\theta(t)$. The resulting $x-y-z$ reference frame has an angular velocity $\mathbf{\Omega}$ defined by

$$\mathbf{\Omega} = \dot{\theta}\mathbf{e}_x \tag{1}$$

Within the $x-y-z$ frame, we draw a position vector $\mathbf{R}$ from fixed point P to a differential mass element dm located on the flexible wing. $\mathbf{R}$ is the sum of three intermediate position vectors such that $\mathbf{R} = \mathbf{r}_1 + \mathbf{r}_2 + \mathbf{r}_3$, where

$$\mathbf{r}_1 = Z(t)\,\mathbf{e}_Z = Z(t)[\sin\theta\,\mathbf{e}_y + \cos\theta\,\mathbf{e}_z] \tag{2}$$
$$\mathbf{r}_2 = y\,\mathbf{e}_y; \quad 0 \le y \le c \tag{3}$$
$$\mathbf{r}_3 = W(y,t)\,\mathbf{e}_z \tag{4}$$

Above, $\mathbf{r}_1$ denotes to the prescribed vertical plunging of the rotational pivot point O, $\mathbf{r}_2$ denotes the y position of dm along the flexible wing between zero and max chord-width c, and $\mathbf{r}_3$ denotes an infinitesimal out-of-plane elastic deflection dependent on both space and time. The velocity of the differential mass with respect to the rotating coordinate frame is

$$\dot{\mathbf{R}} = \mathbf{\Omega}\times\mathbf{R} + \dot{\mathbf{r}}_1 + \dot{\mathbf{r}}_3 \tag{5}$$
$$\dot{\mathbf{R}} = [\dot{Z}\sin\theta - W\dot{\theta}]\,\mathbf{e}_y + [\dot{Z}\cos\theta + y\dot{\theta} + \dot{W}]\,\mathbf{e}_z \tag{6}$$

We also determine the acceleration of the differential mass as

$$\begin{aligned}\ddot{\mathbf{R}} = (\ddot{Z}\sin\theta - 2\dot{W}\dot{\theta} - W\ddot{\theta} - y\dot{\theta}^2)\mathbf{e}_y \\ \cdots + (\ddot{Z}\cos\theta + y\ddot{\theta} - W\dot{\theta}^2 + \ddot{W})\mathbf{e}_z\end{aligned} \tag{7}$$

Note that $\ddot{\mathbf{R}}$ is not required to formulate the equation of motion governing wing deformation, however it needed later to approximate the added mass fluid loading. Next, we discretize out-of-plane deflection W via an eigenfunction expansion of vibration mode shapes $\phi_k(y)$ multiplied by modal responses $q_k(t)$, or

$$W(y,t) = \sum_{k=1}^{\infty} \phi_k(y) q_k(t) \tag{8}$$

where vibration mode shapes are normalized with respect to the wing's mass to satisfy orthonormal conditions. We then formulate wing's potential and kinetic energies, which are required to employ the Lagrangian approach. Note that only a high-level derivation is provided here; for further detail on the equation of motion derivation, please refer to Appendix A. The kinetic energy T of the flexible wing is

$$T = \frac{1}{2}\int_m \dot{\mathbf{R}}\cdot\dot{\mathbf{R}}\,dm \tag{9}$$

where Eqs. 6 and 8 are substituted into the above expression to give the explicit form of T. The potential energy U of the wing is

$$U = \frac{1}{2}\int_V S(W,W)\,dV \tag{10}$$

where V is the volumetric domain of integration, and S is a symmetric, quadratic strain energy density function. Using the Lagrangian approach, we determine the Equation of Motion (EoM) governing the unknown modal response q_k as

$$\ddot{q}_k + (\omega_k^2 - \dot{\theta}^2)q_k = -\lambda_k\ddot{Z}\cos\theta - \psi_k\ddot{\theta} + Q_k \tag{11}$$

Copyright © 2020 by ASME

where Q_k is the non-conservative aerodynamic force projected onto the wing's kth mode, ω_k is the wing's kth natural frequency and λ_k, ψ_k are constants defined by

$$\lambda_k = \int_m \phi_k \, dm \tag{12}$$

$$\psi_k = \int_m y \, \phi_k \, dm \tag{13}$$

The non-conservative aerodynamic modal force is determined through the principle of virtual work, where the virtual work $\delta\mathcal{W}$ is

$$\delta\mathcal{W} = Q_k \delta q_k \tag{14}$$

$$Q_k \delta q_k = \int_S \mathbf{F}_N \cdot \delta W \mathbf{e}_z \, dS = \int_S \mathbf{F}_N \cdot \sum_{k=1}^{\infty} \phi_k \delta q_k \, \mathbf{e}_z \, dS \tag{15}$$

$$Q_k = \int_S \phi_k \mathbf{F}_N \cdot \mathbf{e}_z \, dS \tag{16}$$

where $\mathbf{F}_N$ is the physical aerodynamic force, S is the surface over which the aerodynamic force acts, and all quantities preceded by a δ are virtual quantities. Note that $\mathbf{F}_N$ is general and may be obtained through a number of suitable fluid models, including CFD. For the purposes of this work, we consider DBET and UVLM fluid models because the computational resources required to resolve $\mathbf{F}_N$ are minimal compared to CFD.

Deformable Blade Element Fluid Model

To formulate the DBET fluid model (Fig. 2), we assume a generic aerodynamic force per unit area $dF_{aero,[\cdot]}$ can be represented as

$$dF_{aero,[\cdot]} = \frac{1}{2} C_{[\cdot]} \rho_f \dot{\mathbf{R}} \cdot \dot{\mathbf{R}} \, dS \tag{17}$$

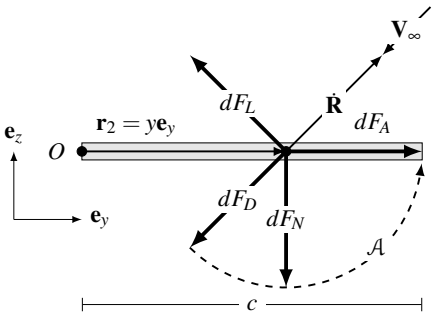


FIGURE 2. Free body diagram of differential aerodynamic forces acting at the location of dm for DBET fluid model. Wing shown in undeformed configuration.

where ρ_f is fluid density, $C_{[\cdot]}$ is an empirical aerodynamic coefficient, $[\cdot]$ is a placeholder to indicate lift of drag, and dS is the differential surface over which the force acts. For the 2D case, $dS = h\,dy$, where h is the wing span (out the page, along the x direction) and dy is a differential length in the chord-wise y direction. The aerodynamic angle-of-attack $\mathcal{A}$ is defined as the angle between the induced flow velocity $\mathbf{V}_\infty$ (equal in magnitude and opposite in direction to $\dot{\mathbf{R}}$ assuming no free-stream flow) and the positive y axis, and can be written as

$$\mathcal{A} = \tan^{-1}\left(\frac{-\dot{\mathbf{R}} \cdot \mathbf{e}_z}{-\dot{\mathbf{R}} \cdot \mathbf{e}_y}\right) = \tan^{-1}\left(\frac{\dot{Z}\cos\theta + y\dot{\theta} + \dot{W}}{\dot{Z}\sin\theta - W\dot{\theta}}\right) \tag{18}$$

As indicated by the above, $\mathcal{A}$ varies along the chord and depends on both the wing's rigid body motion and elastic deformation. The form of aerodynamic lift/drag coefficients in Eq. 17 is taken from [23] as

$$C_L(\mathcal{A}) = C_{L_{max}} \sin(2\mathcal{A}) \tag{19}$$

$$C_D(\mathcal{A}) = \frac{C_{D_{max}} + C_{D_0}}{2} - \frac{C_{D_{max}} - C_{D_0}}{2} \cos(2\mathcal{A}) \tag{20}$$

where $C_{L_{max}}$, $C_{D_{max}}$ and C_{D_0} are empirically fit from experimental or computational methods. Then, expanding Eq. 17 and integrating over the wing surface gives

$$F_{R,[\cdot]} = \frac{1}{2}\rho_f C_{[\cdot]} \int_S (\dot{Z}^2 + 2\dot{Z}\dot{\theta} y \cos\theta + y^2\dot{\theta}^2)\, dS \tag{21}$$

$$F_{E,[\cdot]} = \rho_f C_{[\cdot]} \int_S (-\dot{Z}\dot{\theta}\sin\theta W + [\dot{Z}\cos\theta + \dot{\theta} y]\dot{W})\, dS \tag{22}$$

where F_R and F_E are the rigid and elastic components of $F_{aero,[\cdot]}$ respectively. Note the terms of $\mathcal{O}(W^2)$ are neglected from F_E given that W is infinitesimal. We then rotate lift and drag forces by $\mathcal{A}$ to determine the aerodynamic axial force $\mathbf{F}_A$ and normal force $\mathbf{F}_N$ as

$$\mathbf{F}_A = (F_D \cos\mathcal{A} - F_L \cos\mathcal{A})\langle \mathbf{e}_y \rangle \tag{23}$$

$$\mathbf{F}_N = (F_D \sin\mathcal{A} + F_L \cos\mathcal{A})\langle -\mathbf{e}_z \rangle \tag{24}$$

In addition to lift and drag forces, we must also consider the normal force imparted to the wing by added mass. The air mass accelerated as the wing flaps may be considerable compared to the mass of the wing itself. This imparts an additional force normal to the wing that is proportional to the wing's acceleration. Added mass normal to the wing, denoted $\mathbf{F}_{N,AM}$ and modified from [24], can be represented for the flapping wing as

Copyright © 2020 by ASME

$$\mathbf{F}_{N,AM} = -\pi\rho_f \left(\frac{c}{4}\right) \int_S \ddot{\mathbf{R}} \cdot \mathbf{e}_z \, dS \, \langle \mathbf{e}_z \rangle \tag{25}$$

As with lift and drag, it is possible to represent $\mathbf{F}_{N,AM}$ as rigid and elastic components:

$$\mathbf{F}_{N,AM,rigid} = -\pi\rho_f \left(\frac{c}{4}\right) \int_S (\ddot{Z}\cos\theta + y\ddot{\theta}) \, dS \langle \mathbf{e}_z \rangle \tag{26}$$

$$\mathbf{F}_{N,AM,elastic} = -\pi\rho_f \left(\frac{c}{4}\right) \int_S (-W\dot{\theta}^2 + \ddot{W}) \, dS \langle \mathbf{e}_z \rangle \tag{27}$$

Finally, we combine the aerodynamic normal force $\mathbf{F}_N$ with the fluid force due to added mass $\mathbf{F}_{N,AM}$ and substitute them into Eq. 16 to estimate the non-conservative forces acting on the wing.

Unsteady Vortex Lattice Fluid Model

To employ UVLM (Fig. 3), we assume the flow to be incompressible throughout, and irrotational except on the surface of the wing and in the wake shed from the trailing edge. Using this approach, unsteady effects such as added mass may be accounted for. The wing is discretized into N_p panels of differential length $ds = c/N_p$, with the leading edge of the first panel at O. On each panel, a bound vortex is placed $0.25ds$ aft of the leading edge, and the control point (Cp) is located at $0.75ds$ aft the leading edge [25].

The no-penetration condition states that across the wing surface, the flow velocity component that is normal to the surface must be zero [26], which implies

$$(-\dot{\mathbf{R}} + \mathbf{V}_{BV} + \mathbf{V}_W) \cdot \mathbf{n} = 0 \tag{28}$$

where $\mathbf{V}_{BV}$ is the velocity induced by the bound vortices on the wing, $\mathbf{V}_W$ is the velocity induced by the free wake vortices and $\mathbf{n}$ is the surface normal vector. In this lumped vortex method, this boundary condition is satisfied at the control point of each panel. Enforcing this boundary condition at each control point gives the strength of the bound vortices. Then, the Kelvin-Helmholtz theorem states that the circulation Γ around a closed curve must remain constant, which leads to

$$\frac{D\Gamma}{Dt} = 0 \tag{29}$$

Since the initial vorticity is zero, the total bound vorticity and wake vorticity will sum to zero every time step. This condition sets the strength of the newly created wake vortex, and means that the strength of the free vortices remain unchanged [21].

The velocity at point i induced by a vortex at point j, $\mathbf{V}_{ind_{i,j}}$, is given by the Biot-Savart law:

$$\mathbf{V}_{ind_{i,j}} = \frac{\Gamma_j}{2\pi L^2} \langle (Z_j - Z_i)\mathbf{e}_Y + (Y_i - Y_j)\mathbf{e}_Z \rangle \tag{30}$$

where L is the scalar distance between i and j, and Y, Z are the coordinate locations of i and j in the $Y-Z$ plane. The bound vortex strength Γ_i of each panel and the new wake vortex $\Gamma_{(Np+1)}$ are found by simultaneously enforcing the boundary condition at each control point [27], or

$$\begin{bmatrix} a_{1,1} & a_{1,2} & \dots & a_{1,Np} & a_{1,Np+1} \\ a_{2,1} & a_{2,2} & \dots & a_{2,Np} & a_{2,Np+1} \\ \vdots & \vdots & \ddots & \vdots & \vdots \\ a_{Np,1} & a_{Np,2} & \dots & a_{Np,Np} & a_{Np,Np+1} \\ 1 & 1 & 1 & 1 & 1 \end{bmatrix} \begin{bmatrix} \Gamma_1 \\ \Gamma_2 \\ \vdots \\ \Gamma_{Np} \\ \Gamma_{Np+1} \end{bmatrix} = \begin{bmatrix} \text{rhs}_1 \\ \text{rhs}_2 \\ \vdots \\ \text{rhs}_{Np} \\ \text{rhs}^* \end{bmatrix} \tag{31}$$

where $a_{i,j}$ is the component of velocity at the i^{th} control point induced by the unit-strength j^{th} bound vortex that is normal to panel i. This influence coefficient is found using the Biot-Savart law above substituting 1 for Γ_j. The right-had side, rhs_i is the normal component of velocity at the control point due to flapping kinematics and the wake vortices. rhs^* is the sum of the bound vortices on the wing from the previous time step. Γ_{Np+1} is the strength of the newly shed vortex wake, equal to the negative of the change in total bound vorticity from the previous time step.

If we assume the wake convects with the local flow, the velocity of the i^{th} wake $\mathbf{V}_{W,i}$ is the sum of the velocities induced by the wing-bound vortices and the wake vortices, written as

$$\mathbf{V}_{W,i} = \sum_{j=1}^{N_p} \mathbf{V}_{ind_{i,j}} + \sum_{m=1}^{N_p} \mathbf{V}_{ind_{im}}; \;\; m \neq i \tag{32}$$

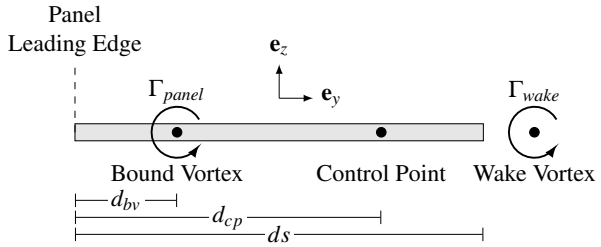


FIGURE 3. Schematic of panel for UVLM fluid model. d_{bv} and d_{cp} are the distance of the bound vortex and control point from the panel leading edge, respectively. ds is panel width.

Copyright © 2020 by ASME

The newly formed wake is placed $0.05c$ with respect to the wing's trailing edge. Next, to determine the pressure differential across the i^{th} panel, ΔP_i, we employ the unsteady Bernoulli equation

$$\Delta P_i = -\rho_f \left[(-\dot{\mathbf{R}} + \mathbf{V}_W)_i \cdot \tau_i \frac{\Gamma_i}{ds} + \frac{\partial}{\partial t} \sum_{j=1}^{i} \Gamma_j \right] \tag{33}$$

where τ_i is the unit vector tangent to the i^{th} panel, and a positive ΔP indicates lower pressure on the upper surface of the wing. Finally, the fluid normal force acting on the i^{th} panel, $\mathbf{F}_{N_i}$ is

$$\mathbf{F}_{N_i} = \Delta P_i \, c \, ds (\mathbf{n}_i \cdot \mathbf{e}_z) \mathbf{e}_z \tag{34}$$

Equation 34 is then substituted into Eq. 16 to determine the generalized aerodynamic modal force.

SIMULATION

In this section, we compare the results of the two flapping wing FSI models. We first establish the wing's properties and prescribed kinematics based off known values for the Hawkmoth *Manduca sexta*, a common model organism in the study of insect flight. We then analyze the wing tip deflection and aerodynamic forces predicted by both models.

Simulation Parameters

The physical properties of the wing are given in Tab. 1. The chord width, span, thickness were estimated for the Hawkmoth from [28]. We adjust the Young's modulus within the biological values presented in [28] until we achieve a natural frequency of 80 Hz, which is corresponds to the torsional mode of the Hawkmoth wing [29]. The damping ratio is also taken from this source. We treat the wing as a homogenous beam with fixed-free boundary conditions, and thus determine its natural frequency and mass-normalized mode shape analytically using well-known expressions from [30]. However, we stress that this formulation permits material and geometry properties to vary along the wing's y direction. For sake of simplicity, we retain only one vibration mode.

Next, we prescribe the rigid body kinematics of the flapping wing. We note that flapping wings undergo three-dimensional rotation in practice, and that the kinematics presented here are an idealization. We assume that the both pitching and plunging motions are harmonic and out-of-phase by $\frac{\pi}{2}$ radians. The plunging motion represents the large, sweeping flapping rotation of the wing – we are essentially projecting the wing's stroke plane onto a two-dimensional space when employing the pitch-plunge model. The pitching has a similar interpretation in both 2D and 3D models. All flapping kinematics are summarized in Tab. 2. Rotation/translation amplitudes are similar to those presented in [13], whereas the flapping frequency is taken from [31]. We use a lower pitch amplitude than is typically observed in Hawkmoth flight [31]. This is because pitch measurements from flying insects, particularly those that experience large wing twisting, invariably contain some rotation arising from rigid body rotation and elastic deformation. How the rigid body rotation and elastic deformation sum to net wing pitch is challenging to delineate from experimental measurements in free-flying insects.

TABLE 1. Physical properties of the wing used for simulation.

Symbol	Description	Value	Units
E	Young's Modulus	24.5	GPa
c	Chord Width	2	cm
h	Span	5	cm
t	Thickness	40	μm
M_w	Mass	40	μg
ω_1	First Natural Frequency	80	Hz
ζ_1	First Modal Damping Ratio	0.05	-

TABLE 2. Flapping Kinematics Parameters.

Symbol	Description	Value	Units
Z_0	Plunge Amplitude	2	cm
θ_0	Pitch Amplitude	15	$^\circ$
ϕ_z	Plunge Phase Advance	90	$^\circ$
ω	Flapping Frequency	25	Hz

We now establish the simulation parameters used for both fluid models. In both cases, we use a time step that corresponds to 200 intervals per wingbeat period (0.2 ms) and allow the simulation to run for 15 periods, which we determined was an adequate duration to achieve steady-state in all cases considered. Reducing the time step further did not impact the solution.

We then verify that the numerical methods have converged. First, consider the DBET model. The solution accuracy, as well as the time required to solve, are dependent on the number of blade elements the structure is discretized into. To ensure that the solution has converged, we vary the number of blade elements and record the maximum wing tip deflection. Then, we plot the wingtip displacement normalized by the converged wingtip displacement with respect to the number of elements (Fig. 4). The solution converges quickly, with less than a 1%

Copyright © 2020 by ASME

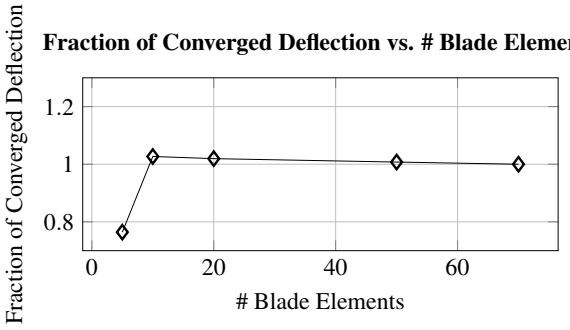


FIGURE 4. Convergence study for the DBET fluid model showing the dependence of the solution on number of blade elements. The y-axis shows the maximum wingtip deflection for the current parameters as a fraction of the maximum wingtip deflection at convergence.

change when increasing the total element count beyond 5. While this rapid convergence can greatly expedite the time required to solve the DBET model, it is worth noting that wings with non-homogeneous material or geometric properties will require more elements to resolve.

Next, consider the UVLM model. We determined that the solution was most sensitive to the number of panels and wakes considered. We maintain the number of wakes at 200 and vary the panel count from 5 to 70, and then maintain the number of panels at 50 and vary the wake count from 5 to 300. We again plot the normalized wingtip displacement as a function of these parameters (Fig. 5). In both cases, the solution converges relatively quickly, with the solution being modestly more sensitive to the number of wakes considered.

With these simple convergence studies completed, we define the remaining parameters needed to carry out numerical simulations for both models. DBET parameters are shown in Tab. 3, where the aerodynamic coefficients are similar to those in [23]. UVLM parameters are shown in Tab. 3.

TABLE 3. DBET Simulation Parameters.

Symbol	Description	Value
C_{D_0}	Drag offset coefficient	0.4
$C_{D_{max}}$	Maximum drag coefficient	4.0
$C_{L_{max}}$	Maximum lift coefficient	1.8
N	Number of blade elements	50

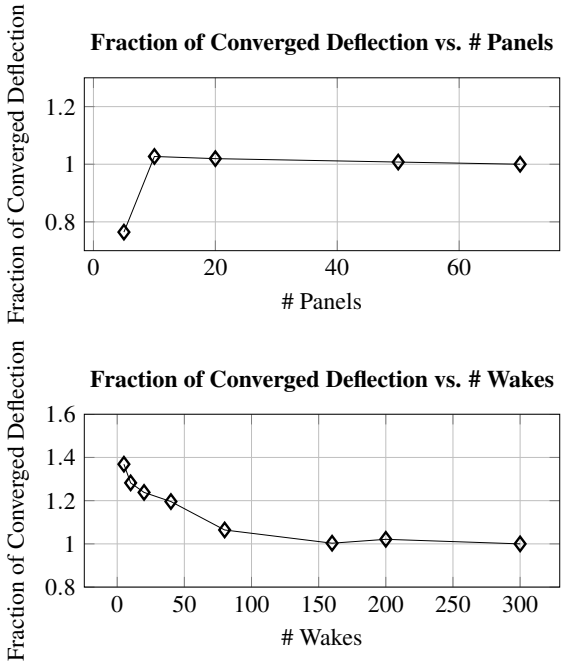


FIGURE 5. Convergence study for the UVLM fluid model showing the dependence of the solution on (top) number of panels and (bottom) number of wakes. The y-axis shows the maximum wingtip deflection for the current parameters as a fraction of the maximum wingtip deflection at convergence.

TABLE 4. UVLM Simulation Parameters.

Symbol	Description	Value
N_w	Number of wakes	200
N_p	Number of panels	50
d_{cp}	Control point distance from leading edge as % of panel length	75
d_{bv}	Bound vortex distance from leading edge as % of panel length	25

Model Comparison

We first compare BET and UVLM fluid models for a rigid wing to provide a baseline and to assess how well the two agree before flexibility is incorporated. The aerodynamic normal force $\mathbf{F}_N$ predicted by both fluid models is shown as a function of a single wingbeat in Fig. 6. In general, the two models agree well both in terms of magnitude and phase. UVLM predicts a larger normal

Copyright © 2020 by ASME

force magnitude and leads the BET prediction in phase. These discrepancies are relatively minor, which suggests the simulation parameters provide a good basis for the fluid models, at least when the wing is rigid.

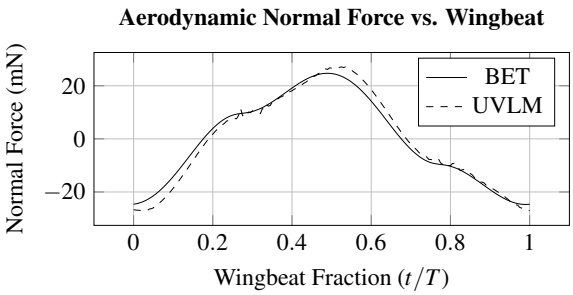


FIGURE 6. Aerodynamic normal force $\mathbf{F}_N$ for a rigid wing predicted by BET and UVLM solvers.

Then, we permit the wing to deform under inertial and aerodynamic loads. Recall that both FSI models utilize the same structural framework, and therefore any differences in the wing's response between the two models stem from differences in the fluid models. We plot both the wingtip (at $y = c$) deflection as well as aerodynamic normal forces for the flexible wing over a wingbeat period in Fig. 7. DBET and UVLM models predict wingtip deflections similarly, with maximum deflections of approximately 7.5 mm occurring just after the stroke reversal around $t/T = 0.33, 0.83$. DBET predicts a larger 3ω component of wingtip response as well as a phase lag relative to UVLM. This phase discrepancy is more appreciable in the aerodynamic normal force, where the DBET normal force lags the UVLM normal force by approximately 18°. While the phase discrepancy appears small, we point out that even minor phase changes can significantly affect aerodynamic force production in the inertial frame, which is essential to flight. Moving forward, we will make efforts to reconcile any phase differences between the two models, particularly once a high-fidelity CFD simulation is available.

From a computational point of view, the DBET model took 2.95 seconds to solve while the UVLM model took 46.81 seconds to solve, each over 15 wingbeats. It is worth noting that the solution time per wingbeat is relatively stable throughout the DBET simulation, whereas the solution time per wingbeat increases at the beginning of the UVLM simulation and later stabilizes once the maximum number of retained wakes is reached. Nonetheless, on an average time-per-period basis, the DBET model solves roughly 15 times faster than UVLM, representing a large computational savings. Compared to coupled CFD-FEA, both UVLM and DBET are several orders of magnitude faster.

Lastly, we study the influence that flexibility has on mean

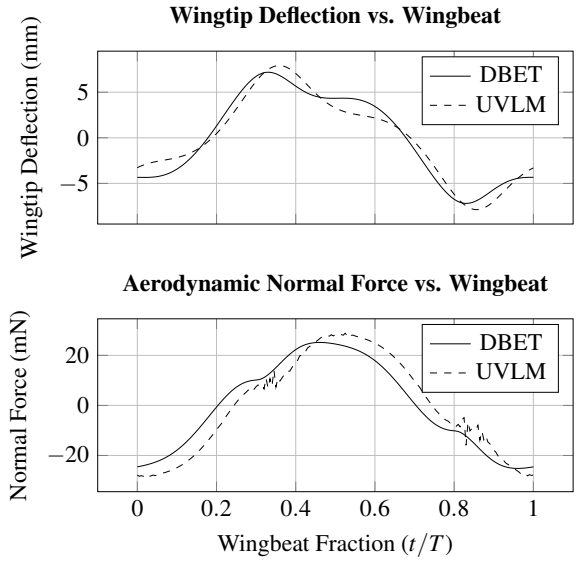


FIGURE 7. (Top) Wingtip deflection and (Bottom) aerodynamic normal force $\mathbf{F}_N$ for a flexible wing predicted by BET and UVLM solvers.

vertical aerodynamic force production (aligned with the -Y direction; Fig. 1), a relevant quantity to keeping the insect aloft. We consider the flapping kinematics in Tab. 2, and solve for the mean aerodynamic vertical force using both DBET and UVLM for both rigid and flexible wings. The results are summarized in Tab. 5. In both cases, the flexible wing produces more mean vertical force, with increases of 7% and 116% from the rigid wing as predicted by the DBET and UVLM models, respectively. We believe in this case, the UVLM model is severely overpredicting the aerodynamic benefits of wing deformation. The DBET model indicates that viscous drag increases significantly as the wing deforms. The UVLM model considers only pressure drag and cannot account for viscous drag without an empirical or other corrective model. This issue affects vector aerodynamic force production, even when the normal forces component predicted by UVLM and DBET are similar (Fig. 7).

TABLE 5. Influence of wing flexibility on mean vertical force for both fluid solvers.

Fluid Solver	Wing Type	Mean Vertical Force (mN)
DBET	Rigid	2.76
DBET	Flexible	2.97
UVLM	Rigid	3.08
UVLM	Flexible	6.67

Copyright © 2020 by ASME

CONCLUSION

In this work, we derived a reduced-order flapping wing FSI model, where the wing was idealized as a two-dimensional flexible pitching, plunging airfoil. We considered DBET and UVLM fluid models, where the former is more computational efficient but does not provide information regarding the flow surrounding the wing, and the latter partially resolves the flow structure but requires increased solution time. We found that, for a limited set of kinematics, DBET and UVLM produced similar estimates for wingtip deflection as well as aerodynamic normal forces. DBET solved approximately 15 times faster than UVLM though both fluid models are much quicker relative to direct numerical simulation. However, UVLM appears to overestimate the vector sum of aerodynamic forces produced by the wing, perhaps because it cannot account for viscous drag without modification. We believe the 7% increase in mean aerodynamic vertical force predicted by the DBET model is a more accurate reflection of the benefits of wing flexibility on force production. While this aerodynamic benefit may seem small, it is plausible that flexibility is also reducing the energy required to flap. Thus, both energy and force production should be studied simultaneously moving forward.

The primary contribution of this work is the DBET framework, which extends the most common aerodynamic model used to study flapping wing insect flight to incorporate flexibility. Nonetheless, there remain many factors to consider before the DBET model is generally applicable, even for the 2D case. Most importantly, we must explore a large range of kinematic parameters and wing stiffnesses. While DBET and UVLM agree fairly well for most responses considered here, it is possible this agreement deteriorates for kinematics that include larger rotations and/or plunging angle. Further, UVLM itself must be verified for accuracy against higher-order CFD, particularly because it does not model viscous forces in this current form. Despite these limitations, the research presented here provides a solid foundation for further studies in reduced-order modeling of flapping wing FSI.

ACKNOWLEDGMENT

This research was supported the National Science Foundation under awards Nos. CBET-1855383 and CMMI-1942810. Any opinions, findings, and conclusions or recommendations expressed in this material are those of the author(s) and do not necessarily reflect the views of the National Science Foundation.

REFERENCES

[1] Phan, H. V., and Park, H. C., 2019. "Insect-inspired, tailless, hover-capable flapping-wing robots: Recent progress, challenges, and future directions". *Progress in Aerospace Sciences*, p. 100573.

[2] Farrell Helbling, E., and Wood, R. J., 2018. "A review of propulsion, power, and control architectures for insect-scale flapping-wing vehicles". *Applied Mechanics Reviews,* ***70***(1).

[3] Combes, S. A., and Daniel, T. L., 2003. "Into thin air: contributions of aerodynamic and inertial-elastic forces to wing bending in the hawkmoth manduca sexta". *Journal of Experimental Biology,* ***206***(17), pp. 2999–3006.

[4] Mountcastle, A. M., and Combes, S. A., 2013. "Wing flexibility enhances load-lifting capacity in bumblebees". *Proceedings of the Royal Society B: Biological Sciences,* ***280***(1759), p. 20130531.

[5] Jankauski, M., Guo, Z., and Shen, I., 2018. "The effect of structural deformation on flapping wing energetics". *Journal of Sound and Vibration,* ***429***, pp. 176–192.

[6] Dickerson, B. H., Aldworth, Z. N., and Daniel, T. L., 2014. "Control of moth flight posture is mediated by wing mechanosensory feedback". *Journal of Experimental Biology,* ***217***(13), pp. 2301–2308.

[7] Shyy, W., Aono, H., Chimakurthi, S. K., Trizila, P., Kang, C.-K., Cesnik, C. E., and Liu, H., 2010. "Recent progress in flapping wing aerodynamics and aeroelasticity". *Progress in Aerospace Sciences,* ***46***(7), pp. 284–327.

[8] Tian, F.-B., Dai, H., Luo, H., Doyle, J. F., and Rousseau, B., 2014. "Fluid–structure interaction involving large deformations: 3d simulations and applications to biological systems". *Journal of computational physics,* ***258***, pp. 451–469.

[9] Takizawa, K., Tezduyar, T. E., and Kostov, N., 2014. "Sequentially-coupled space–time fsi analysis of bio-inspired flapping-wing aerodynamics of an mav". *Computational Mechanics,* ***54***(2), pp. 213–233.

[10] Jankauski, M., and Shen, I., 2014. "Dynamic modeling of an insect wing subject to three-dimensional rotation". *International Journal of Micro Air Vehicles,* ***6***(4), pp. 231–251.

[11] Jankauski, M., and Shen, I., 2016. "Experimental studies of an inertial-elastic rotating wing in air and vacuum". *International Journal of Micro Air Vehicles,* ***8***(2), pp. 53–63.

[12] Anderson, J. D., and Wendt, J., 1995. *Computational fluid dynamics*, Vol. 206. Springer.

[13] Yin, B., and Luo, H., 2010. "Effect of wing inertia on hovering performance of flexible flapping wings". *Physics of Fluids,* ***22***(11), p. 111902.

[14] Tian, F.-B., Luo, H., Song, J., and Lu, X.-Y., 2013. "Force production and asymmetric deformation of a flexible flapping wing in forward flight". *Journal of Fluids and Structures,* ***36***, pp. 149–161.

[15] Sridhar, M., and Kang, C.-k., 2015. "Aerodynamic performance of two-dimensional, chordwise flexible flapping wings at fruit fly scale in hover flight". *Bioinspiration & biomimetics,* ***10***(3), p. 036007.

[16] Roccia, B. A., Preidikman, S., and Balachandran, B., 2017.

 Copyright © 2020 by ASME

"Computational dynamics of flapping wings in hover flight: a co-simulation strategy". *AIAA Journal,* ***55***(6), pp. 1806–1822.

[17] Wang, Q., Goosen, J., and van Keulen, F., 2017. "An efficient fluid–structure interaction model for optimizing twistable flapping wings". *Journal of Fluids and Structures,* ***73***, pp. 82–99.

[18] Schwab, R. K., Reid, H. E., and Jankauski, M., 2020. "Reduced-order modeling and experimental studies of bilaterally coupled fluid-structure interaction in single-degree-of-freedom flapping wings (in press)". *Journal of Vibration and Acoustics*.

[19] Schwab, R. K., Reid, H. E., and Jankauski, M. A., 2019. "Reduced-order modeling and experimental studies of two-way coupled fluid-structure interaction in flapping wings". In ASME 2019 International Design Engineering Technical Conferences and Computers and Information in Engineering Conference, American Society of Mechanical Engineers Digital Collection.

[20] Schwab, R., Johnson, E., and Jankauski, M., 2019. "A novel fluid–structure interaction framework for flapping, flexible wings". *Journal of Vibration and Acoustics,* ***141***(6).

[21] Fitzgerald, T., Valdez, M., Vanella, M., Balaras, E., and Balachandran, B., 2011. "Flexible flapping systems: computational investigations into fluid-structure interactions". *The Aeronautical Journal,* ***115***(1172), pp. 593–604.

[22] Mountcastle, A., and Daniel, T., 2010. "Vortexlet models of flapping flexible wings show tuning for force production and control". *Bioinspiration & biomimetics,* ***5***(4), p. 045005.

[23] Whitney, J. P., and Wood, R. J., 2010. "Aeromechanics of passive rotation in flapping flight". *Journal of Fluid Mechanics,* ***660***, pp. 197–220.

[24] Sedov, L. I., Chu, C., Cohen, H., Seckler, B., and Gillis, J., 1965. "Two-dimensional problems in hydrodynamics and aerodynamics". *Physics Today,* ***18***, p. 62.

[25] Katz, J., and Plotkin, A., 2001. *Low-speed aerodynamics*, Vol. 13. Cambridge university press.

[26] Roccia, B. A., Preidikman, S., Massa, J. C., and Mook, D. T., 2013. "Modified unsteady vortex-lattice method to study flapping wings in hover flight". *AIAA journal,* ***51***(11), pp. 2628–2642.

[27] Tang, L., Pai, M. P., et al., 2007. "On the instability and the post-critical behaviour of two-dimensional cantilevered flexible plates in axial flow". *Journal of Sound and Vibration,* ***305***(1-2), pp. 97–115.

[28] Combes, S., and Daniel, T., 2003. "Flexural stiffness in insect wings i. scaling and the influence of wing venation". *Journal of experimental biology,* ***206***(17), pp. 2979–2987.

[29] Sims, T. W., Palazotto, A. N., and Norris, A., 2010. "A structural dynamic analysis of a manduca sexta forewing". *International Journal of Micro Air Vehicles,* ***2***(3), pp. 119–140.

[30] Meirovitch, L., 2010. *Fundamentals of vibrations*. Waveland Press.

[31] Willmott, A. P., and Ellington, C. P., 1997. "The mechanics of flight in the hawkmoth manduca sexta. i. kinematics of hovering and forward flight.". *Journal of experimental Biology,* ***200***(21), pp. 2705–2722.

APPENDIX A - KINETIC ENERGY

This appendix provides additional detail on the derivation of Eq. 11. In general, the Lagrange formulation requires explicit representations of kinetic energy T and potential energy U. Expanding Eqs. 9-10 in terms of Eqs. 6,8 yields

$$
\begin{aligned}
T_1 &= \frac{1}{2}\dot{\theta}^2 \int_m W^2\, dm = \frac{1}{2}\dot{\theta}^2 \sum_{k=1}^{\infty} q_k^2 \\
T_2 &= -\dot{\theta}\dot{Z}\sin\theta \int_m W\, dm = -\dot{\theta}\dot{Z}\sin\theta \sum_{k=1}^{\infty} q_k \int_m \phi_k\, dm \\
T_3 &= \frac{1}{2}\dot{Z}^2 \int_m dm = \frac{1}{2} m \dot{Z}^2 \\
T_4 &= \frac{1}{2}\dot{\theta}^2 \int_m y^2 dm = \frac{1}{2} I_{xx}\dot{\theta}^2 \\
T_5 &= \frac{1}{2}\int_m \dot{W}^2\, dm = \frac{1}{2}\sum_{k=1}^{\infty} \dot{q}_k^2 \\
T_6 &= \dot{Z}\cos\theta \int_m y\, dm \\
T_7 &= \dot{\theta}\int_m \dot{W} y\, dm = \dot{\theta}\sum_{k=1}^{\infty} \dot{q}_k \int_m \phi_k y\, dm \\
T_8 &= \dot{Z}\cos\theta \int_m \dot{W}\, dm = \dot{Z}\cos\theta \sum_{k=1}^{\infty} \dot{q}_k \int_m \phi_k\, dm \\
U &= \frac{1}{2}\int_V S(W,W)\, dV = \frac{1}{2}\sum_{k=1}^{\infty} \omega_k^2 q_k^2
\end{aligned}
$$

where $T = \sum_{m=1}^{8} T_m$. Then, to determine the equation of motion governing q_k, we apply the Lagrangian formulation. Treating q_k as our generalized coordinate, we have

$$
\frac{d}{dt}\left(\frac{\partial T}{\partial \dot{q}_k}\right) - \frac{\partial T}{\partial q_k} + \frac{\partial V}{\partial q_k} = Q_k
$$

Carrying out the above operations results in Eq. 11.

Copyright © 2020 by ASME

INVESTIGATION OF CHORDWISE FUNCTIONALLY GRADED FLEXURAL RIGIDITY IN FLAPPING WINGS USING A TWO-DIMENSIONAL PITCH-PLUNGE MODEL

Contribution of Authors and Co-Authors

Manuscript in following chapter

Author: Joseph Reade

Contributions: Development of vortex lattice model

Author: Mark Jankauski

Contributions: Development of blade element model

Manuscript Information

J. Reade, M. Jankauski

Bioinspiration and Biomimetics

Status of Manuscript:
____ Prepared for submission to a peer-reviewed journal
____ Officially submitted to a peer-reviewed journal
____ Accepted by a peer-reviewed journal
_X_ Published in a peer-reviewed journal

Institute of Physics
September 2022
Volume 17, Issue 6
DOI: 10.1088/1748-3190/ac8f05

Bioinspiration & Biomimetics

PAPER

Investigation of chordwise functionally graded flexural rigidity in flapping wings using a two-dimensional pitch–plunge model

To cite this article: Joseph Reade and Mark Jankauski 2022 *Bioinspir. Biomim.* **17** 066007

View the article online for updates and enhancements.

You may also like

- Aerodynamic comparison of a butterfly-like flapping wing–body model and a revolving-wing model
Kosuke Suzuki and Masato Yoshino
- Optimal flapping wing for maximum vertical aerodynamic force in hover: twisted or flat?
Hoang Vu Phan, Quang Tri Truong, Thi Kim Loan Au et al.
- Experimental optimization of wing shape for a hummingbird-like flapping wing micro air vehicle
Yanghai Nan, Matj Karásek, Mohamed Esseghir Lalami et al.

This content was downloaded from IP address 153.90.112.191 on 08/07/2024 at 19:11

IOP Publishing Bioinspir. Biomim. 17 (2022) 066007 https://doi.org/10.1088/1748-3190/ac8f05

Bioinspiration & Biomimetics



PAPER

Investigation of chordwise functionally graded flexural rigidity in flapping wings using a two-dimensional pitch–plunge model

RECEIVED
15 April 2022

REVISED
2 August 2022

ACCEPTED FOR PUBLICATION
2 September 2022

PUBLISHED
3 October 2022

Joseph Reade and Mark Jankauski*

Montana State University, Department of Mechanical & Industrial Engineering, Bozeman, MT, United States of America
* Author to whom any correspondence should be addressed.

E-mail: mark.jankauski@montana.edu

Keywords: flapping wings, unsteady vortex lattice method, reduced-order modeling, pitching-plunging airfoil, insect flight, structural dynamics

Abstract

Insect wings are heterogeneous structures, with flexural rigidity varying one to two orders of magnitude over the wing surface. This heterogeneity influences the deformation the flapping wing experiences during flight. However, it is not well understood how this flexural rigidity gradient affects wing performance. Here, we develop a simplified 2D model of a flapping wing as a pitching, plunging airfoil using the assumed mode method and unsteady vortex lattice method to model the structural and fluid dynamics, respectively. We conduct parameter studies to explore how variable flexural rigidity affects mean lift production, power consumption and the forces required to flap the wing. We find that there is an optimal flexural rigidity distribution that maximizes lift production; this distribution generally corresponds to a 3:1 ratio between the wing's flapping and natural frequencies, though the ratio is sensitive to flapping kinematics. For hovering flight, the optimized flexible wing produces 20% more lift and requires 15% less power compared to a rigid wing but needs 20% higher forces to flap. Even when flapping kinematics deviate from those observed during hover, the flexible wing outperforms the rigid wing in terms of aerodynamic force generation and power across a wide range of flexural rigidity gradients. Peak force requirements and power consumption are inversely proportional with respect to flexural rigidity gradient, which may present a trade-off between insect muscle size and energy storage requirements. The model developed in this work can be used to efficiently investigate other spatially variant morphological or material wing features moving forward.

1. Introduction

Flapping insect wings are highly compliant structures that deform under aerodynamic and inertial forces [1]. Deformation is believed to play a fundamental role in insect flight mechanics and has been shown to enhance aerodynamic force generation [2–4] and energetic efficiency [5–7]. Various structural features, including venation and corrugation, influence wing deformation under dynamic loading. These features also govern how the wing's mechanical properties vary in space. Experimental studies have shown that the flexural rigidity of the Hawkmoth *Manduca sexta* forewing, for example, varies one to two orders of magnitude over the wing's chord length [8]. This pronounced gradient may underpin wing responses that are aerodynamically and energetically favorable. However, it is not well understood how graded flexural rigidity influences flapping wing performance.

This is in part because models used to predict wing fluid–structure interaction (FSI) are computationally-intensive. They are consequently challenged by parameter studies that consider variable flexural rigidity or other morphological and material properties. Flapping wing FSI models usually rely on coupled finite element method (FEM) and computational fluid dynamic solvers (CFD) [9–13]. Flapping wings pose unique challenges to both of these numerical approaches. Given the finite, periodic rotation of the wing, stiffness matrices within FEM must be updated at each time interval of analysis, which increases computation times considerably [14]. CFD requires that the Navier–Stokes equations be solved across a discretized fluid domain [15],

© 2022 IOP Publishing Ltd

which could result in upwards of hundreds of thousands of equations to solve. Estimating wing deformation via coupled CFD/FEM may therefore span several hours per wingbeat in some cases.

Lower-order FSI models can decrease the computational requirements considerably. Simplifications in fluid and structural solvers, as well as converting the 3D problem to a 2D idealization, have yielded models that can be solved on the order of seconds. Some of the most common flapping wing FSI models treat the wing as a 2D pitching, plunging airfoil [2, 3, 7, 16, 17]. The airfoil represents a cross-section running along the chord of the insect's wing. Plunge represents the primary flap rotation and pitch represents the rotation the wing experiences about its leading edge. The 2D pitch–plunge framework neglects some of the physics that play a role in true 3D flapping, such as spanwise bending [18], spanwise flow [19] and wingtip effects [20]. Despite lower quantitative accuracy relative to 3D models, 2D models can quickly identify solution trends and thus can establish foundational knowledge that may be subsequently extended to more computationally intensive 3D modeling. For this purpose, they have been widely utilized to investigate several aspects of flapping wing mechanics. For example, Yin and Luo used a pitch–plunge model to show that, when a wing's deformation was dominated by external flows rather than inertia, it had better power efficiency [7]. Tian *et al* used this framework to understand how asymmetry between the wing's deformation during upstroke and downstroke affected forward flight [17]. Vanella *et al* demonstrated that a super-harmonic resonance may favorably influence the wing's lift to drag ratio at low Reynold's numbers [2]. Mountcastle and Daniel investigated how variable wing kinematics and structural properties affected the wing's lift generation [3].

Despite the contributions of these works and others, the influence graded flexural rigidity has on flapping wing aeromechanics remains understudied. The objectives of the present research are to (1) develop a reduced-order FSI model of a flapping, flexible insect wing treated as a pitching plunging airfoil, and (2) to use this model to understand how chordwise graded flexural rigidity affects wing dynamics. Specifically, we evaluate lift, power and the forces required to drive the wing. We employ a number of assumptions to simplify the wing structure and flapping kinematics in this study. First, because we treat the wing as a 2D pitching, plunging airfoil, spanwise flow, spanwise bending and wingtip losses associated with 3D motion are neglected. Second, we neglect complex venation patterns, cross-sectional curvature and spatially-variable material properties that may affect the wing's local flexural rigidity. We instead assume that spatial variation of flexural rigidity is driven by chordwise variations of wing thickness, since vein thickness reduces dramatically along the chord in many insect wings [21]. Because of these assumptions, the model developed in this work is not suitable for high-fidelity fluid or structural calculations of real insect wings. It is instead intended to isolate and study variable flexural rigidity in a simpler setting.

The remainder of this manuscript is organized as follows. First, we derive the FSI framework using the assumed mode method (AMM) to model the structure and unsteady vortex lattice method (UVLM) to model the fluid. Next, we apply the model to numerically simulate the response of a wing with similar properties to a Hawkmoth *Manduxa sexta* (*M. sexta*) forewing. We explore the aerodynamics and energetic requirements of the wing under hovering flapping circumstances, and conduct a parameter study to determine how these quantities are influenced by variable kinematics. We conclude by discussing the broader implications of this research on the study of insect flight and insect-inspired robotics.

2. Theory

2.1. Structural model

In this section, we derive the equation of motion governing the wing's deformation via the Lagrangian approach. We treat the wing as an Euler–Bernoulli beam, where the leading edge is clamped and the trailing edge is free to deflect. Wing deformation is calculated using the AMM, where the total deflection is a linear combination of the wing's eigenfunctions. This work expands upon the structural model derived in [22].

First, we first define two reference frames; an inertial $X-Y-Z$ frame that is fixed in space, and a body-fixed $x-y-z$ frame that translates and rotates with the wing's rigid body motion (figure 1). Note that the gravity would act in the $+Y$ direction, and thus the wing must produce lift in the $-Y$ direction in order for the insect to remain aloft. The origin O of the $x-y-z$ frame is located at the leading edge of the wing. O is subject to prescribed plunging $Z(t)$ and the wing experiences prescribed pitching $\theta(t)$ about O. The $x-y-z$ frame has angular velocity

$$\boldsymbol{\Omega} = \dot{\theta}\boldsymbol{e}_x \tag{1}$$

The position $\boldsymbol{R}$ of a differential mass element dm relative to the body-fixed frame is the sum of three component vectors (e.g., $\boldsymbol{R} = \boldsymbol{r}_1 + \boldsymbol{r}_2 + \boldsymbol{r}_3$), where

$$\boldsymbol{r}_1 = Z(t)\boldsymbol{e}_Z = Z(t)\sin\theta\boldsymbol{e}_y + Z(t)\cos\theta\boldsymbol{e}_z \tag{2}$$

$$\boldsymbol{r}_2 = y\boldsymbol{e}_y \tag{3}$$

$$\boldsymbol{r}_3 = w(y,t)\boldsymbol{e}_z \tag{4}$$

Above, $\boldsymbol{r}_1$ describes the displacement associated with the plunging motion, $\boldsymbol{r}_2$ describes the position of dm at a location y along the wing's chord, and $\boldsymbol{r}_3$ describes

IOP Publishing Bioinspir. Biomim. 17 (2022) 066007 J Reade and M Jankauski

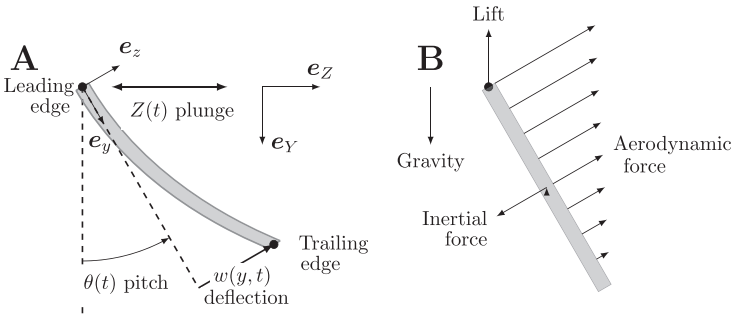


Figure 1. (A) Reference frames and pitch–plunge motion, (B) free-body diagram of forces acting on the wing and gravity vector to show orientation. Cartesian grad applies to both panels. The black circle in both panels indicates where the wing would meet insect body.

an infinitesimal out-of-plane wing deflection w. In-plane deflection is neglected. The velocity of dm is

$$\dot{\boldsymbol{R}} = [\dot{Z}\,\sin\,\theta - w\dot{\theta}]\,\boldsymbol{e}_y + [\dot{Z}\,\cos\,\theta + y\dot{\theta} + \dot{w}]\,\boldsymbol{e}_z \tag{5}$$

and the acceleration of dm is

$$\ddot{\boldsymbol{R}} = [\ddot{Z}\,\sin\,\theta - 2\dot{w}\dot{\theta} - w\ddot{\theta} - y\dot{\theta}^2]\boldsymbol{e}_y\ \ldots + [\ddot{Z}\,\cos\,\theta + \ddot{w} + y\ddot{\theta} - w\dot{\theta}^2]\boldsymbol{e}_z \tag{6}$$

While $\ddot{\boldsymbol{R}}$ is not required to derive the equation of motion, it is necessary to calculate power consumption and inertial forces and moments as detailed later. We expand wing deflection $w(y,t)$ in terms of mass-normalized mode shapes ϕ_k and modal responses q_k as

$$w(y,t) = \sum_{k=1}^{\infty} \phi_k(y)\,q_k(t). \tag{7}$$

In practice, only a finite number of modes are used. In this implementation, we include only the first mode (see section 3). The wing's total kinetic and potential energies are subsequently formulated. Applying Lagrange's equation, we arrive at the equation of motion governing modal response q_k as

$$\ddot{q}_k + 2\zeta_k\omega_k\dot{q}_k + (\omega_k^2 - \dot{\theta}^2)q_k = -\lambda_k\ddot{Z}\,\cos\,\theta - \psi_k\ddot{\theta} + Q_k \tag{8}$$

where ω_k and ζ_k are the wing's kth natural frequency and damping ratio, respectively. Note that the viscous damping term is not derived explicitly through the energy formulation and is instead included as an empirical correction term. Constants λ_k and ψ_k are obtained by integrating the mode shape over the wing's mass domain, or

$$\lambda_k = \int_m \phi_k\,\mathrm{d}m \tag{9}$$

$$\psi_k = \int_m y\phi_k\,\mathrm{d}m \tag{10}$$

Equation (8) shows that the wing's stiffness is time-varying and dependent on the wing's pitching rate and stationary natural frequency. The first excitation term to the right-hand side of equation (8) is a plunge-dominated inertial term proportional to the linear acceleration of the wing. The second excitation term is a pitch-dominated inertial term modulated by the wing's angular acceleration. The non-conservative generalized load Q_k is obtained by integrating the projection of an aerodynamic force distribution onto the mode shape

$$Q_k = \int_c \phi_k(\mathrm{d}\boldsymbol{F}_{\mathrm{aero}} \cdot \boldsymbol{e}_z)\,\mathrm{d}y \tag{11}$$

where d$\boldsymbol{F}_{\mathbf{aero}}$ is the aerodynamic force per unit length, discussed the following section.

2.2. Fluid model

We use a modified UVLM approach to predict the flow and estimate the force distribution over the wing. Our method is based on that described in [23]. Only a high-level description of the model is given here. For additional detail on the mathematical derivation, please refer to appendix A.

UVLM is based on potential flow theory. The flow is assumed to be irrotational, except on the surface of the wing and in the wake that is shed from the trailing edge, and is incompressible throughout. By modeling the wake, we account for unsteady effects such as added mass. Viscous effects are not accounted for. Using the maximum plunge rate and chord width as the characteristic speed and length respectively, the Reynolds number of the wing simulated in this work under normal hovering conditions is about 5000 (see section 3). This indicates that inertial aerodynamic forces will far exceed viscous aerodynamic forces, and hence we believe the inviscid assumption is reasonable in this study.

The wing is discretized into N_{p} panels, each of length ds (figure 2). On each panel, a bound vortex and control point are located 0.25 ds and 0.75 ds from the leading edge of the panel, respectively. Additionally, a wake vortex is shed from the trailing edge of the

IOP Publishing Bioinspir. Biomim. 17 (2022) 066007 J Reade and M Jankauski

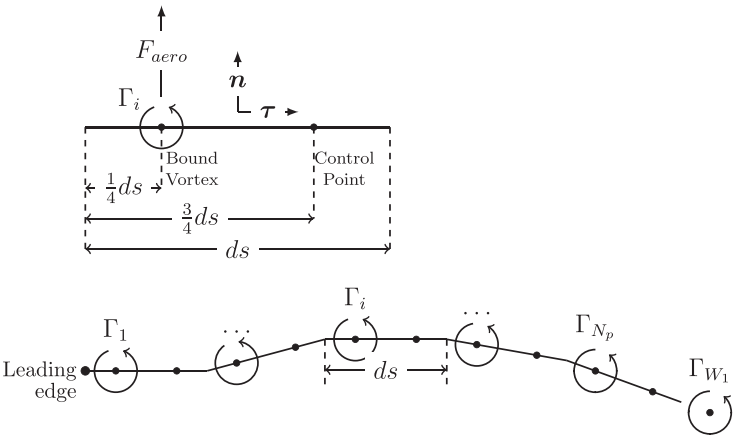


Figure 2. Wing discretization used by UVLM.

wing at each time step, with the wake being truncated at N_w vortices. A bound vortex induces a flow velocity around itself that diminishes with distance. The flow velocity at any point in space that is induced by a vortex is given by the Biot–Savart law. Then, according to the Kelvin–Helmholtz theorem for an ideal fluid, the total circulation around a closed contour must remain constant. Since the initial state of the fluid flow is at rest with zero vorticity throughout, this implies that the total vorticity, found by summing the strengths of the bound and wake vortices, is zero at each time step. This condition is used to calculate the strength of the wake vortices.

Flow may not travel through the solid surface of the wing, meaning that the component of velocity normal to the surface is zero. Because there are a finite number of bound vortices, the non-penetration condition cannot be satisfied across an entire panel, so the control point is chosen as the location where it must hold true. By simultaneously enforcing the non-penetration condition at all control points on the wing, as well as the Kelvin–Helmholtz condition, the strengths of the bound vortices can be determined. Advected wake vortices are placed a fixed distance aft of the trailing edge. All existing wake vortices are advected with the local flow. Finally, the aerodynamic force on the wing is determined using the unsteady Bernoulli equation.

2.3. Force, moments and power

Flight is the most energetically expensive mode of locomotion per unit of time, and thus it is essential to understand how the wing's structural dynamics underpin low energetic expenditures. In this section, we derive expressions based on modal responses to calculate flapping wing moments, forces and instantaneous power.

Total power consumption is broken into two components: inertial power and aerodynamic power. Inertial power is required to move the wing mass through space—if the wing was operated in a vacuum, inertial power would equal to total power. Inertial power of a rotating, translating system is

$$P_{\text{inertial}} = \boldsymbol{F}_O \cdot \dot{\boldsymbol{r}}_1 + \boldsymbol{M}_O \cdot \boldsymbol{\Omega} \tag{12}$$

where $\boldsymbol{F}_O$ is the inertial force at O and $\boldsymbol{M}_O$ is the inertial moment about the leading edge. The inertial force is the wing's spatiotemporal acceleration integrated over the wing's mass, is

$$\boldsymbol{F}_O = \left[m\ddot{Z} \sin\theta - \dot{\theta}^2\xi - \sum_{k=1}^{\infty} (2\dot{q}_k\dot{\theta}\lambda_k + q_k\ddot{\theta}\lambda_k) \right] \boldsymbol{e}_y + \left[m\ddot{Z}\cos\theta + \ddot{\theta}\xi \; - \sum_{k=1}^{\infty} (q_k\dot{\theta}^2\lambda_k - \ddot{q}_k\lambda_k) \right] \boldsymbol{e}_z \tag{13}$$

where m is the mass of the wing and ξ is a constant defined by

$$\xi = \int_m y \, \mathrm{d}m. \tag{14}$$

The inertial moment about O is

$$\boldsymbol{M}_O = \left[\ddot{Z}\xi\cos\theta + I_{xx}\ddot{\theta} + \sum_{k=1}^{\infty} \left(\ddot{q}_k\phi_k - \ddot{Z}q_k\lambda_k \sin\theta + \ddot{\theta}q_k^2 + 2q_k\dot{q}_k\dot{\theta} \right) \right] \boldsymbol{e}_x \tag{15}$$

where I_{xx} is the wing's mass-moment of inertia about O. The aerodynamic power is the power required to overcome the fluid forces acting against the wing, given by

$$P_{\text{aero}} = \int_{\text{chord}} \mathrm{d}\boldsymbol{F}_{\text{aero}} \cdot \dot{\boldsymbol{R}} \, \mathrm{d}y \tag{16}$$

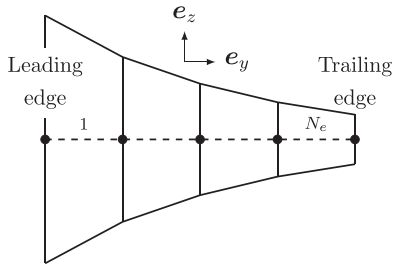


Figure 3. Wing discretization with exponential thickness distribution. Nodes $2, \ldots, N_e + 1$ may experience vertical displacement and rotation, while the leading-edge node is clamped. Wing thickness is exaggerated.

where $d\boldsymbol{F}_{aero}$ is the aerodynamic force at some point on the wing as computed by the UVLM.

3. Numerical simulation

Here, we describe the numerical parameters used to simulate the dynamic response of the wing. We use the FEM to convert the wing from a continuous domain to a discrete domain (see appendix B). The finite element discretization is implemented using a custom in-house MATLAB (Ver. 2020b) code. The wing is discretized into N_e beam elements each with two degrees-of-freedom (vertical displacement and rotation) at each node. We use spatially variable wing thickness to modulate local flexural rigidity, since wing flexural rigidity is affected by thickness and Young's modulus and the latter is kept constant (figure 3). The wing thickness decays exponentially from leading edge to trailing edge, with the thickness t at chordwise location y described by

$$t(y) = t_{LE} e^{-a\frac{y}{c}}, \tag{17}$$

where t_{LE} is the leading edge thickness, c is the chord length and a is the decay rate. Values of a range from 0 to 1.6, which correspond to leading-to-trailing-edge taper ratios t_{TE}/t_{LE} from 1.0 (uniform thickness) to 0.2 (highly tapered). The most tapered case results in a two orders-of-magnitude decrease in flexural stiffness over the chord, which encompasses the range of chordwise-stiffness distributions reported in *Manduca sexta* [8]. Wing mass is maintained at 45 mg across all taper ratios tested. Consequently, each wing has an average thickness of 45 μm, but the leading edge thickness t_{TE} varies with taper ratio. The maximum leading edge thickness considered is 90 μm for the most tapered wing. We also simulate rigid wings across all taper ratios to compare their performance against flexible wings.

We use 40 panels, 40 finite elements, 100 wakes and 200 time steps per wingbeat for all numerical studies. The convergence studies that informed these parameters are detailed in appendix C. We neglect any modes associated with frequencies at least ten times higher than the flapping frequency, as the contribution of these modes is expected to be small. The second natural frequency was 360 Hz for a homogeneous wing, which is roughly 14 times greater than the flapping frequency of 25 Hz. All other stiffness distributions tested have a greater second natural frequency. Therefore, only the first mode was retained for simulations. We use the MATLAB (Ver. 2020b) explicit ode45 solver to simulate the response of the wing. For all simulations, we calculate wing deflection, forces at the leading edge and total power required to flap the wing. We also calculate mean lift-to-power as proxy for flight efficiency.

Table 1. Wing parameters.

Symbol	Description	Value	Units
E	Young's modulus	10	GPa
c	Chord length	2	cm
b	Span	5	cm
m	Mass	45	mg
t_{avg}	Average thickness	45	μm
ρ	Density	1000	kg m^{-3}
ζ_1	First modal damping ratio	0.05	—
Z_0	Plunge amplitude	2.62	cm
θ_0	Pitch amplitude	45	$^\circ$
β_z	Pitch–plunge phase difference	-90	$^\circ$
ω	Flapping frequency	25	Hz

Wing morphology and flapping kinematics are based approximately on the *M. Sexta* [8, 24, 25] and are summarized in table 1. Flapping kinematics assume hovering flight. Pitch and plunge are idealized as purely harmonic with a frequency of 25 Hz and a phase difference of -90°. The plunge amplitude was approximated by the distance traveled by the semi-span ($x =$ span/2) of a three-dimensional wing experiencing a flap amplitude of 60°. The Young's modulus and density were estimated from measurements on insect cuticle [26, 27].

Prior to numerical simulations on tapered wings, we performed a validation study on homogeneous flexible wings to benchmark the accuracy of our model (see appendix D). Lift coefficients generated via our reduced-order model were compared to those generated by a higher-fidelity model [7]. Note that the flapping kinematics used in the validation study vary modestly from those used in the hovering case described in this paper. The lift coefficients predicted for each model had similar magnitude, but were modestly out of phase.

4. Results

In this section, we show how taper ratio influences flexural rigidity and thus the dynamics of flapping wings. First, we determine how taper affects the wing's first natural frequency and mode shape. Next, we calculate wingtip deflection, lift, power consumption and total forces acting at the wing's leading edge

IOP Publishing Bioinspir. Biomim. 17 (2022) 066007 J Reade and M Jankauski

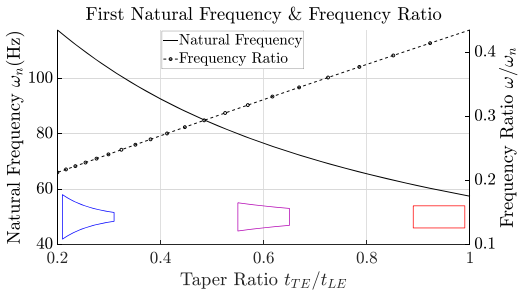


Figure 4. First natural frequency (solid line) and frequency ratio (dashed line) as a function of chordwise wing taper. Approximate airfoils indicating the taper are shown at the bottom of the figure, with taper ratios of 0.2, 0.6, and 1 from left to right. Flapping frequency is assumed to be 25 Hz.

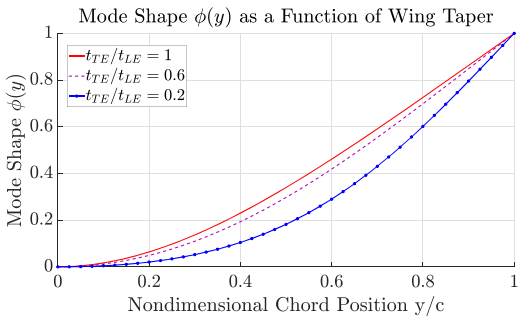


Figure 5. The bending mode used to calculate wing deflection. Mode shapes presented in this plot are normalized by the maximum value at the trailing edge.

for a wing flapping with hovering kinematics. We then conduct a parameter study to examine how deviations from hovering kinematics affect wing performance.

4.1. Natural frequencies & mode shapes

The wing's natural frequency affects deflection magnitude and consequently, the aerodynamic forces that arise from flapping. Certain flapping-to-natural frequency ratios have been shown to improve the aerodynamic and energetic performance of flapping wings [2, 5, 6]. Here, we explore how variable flexural rigidity influences the wing's natural frequency to provide context to the dynamic studies described in the following sections.

Over the range of taper ratios considered, the wing's natural frequency varies from about 57 to 115 Hz (figure 4). Assuming a flap frequency of 25 Hz, this coincides to a flapping-to-natural frequency ratio range from 0.21 to 0.44. Natural frequencies corresponding to the first torsional mode in *M. sexta* forewings have been reported between 75–95 Hz [25, 28], which are represented by taper ratios from about 0.4 to 0.5. Note that the first mode in the *M. sexta* forewing corresponds to a bending mode, however since our 2D model does not account for spanwise deformation, it is more appropriate to compare our computed natural frequencies to torsional modes where deformation varies predominately over the wing chord. Though the bending mode in *M. sexta* wings has a lower natural frequency (≈60–70 Hz, [25, 28]) than the twisting mode, this does not necessarily imply the bending mode is more important. The insect flaps at about 25 Hz, and previous studies have shown flapping excites frequencies at odd multiples of the wingbeat frequency. Consequently, twisting may be as significant as bending to wing deformation.

As the taper ratio decreases from 1 to 0.2, the wing's local area moment of inertia and mass increase near the leading edge and decrease towards the trailing edge. As a result, the wing's natural frequency is inversely proportional to taper ratio (figure 4). The most tapered wing has a natural frequency nearly double that of the homogeneous wing. Mode shapes associated with tapered wings tend to bend more around the center of the chord, while bending is localized towards the leading edge in homogeneous wings (figure 5). This is consistent with torsional mode shapes measured in *M. sexta* forewings [25].

IOP Publishing Bioinspir. Biomim. 17 (2022) 066007 J Reade and M Jankauski

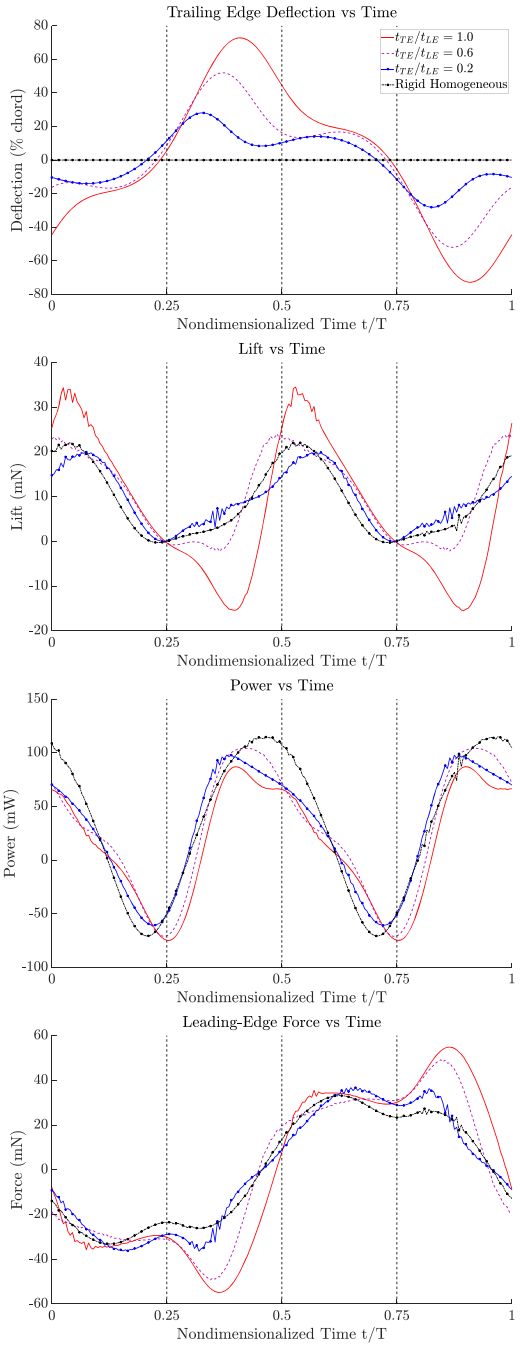


Figure 6. Comparison of lift, power, leading edge force, and wing tip deflection for several taper ratios using kinematics in table 1.

IOP Publishing Bioinspir. Biomim. 17 (2022) 066007 J Reade and M Jankauski

4.2. Flapping with hovering kinematics

We now examine the wing's dynamic response assuming the flapping kinematics described in table 1. Wing deflection, lift, power and leading edge force are shown for various taper ratios in figure 6. Quantities are reported as a function of wingbeat fraction t/T, where t is time and T is the wingbeat period. All quantities are taken once the wing has achieved steady-state. We use mean power as a proxy for energy consumption. This assumes negative power is elastically stored in the insect exoskeleton and that this stored potential energy can be recycled to offset positive power requirements. Then, we use the Z component of total leading edge force $\mathbf{F}_{T,XYZ}$ to approximate the forces the insect flight muscle must produce in order to flap the wing. $\mathbf{F}_{T,XYZ}$ is defined with respect to the inertial coordinate system and is inclusive of both aerodynamic and inertial forces. The Z component of $\mathbf{F}_{T,XYZ}$ (simply leading edge force hereafter) is a better proxy for muscle forces than total moment $\mathbf{M}_T$, since the literature suggests wing pitching arises passively from inertial and aerodynamic forces [29].

Calculated deflections appear to be consistent with reported values for *M. sexta* [24]. Previous studies reported the angle of rotation between the leading edge and the trailing edge, which is an aggregate quantity influenced both by the rigid body pitch angle and trailing edge deflection. Angles of rotation were typically around 45° for chords proximal to the insect body and 65° for chords distal to the insect body. Our model predicted angles of rotation of approximately 59° when for a taper ratio of 0.2 and 71° for a taper ratio of 1. While the homogeneous wing resulted in an angle of rotation greater than reported values, the tapered wings matched fairly well. Aerodynamic forces are also consistent with those produced by *M. sexta*. Assuming the insect has a body mass of 2.0 grams [30], a wing pair produces sufficient lift to hover when taper ratios are between about 0.27 and 0.65. This corresponds to a natural frequency range of about 70 to 109 Hz.

As chordwise wing taper ratio increases, both wingtip deflection amplitude and primary response phase (taken with respect to plunge) decrease (figure 6). The lower deflection is due to the tapered wing being stiffer than the homogeneous wing, evidenced by the higher natural frequency (figure 4). Peak deflection moves away from the mid-stroke ($t/T = 0,\ 0.5$) and towards the stroke reversals ($t/T = 0.25,\ 0.75$) as wing flexibility increases. This indicates that deflection in highly tapered wings is more influenced by the plunging inertial force and less by the aerodynamics, as plunging acceleration $\ddot{Z}$ is at a maximum while the aerodynamic force is minimized at stroke reversal.

Chordwise wing taper has a large effect on lift production. While the homogeneous wing generated the highest peak lift, its time-averaged lift was 20 to 30 percent lower than that of the other wings (table 2). This can be partially attributed to the large troughs in lift occurring at $t/T \approx 0.375, 0.875$, when the plunging motion of the wing reverses. These troughs are not seen with the stiffer wings. The lowest point in the trough roughly corresponds to the peak deflection experienced by the wing. Separating lift into steady and unsteady components, we see that the negative lift is largely driven by the steady component. When the wing undergoes large deflections, it reduces the effective angle of attack and creates an adverse camber that biases lift in the positive Y direction. As the taper becomes more pronounced and wing stiffness increases, the lift contribution from the steady component increases while that of the unsteady component is reduced.

Table 2. Peak deflection, mean lift, mean power and peak leading edge force for various taper ratios assuming normal flapping kinematics. Rigid wing is assumed to have uniform thickness.

Taper ratio	1.0	0.6	0.2	Rigid
Peak deflection (mm)	14.6	10.4	5.6	0
Mean lift (mN)	7.19	10.1	9.47	8.89
Power (mW)	15.5	26.4	28.8	33.6
Peak leading edge force (mN)	54.8	49.2	36.7	33.2

Mean power is sensitive to taper ratio as well. The primary effect of wing deformation is seen at the mid-stroke ($t/T = 0,\ 0.5$), where peak power is lower for the flexible wings compared to the rigid wing. At that instant, the flexible wings are bent backwards due to aerodynamic forces, and their angle of attack is lower compared to that of the rigid wing. As a result, mean power is lower for the flexible wing compared to the rigid wing (table 2). While mean power reduces with taper ratio, peak leading edge forces increase. The most flexible wings experience the largest leading edge forces, where the peaks in forces coincide approximately with peak deflections. This indicates that the inertial and aerodynamic forces associated with elastic deformation increase the leading edge forces required to sustain the prescribed kinematics of O.

4.3. Deviations from hovering kinematics

In this section, we explore the sensitivity of the wing response to kinematic deviations from the hovering flapping kinematics shown in table 1. We characterize the influence of taper ratio on lift, power, leading edge force and mean lift-to-power for various sets of flapping kinematics.

4.3.1. Pitch amplitude

First, we investigate how pitch amplitude affects wing dynamics. Rigid-body pitch angle is difficult to characterize in flexible insect wings. We define rigid body pitch as the angle between the leading edge and trailing edge assuming the wing is rigid (figure 1). However, if the trailing edge deforms out-of-plane, the perceived pitch angle between the leading edge

IOP Publishing Bioinspir. Biomim. 17 (2022) 066007 J Reade and M Jankauski

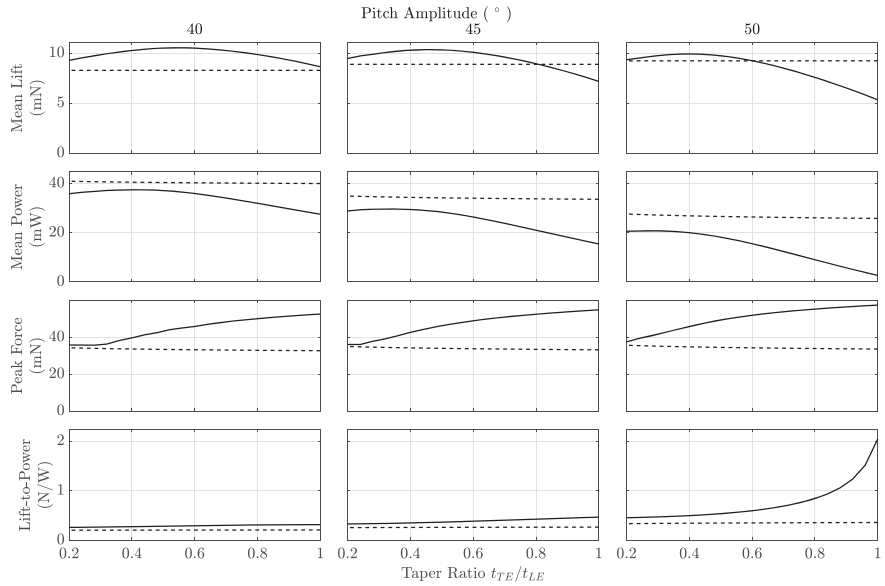


Figure 7. Study of pitch amplitude. The flexible and rigid wing values are represented by the solid and dashed lines, respectively.

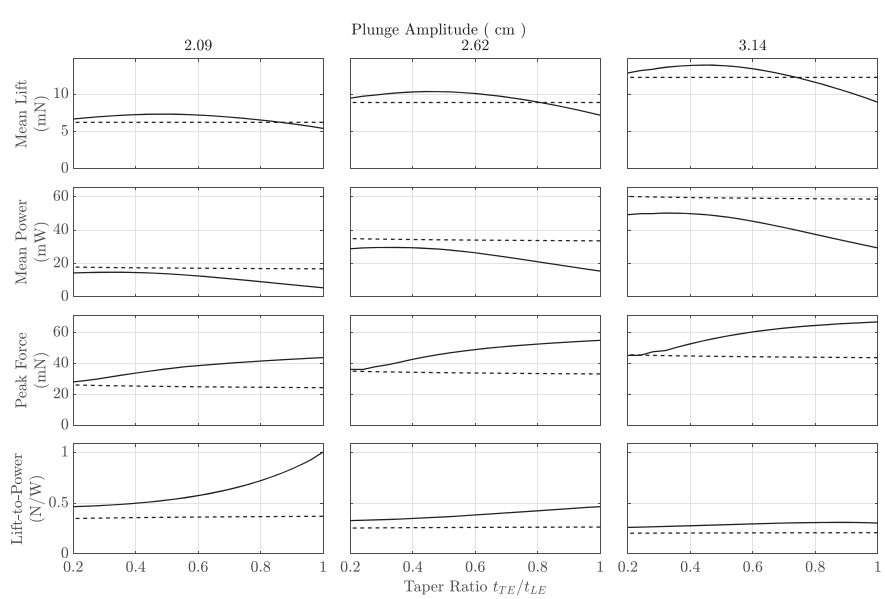


Figure 8. Study of plunge amplitude. The flexible and rigid wing values are represented by the solid and dashed lines, respectively.

and trailing edge will increase. All insect wings experience some deformation at the trailing edge in practice, and thus pitch amplitudes reported in the literature may overestimate rigid body pitch. We tested several values of rigid-body pitch amplitude to examine how wing performance is affected by variations in this quantity (figure 7).

Lift and power consumption are both strongly impacted by pitch amplitude. Pitch amplitude significantly affects mean lift in highly flexible wings,

but only modestly affects lift in stiffer wings. When highly tapered, the wing produced nearly constant lift regardless of the pitching amplitude. By contrast, the highly flexible homogeneous wing is more sensitive to pitch amplitude. The wing experiences similar deformation under both pitch angles, but the effective angle of attack is decreased by the higher pitch angle in addition to the deflection-induced camber and the downwash caused by the wake vortices. Around stroke reversal in the 50° pitching case, the aerodynamic force is heavily weighted towards the leading edge, reducing both lift and power consumption. A byproduct of this is that the taper ratio associated with maximum lift decreases with increasing pitch amplitude. These results also demonstrate that there is an optimal taper ratio which maximizes lift generation, and that this optimal taper ratio depends on pitch amplitude.

Power consumption of the flexible wing is lower than that of the rigid wing in all cases. The mean power versus taper ratio curve is concave, with the location of the maxima contingent on pitch amplitude. The low energy requirement of the flexible wing at high pitch amplitude is due to the wing bending out of the way and minimizing aerodynamic loads, though this adversely affects lift generation. Mean lift-to-power increases with taper ratio, but is relatively stationary in the range of taper ratios that produce sufficient lift to hover. Across the taper ratios considered, the mean lift-to-power of the flexible wing is higher than that of the rigid wing.

Peak leading edge force is largely unaffected by the pitching angle. Forces in general are dominated by the plunging inertial and aerodynamic forces rather than the pitching inertial force. The pitching motion accounts for only 19% of the peak leading edge force in a homogeneous flexible wing and 14% in a wing with a taper ratio of 0.2. On the other hand, peak leading edge force is sensitive to taper ratio. The lowest leading edge forces occur in the most tapered wing, presumably because the wing's center of mass is closer to the point of rotation. This reduces the inertial forces associated with pitching. The largest leading edge forces occur in the untapered wing, since the center of mass is further from the point of rotation and the wing experiences larger deflections.

4.3.2. Plunge amplitude

Some insects have been shown to increase their flapping amplitude to increase lift generation [31]. Within the pitch–plunge model, this is akin to increasing the plunge amplitude. We tested three different values of plunge amplitude to identify how variation of this parameter affected lift, mean power and peak leading edge forces (figure 8).

Plunge amplitude impacts each quantity strongly. Raising the plunge amplitude increases the distance and velocity of the wing during each stroke. As expected, this increases the lift, power, and leading edge force. Mean lift in flexible wings does not increase proportionally to the plunge velocity squared as might be expected from conventional steady aerodynamic theory. A possible reason for this is that the increased velocity generates higher aerodynamic forces on the wing, which in turn leads to higher deflections and reduced angle of attack, meaning that increasing the plunge amplitude and velocity results in diminishing returns. Mean lift in stiffer wings more closely scales with plunge velocity squared.

For a stationary airfoil subject to a uniform free-stream velocity, aerodynamic power scales with the free-stream velocity cubed [32]. We observe that the mean power scales nearly cubically with plunge velocity in rigid wings. In the highly tapered wing, the mean power requirement is nearly identical to that of a rigid wing at low plunge amplitudes. However, at higher plunge amplitudes, the disparity between power requirements is larger. The increased deflection arising from plunge amplitude likely decreases the effective drag on the wing, thereby reducing the power required by the flexible wing. This also explains why power decreases with taper ratio for all plunge amplitudes considered, though mean lift decreases above a certain taper ratio as well. The optimal taper ratio thus falls somewhere between providing sufficient lift to fly while requiring low energetic expenditures. Since the lift-to-power ratio increases monotonically with taper ratio for all plunge amplitudes considered, the optimal configuration corresponds to the highest taper ratio that satisfies the roughly 10 mN mean lift constraint.

Increasing the plunge amplitude increases the peak leading edge force for all wings considered, since the increased plunging amplitudes lead to larger linear accelerations and aerodynamic forces. As plunge amplitude increases, the contribution of the plunging force actually decreases slightly for all tested taper ratios. This is because the aerodynamic forces acting on the wing are more sensitive to increases in plunging amplitude than the plunging inertial forces are.

4.3.3. Pitch–plunge phase

Hawkmoths have been shown to adjust the relative phase of activation between their two flight muscle groups in response to visual stimuli [33], which influences the relative phase between their wing's flap and pitch rotations. It is plausible that modulation of the phase between kinematic parameters is responsible for some maneuvers during flight. Here, we explore how the relative phase between wing pitching and plunging motions affects flapping wing aeromechanics. Mean lift, power and peak leading edge forces are shown as a function of taper ratio for various pitch–plunge phase differences in figure 9.

Mean lift is fairly influenced by deviations in pitch–plunge phase. Increasing the phase to −75° increases the highest achievable lift in both flexible

IOP Publishing Bioinspir. Biomim. 17 (2022) 066007 J Reade and M Jankauski

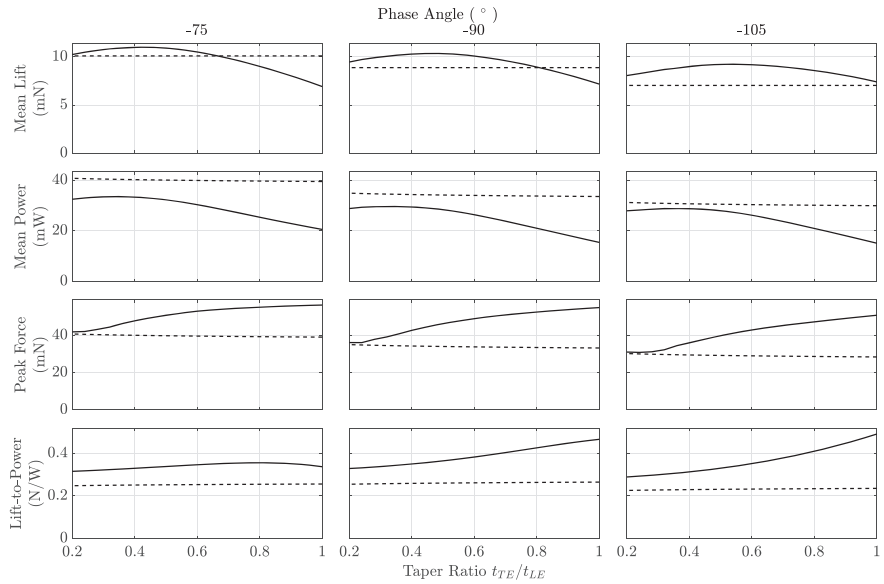


Figure 9. Study of pitch–plunge phase offset. The flexible and rigid wing values are represented by the solid and dashed lines, respectively.

and rigid wings, whereas decreasing the phase to −105° decreases highest achievable lift. Flexible wings across all taper ratios produce higher lift than rigid wings for a pitch–plunge phase of −105°, but for a pitch–plunge phase of −75°, flexible wings only produce mean lift than rigid wings for low taper ratios. Similar to trends observed in pitch amplitude, the taper ratio associated with greatest mean lift varies modestly with respect to pitch–plunge phase.

Mean power in general decreases when pitch–plunge phase is lowered. The largest reduction in mean power occurs in the rigid wing. The flexible wing have similar power requirements for −105° and −90° pitch–plunge phases, while power requirements for −75° are slightly higher, presumably due to an increase in lift and drag. The opposite trends in leading edge force are true, where leading edge force is reduced as the phase angle is decreased. As with all other parameter studies considered, the peak leading edge force increases with taper ratio as the wing becomes more flexible. The mean lift-to-power ratio is similar for all phase angles considered, particularly in the range of taper ratios that produce sufficient lift for hovering flight.

5. Discussion

5.1. Optimal lift production

Functionally graded flexural rigidity may improve flight performance in terms of aerodynamic force generation across a broad range of flapping wing kinematics. Figures 7–9 show that the mean lift produced by flexible wings is generally greater than that produced by rigid wings, though rigid wings may outperform flexible wings when deformation is extreme. Interestingly, there is an optimal taper ratio that maximizes the mean lift. For the normal flapping kinematics shown in table 1, this taper ratio is about 0.5, which corresponds to a natural frequency of 83 Hz and a flapping-to-natural frequency ratio of about 0.3. Prior studies show similar aerodynamic benefits when operating close to this ratio. Vanella *et al* showed that flapping at 1/3 the wing's natural frequency evokes a super-harmonic resonant response that improves the lift-to-drag ratio compared to a rigid wing with identical kinematics [2]. Dai *et al* found that flexible wings with flapping-to-natural frequency ratios equal to or less than 0.3 produced more lift than rigid wings [34]. Though our results generally agree with these findings, we saw that the exact lift-maximizing flapping-to-natural frequency ratio depends on flapping kinematics. For a pitching amplitude of 50°, the optimal flapping-to-natural frequency ratio is about 0.27; this increases to about 0.35 when the pitching amplitude is reduced to 40°. The optimal flapping-to-natural ratio changes with pitch–plunge phase as well, but is stationary with respect to plunge amplitude. This collectively shows that the wing's natural frequency is strongly associated with lift generation.

5.2. Trade-offs between power & force

In all cases tested, mean power and peak leading edge force were inversely proportional. With increasing

taper ratio, mean power decreased while peak leading edge force increased. The reduction of power at high taper ratios likely stems from a reduction of drag, though lift is lower at higher taper ratios as well. Large leading edge forces at high taper ratios result from the increased deflections and accompanying inertial forces.

The inverse relationship of mean power and peak leading edge force poses trade-offs for flight. Low mean power consumption implies the insect requires less energy storage, and low peak leading edge forces implies that the insect requires less muscle mass. Based on insect anatomy, we hypothesize that the flight mechanism is oriented more towards energetic efficiency. The thorax constitutes about 25%–30% of the total body mass in *M. sexta* [30] and the flight muscles occupy much of the thorax volume. The flight muscles can generate staggering forces, with one flight muscle group producing forces as high as 1 N [35]. These forces are 50 times greater than the total weight of the insect assuming a body mass of 2 grams. It is possible that the increased muscle force requirements resulting from wing flexibility are an acceptable trade-off for high aerodynamic force generation and relatively low power consumption.

5.3. Implications for robotics

The results of this study can inform the design and fabrication of insect-scale flapping wing micro air vehicles (FWMAVs). FWMAVs operating at low Reynolds numbers have reduced payload capacity, which makes conventional sensing and actuation technologies prohibitively heavy or energetically inefficient. Consequently, many FWMAVs rely on external tethers to supply power [16], which limits their autonomy and ability to perform useful tasks. Lightweight, flexible wing structures inspired by flying insects can reduce the power required to flap, thereby improving the energy economy of the robotic vehicle.

Artificial have been fabricated in a variety of ways, including additive manufacturing, laser cutting, molding or a combination thereof [25, 36, 37]. As manufacturing techniques become more sophisticated, the ability to tailor local wing stiffness through geometric or material modifications has improved. The capacity to modulate geometric or material properties may enable artificial wings to behave more similarly to their biological counterparts during flight. Chordwise functional rigidity plays a key role in some insect wings [38], and as shown within this work, may benefit aerodynamic force generation and energetic expenditures. Graded flexural rigidity in artificial wings can be realized by varying the taper ratio of vein structures that serve support scaffolding for surrounding membrane material.

In the design of functionally graded wings, one must first establish the range of taper ratios what produce enough lift to support the aircraft. Trade-offs between peak force and mean power should also be considered. As discussed, mean power and peak force scale inversely with one another as taper ratio is varied. From a robotics perspective, higher mean power draw requires increased energy storage, and larger peak forces require bigger actuators capable of delivering such forces. However, within the permissible range of taper ratios, higher taper ratios correspond to larger mean lift-to-power ratios. We consequently believe that the upper bound of taper ratio that provides enough lift for flight represents a design that balances the various requirements for power and force. However, true three-dimensional simulations should also be performed to understand how physics neglected by this two-dimensional model (e.g., spanwise bending and flow) may also influence wing performance.

5.4. Computational economy and model assumptions

The reduced-order FSI model developed through this work can be used to estimate how morphological or material properties beyond flexural rigidity impact flapping wing performance. Though the pitch–plunge idealization is used frequently to study of flapping wings, most implementations still rely on high-order computational solvers. UVLM has been incorporated into the pitch–plunge model to reduce the computational costs of the fluid solver on several occasions, but the AMM representation is less frequently used to lower the costs of the structural solver. Together, our model based on coupled UVLM/AMM can be solved in less than 1 s per wingbeat for the described discretization parameters, representing a large computational savings compared to higher-order solvers. When running on a laptop with a Ryzen 5800H 3.2 GHz CPU and 16 GB of DDR4 RAM, our model solves in roughly 10 s when considering 20 wing beat cycles. Further, to our knowledge, the flapping wing moments, leading edge forces and power for a flexible wing experiencing pitch–plunge motion have not previously been derived in modal coordinates. If wing deformation is known, these expressions can be used to compute quantities more efficiently than if using the canonical definitions, since spatial and temporal dependence can be decoupled and spatial integrals pre-computed.

While computationally efficient, our FSI model has limitations as well. First, the simplified 2D model neglects some dynamics associated with 3D flapping, such as spanwise bending, spanwise flow and wingtip losses. Previous studies have shown that spanwise flow may positively or negatively influence lift depending on the relative phase between bending and flapping [18]. Spanwise bending may be incorporated in future work and would best be accounted for by modifying plunge to be the sum of

rigid body flapping and elastic deformation, where the elastic deformation is a degree-of-freedom to be solved for. Spanwise flow and wingtip losses are more difficult to accommodate in a 2D setting, and consequently 2D models are most appropriate to generate approximate low-fidelity solutions quickly. The validity of the 2D solution, and how spanwise flow and wingtip loss may affect a specific wing configuration, should subsequently be assessed with higher-fidelity 3D modeling. Nonetheless, in many cases results from 2D have agreed with results generated by computational or experimental 3D studies with reasonable accuracy [39–41]. This suggests that at least some of the insights garnered from a 2D study can inform a 3D simulation. Next, the UVLM fluid model neglects viscous effects. While the inviscid assumption is appropriate for a broad range of flying insects including *M. sexta*, fluid viscosity may play a non-trivial role in the flight of very small insects [42]. Finally, the structural model is based on linear assumptions and cannot account for structural nonlinearity. As a result, some dynamic phenomena associated with large deformation may be lost. Further, numerous features observed in real wing structures, such as venation patterns, curvature, corrugation and graded material properties are neglected. Each of these may contribute to the wing's overall flexural rigidity, but should first be studied in isolation before a high-fidelity structural model of the wing is attainable.

6. Conclusion

Flapping insect wings are complex structures that deform from aerodynamic and inertial forces. In addition to the flapping motions of the wing, heterogeneous geometric and material properties influence how the wing deforms. Previous studies have shown that flexural rigidity in some insect wings varies as much as two orders of magnitude from the leading edge to the trailing edge [8]. However, the computational cost of many flapping wing FSI models have precluded us from understanding how these gradients in flexural rigidity regulate flapping wing performance. In this work, we developed a simplified 2D FSI model of a flapping wing as a pitching-plunging airfoil using AMM and UVLM. We derived expressions for the power, leading edge forces and moments required to flap the wing using modal coordinates. We used these models to understand how gradients in flexural rigidity affect flight energetics and the forces needed to sustain flight.

We found that wings with functionally graded flexural rigidity increased aerodynamic force generation and decreased power requirements relative to rigid wings or wings with uniform flexural rigidity. For normal hovering flapping kinematics, a wing with an optimal taper ratio of 0.5 produced about 20% more mean lift than a rigid wing and required about 15% less mean power. This taper ratio corresponded to a wing with a natural frequency of about 85 Hz, which is similar to the torsional natural frequency measured in *M. sexta* wings [25]. Variation of rigid body pitch amplitude and relative pitch–plunge phase affected the taper ratio that maximized lift production. Otherwise, trends in mean lift, mean power and peak leading edge force were not dramatically affected by deviations in flapping kinematics. This work suggests that functionally graded flexural rigidity, driven by spatial variations of wing thickness, enhances the performance of flapping wing insects.

Funding

This research was supported the National Science Foundation under awards Nos. CBET-1855383 and CMMI-1942810 to MJ. Any opinions, findings, and conclusions or recommendations expressed in this material are those of the author(s) and do not necessarily reflect the views of the National Science Foundation.

Data availability statement

The data that support the findings of this study are available upon reasonable request from the authors.

Appendix A. Aerodynamic modeling

This appendix details the derivation of the UVLM approach used to determine the aerodynamic forces acting on the wing. The flow velocity at any point i in space that is induced by a vortex at j is given by the Biot–Savart law:

$$\boldsymbol{V}_{\mathrm{ind}_{i,j}} = \frac{\Gamma_j}{2\pi L^2}\langle (Z_j - Z_i)\boldsymbol{e}_Y + (Y_i - Y_j)\boldsymbol{e}_Z\rangle, \quad \text{(A.1)}$$

where $\boldsymbol{V}_{\mathrm{ind}}$ is the induced velocity, L is the distance between point i and vortex j, Y and Z are the coordinates of i and j in the inertial reference frame, and Γ_j is the circulation of the vortex. Then, according to the Kelvin–Helmholtz theorem for an ideal fluid, the total circulation around a closed contour must remain constant, or

$$\frac{D\Gamma}{Dt} = 0. \quad \text{(A.2)}$$

Flow may not travel through the solid surface of the wing, meaning that the component of velocity normal to the surface is zero. This is represented by

$$(-\dot{\boldsymbol{R}} + \boldsymbol{V}_{\mathrm{ind}}) \cdot \boldsymbol{n} = 0 \quad \text{(A.3)}$$

where $\dot{\boldsymbol{R}}$ is the velocity of the wing's surface in the inertial reference frame and $\boldsymbol{n}$ is the surface normal vector. By simultaneously enforcing the non-penetration condition at all control points on the wing, as well as the Kelvin–Helmholtz condition, the

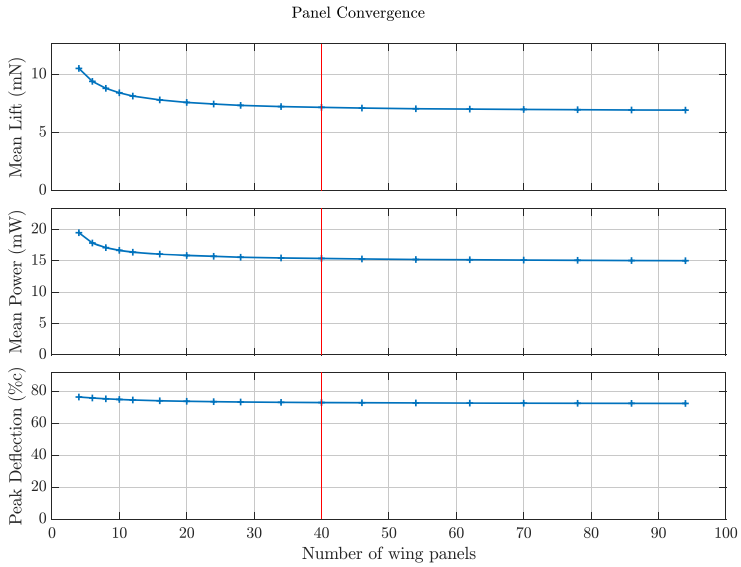


Figure C10. Dependence of mean lift, mean power and peak deflection on chordwise panel discretization. The red line indicates the number of panels used in this work.

strengths of the bound vortices can be determined via

$$\begin{bmatrix} a_{1,1} & a_{1,2} & \dots & a_{1,N_\mathrm{p}} & a_{1,N_\mathrm{p}+1} \\ a_{2,1} & a_{2,2} & \dots & a_{2,N_\mathrm{p}} & a_{2,N_\mathrm{p}+1} \\ \vdots & \vdots & \ddots & \vdots & \vdots \\ a_{N_\mathrm{p},1} & a_{N_\mathrm{p},2} & \dots & a_{Np,N_\mathrm{p}} & a_{Np,N_\mathrm{p}+1} \\ 1 & 1 & \dots & 1 & 1 \end{bmatrix} \begin{Bmatrix} \Gamma_1 \\ \Gamma_2 \\ \vdots \\ \Gamma_{N_\mathrm{p}} \\ \Gamma_{N_\mathrm{p}+1} \end{Bmatrix} = \begin{Bmatrix} \mathrm{rhs}_1 \\ \mathrm{rhs}_2 \\ \vdots \\ \mathrm{rhs}_{N_\mathrm{p}} \\ \mathrm{rhs}^* \end{Bmatrix} \tag{A.4}$$

where $a_{i,j}$ is the influence coefficient. On the right-hand side, $\mathrm{rhs}_{1,2\dots N_\mathrm{p}}$, are the normal velocities due to the combined effect of the pitch–plunge motion, structural deflection, and velocity induced by the wake vortices. rhs^* is the total bound vorticity from the previous time step. The solved quantities $\Gamma_{1,2\dots N_\mathrm{p}}$ and $\Gamma_{N_\mathrm{p}+1}$ are the strengths of the bound vortices on the wing and of the newly-shed wake vortex, respectively.

The new wake vortex is placed a fixed distance aft of the trailing edge. All existing wake vortices are advected with the local flow. The velocity of the ith wake vortex is given by

$$\boldsymbol{V}_i = \sum_{j=1}^{N_\mathrm{p}} \boldsymbol{V}_{\mathrm{ind}_{i,j}} + \sum_{k=1,k\neq i}^{N_w} \boldsymbol{V}_{\mathrm{ind}_{i,k}}, \tag{A.5}$$

where $\boldsymbol{V}_i$ is the total induced velocity at i by N_p bound vortices on the wing and $N_\mathrm{w} - 1$ wake vortices. A wake vortex is not influenced by its own vorticity. The aerodynamic force on the wing is determined using the unsteady Bernoulli equation,

$$\frac{P_\mathrm{ref} - P}{\rho} = \frac{V^2 - V_\mathrm{ref}^2}{2} + \frac{\partial \Phi}{\partial t}, \tag{A.6}$$

where P and P_ref are the local and reference pressures, V and V_ref are the local and reference (freestream) velocities, ρ is the fluid density, and Φ is the flow potential. When solved at the bound vortex for the ith wing panel, this becomes

$$\Delta P_i = -\rho \left[(-\dot{\boldsymbol{R}} + \boldsymbol{V}_{\mathrm{ind},\,i}) \cdot \boldsymbol{\tau}_i \frac{\Gamma_i}{\mathrm{d}s} + \frac{\partial}{\partial t} \sum_{j=1}^{i} \Gamma_j \right] \tag{A.7}$$

where ΔP is the pressure difference between the top and bottom surfaces of the wing and $\boldsymbol{\tau}$ is the unit vector tangent to the wing surface. The total aerodynamic force is obtained by summing the products of the pressure differentials and the panel normal vectors.

Appendix B. Finite element modeling

This appendix details how the mode shapes and natural frequencies of the 2D wing are determined. The stiffness matrix $\mathbf{K}_\mathrm{e}$ based on Euler–Bernoulli beam theory for an individual element is

$$\mathbf{K}_\mathrm{e} = \frac{E_e I_e}{c_\mathrm{e}^3} \begin{bmatrix} 12 & 6c_\mathrm{e} & -12 & 6c_\mathrm{e} \\ 6c_\mathrm{e} & 4c_\mathrm{e}^2 & -6c_\mathrm{e} & 2c_\mathrm{e}^2 \\ -12 & -6c_\mathrm{e} & 12 & -6c_\mathrm{e} \\ 6c_\mathrm{e} & 2c_\mathrm{e}^2 & -6c_\mathrm{e} & 4c_\mathrm{e}^2 \end{bmatrix} \tag{B.1}$$

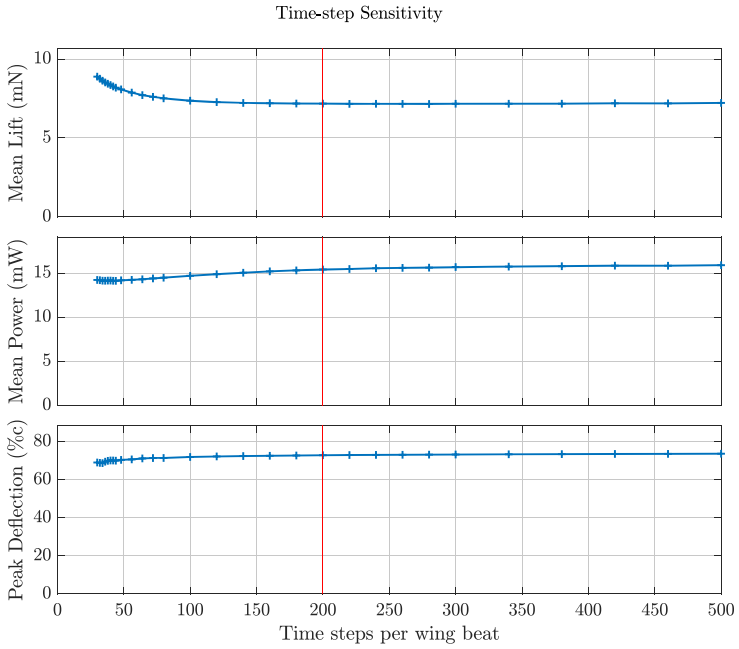


Figure C11. Dependence of mean lift, mean power and peak deflection on time step discretization. The red line indicates the number of panels used in this work.

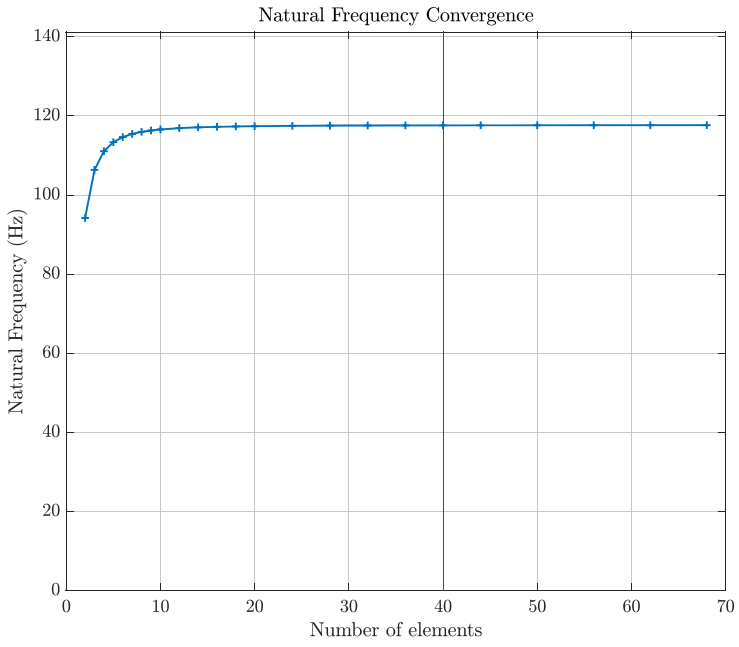


Figure C12. Dependence of the wing's first natural frequency on the number of elements. The red line indicates the number of elements used in this work.

Table C3. Discretization parameters.

Symbol	Description	Value
N_c	Number of elements	40
N_p	Number of panels	40
N_w	Number of wake vortices	100
T/dt	Time-steps per cycle	200

where I_e, E_e, and c_e are the elemental area moment of inertia, elastic modulus, and length respectively. In the I_e calculation, the cross-sectional area of the wing in the x–z plane is assumed rectangular. E_e and c_e are uniform across all elements. The elemental mass matrix $\mathbf{M}_e$ is

$$\mathbf{M}_e = \frac{\rho_w b t_e c_e}{420}\begin{bmatrix} 156 & 22c_e & 54 & -13c_e \\ 22c_e & 4c_e^2 & 13c_e & -3c_e^2 \\ 54 & 13c_e & 156 & -22c_e \\ -13c_e & -3c_e^2 & -22c_e & 4c_e^2 \end{bmatrix} \tag{B.2}$$

where ρ_w is the wing material density, b is the wing span, and t_e is the element thickness. The wing vibration modes and natural frequencies are determined by finding the eigenvectors and eigenvalues of the matrix quantity $\mathbf{M}^{-1}K$.

Appendix C. Discretization parameter convergence studies

This appendix shows the convergence studies used to determine panel count, number of time steps and number of elements. All discretization parameters are shown in table C3. Sensitivity of lift, power, and deflection as a function panel count are shown in figure C10, and as a function of time step size in figure C11. The wing's first natural frequency as a function of element count is shown in figure C12. In both the panel count and time step analyses, a homogeneous wing is used, as the most flexible wing should experience the greatest deformation and dependence on panel count. In the element count analysis, a highly-tapered wing is used, since natural frequency converges fastest with the homogeneous wing. In the time-step sensitivity analysis, the number of time-steps per wing beat is varied from 30 to 500. The number of wake vortices N_w was fixed to half of this value to prevent the results being affected by the wing flying back through its wake.

Appendix D. Validation

In this section, we benchmark our model using results from high fidelity CFD from [7]. The two-dimensional wing is uniform thickness and stiffness. The pitch and plunge amplitudes are 22.5° and 1.25c, respectively. The driving-to-natural frequency ratio is 0.4, and the mass number (a measure of the relative magnitude of inertial to aerodynamic forces) is 1. We use the same geometric parameters as shown in table 1, as the comparison study used non-dimensional quantities. We apply low-pass filter to the lift coefficient with a cutoff frequency about 16 times that of the flapping frequency.

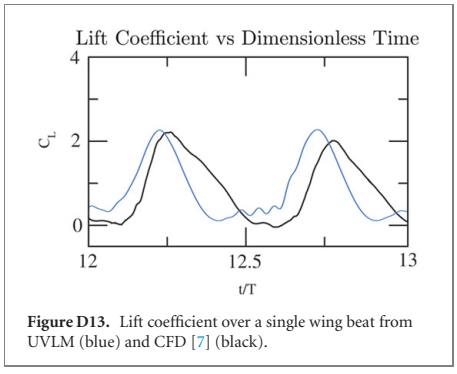


Figure D13. Lift coefficient over a single wing beat from UVLM (blue) and CFD [7] (black).

We compare then the lift coefficient predicted by both models using the maximum plunge rate as the reference velocity (figure D13). Both methods results in similar lift coefficients, though the lift coefficient by UVLM slightly lags the phase of that predicted by the higher fidelity model. Given the computational savings of the reduced-order model, we consider these results to be sufficiently similar.

ORCID iDs

Mark Jankauski https://orcid.org/0000-0001-6305-0564

References

[1] Combes S A and Daniel T L 2003 Into thin air: contributions of aerodynamic and inertial-elastic forces to wing bending in the Hawkmoth Manduca sexta *J. Exp. Biol.* **206** 2999–3006
[2] Vanella M, Fitzgerald T, Preidikman S, Balaras E and Balachandran B 2009 Influence of flexibility on the aerodynamic performance of a hovering wing *J. Exp. Biol.* **212** 95–105
[3] Mountcastle A and Daniel T 2010 Vortexlet models of flapping flexible wings show tuning for force production and control *Bioinspir. Biomim.* **5** 045005
[4] Mountcastle A M and Combes S A 2013 Wing flexibility enhances load-lifting capacity in bumblebees *Proc. R. Soc.* B **280** 20130531
[5] Jankauski M, Guo Z and Shen I 2018 The effect of structural deformation on flapping wing energetics *J. Sound Vib.* **429** 176–92
[6] Reid H E, Schwab R K, Maxcer M, Peterson R K, Johnson E L and Jankauski M 2019 Wing flexibility reduces the energetic requirements of insect flight *Bioinspir. Biomim.* **14** 056007
[7] Yin B and Luo H 2010 Effect of wing inertia on hovering performance of flexible flapping wings *Phys. Fluids* **22** 111902
[8] Combes S and Daniel T 2003 Flexural stiffness in insect wings II. Spatial distribution and dynamic wing bending *J. Exp. Biol.* **206** 2989–97

[9] Tian F-B, Dai H, Luo H, Doyle J F and Rousseau B 2014 Fluid–structure interaction involving large deformations: 3D simulations and applications to biological systems *J. Comput. Phys.* **258** 451–69

[10] Ishihara D, Horie T and Denda M 2009 A two-dimensional computational study on the fluid–structure interaction cause of wing pitch changes in dipteran flapping flight *J. Exp. Biol.* **212** 1–10

[11] Hamamoto M, Ohta Y, Hara K and Hisada T 2007 Application of fluid–structure interaction analysis to flapping flight of insects with deformable wings *Adv. Robot.* **21** 1–21

[12] Fitzgerald T, Valdez M, Vanella M, Balaras E and Balachandran B 2011 Flexible flapping systems: computational investigations into fluid–structure interactions *Aeronaut. J.* **115** 593–604

[13] Tang J, Chimakurthi S, Palacios R, Cesnik C and Shyy W 2008 Computational fluid–structure interaction of a deformable flapping wing for micro air vehicle applications *46th AIAA Aerospace Sciences Meeting and Exhibit* vol 615

[14] Jankauski M and Shen I 2014 Dynamic modeling of an insect wing subject to three-dimensional rotation *Int. J. Micro Air Vehicles* **6** 231–51

[15] Anderson J D and Wendt J 1995 *Computational Fluid Dynamics* vol 206 (Berlin: Springer)

[16] Platzer M F, Jones K D, Young J and Lai J C 2008 Flapping wing aerodynamics: progress and challenges *AIAA J.* **46** 2136–49

[17] Tian F-B, Luo H, Song J and Lu X-Y 2013 Force production and asymmetric deformation of a flexible flapping wing in forward flight *J. Fluids Struct.* **36** 149–61

[18] Roccia B A, Preidikman S, Verstraete M L and Mook D T 2017 Influence of spanwise twisting and bending on lift generation in MAV-like flapping wings *J. Aerospace Eng.* **30** 04016079

[19] Birch J M and Dickinson M H 2001 Spanwise flow and the attachment of the leading-edge vortex on insect wings *Nature* **412** 729–33

[20] Kweon J and Choi H 2010 Sectional lift coefficient of a flapping wing in hovering motion *Phys. Fluids* **22** 071703

[21] Hoffmann J, Donoughe S, Li K, Salcedo M K and Rycroft C H 2018 A simple developmental model recapitulates complex insect wing venation patterns *Proc. Natl Acad. Sci. USA* **115** 9905–10

[22] Reade J and Jankauski M A 2020 Deformable blade element and unsteady vortex lattice fluid–structure interaction modeling of a 2D flapping wing *Int. Design Engineering Technical Conf. Computers and Information in Engineering Conf.* vol 83969 (American Society of Mechanical Engineers) V007T07A032

[23] Katz J and Plotkin A 2001 *Low-Speed Aerodynamics* vol 13 (Cambridge: Cambridge University Press)

[24] Willmott A P and Ellington C P 1997 The mechanics of flight in the Hawkmoth Manduca sexta. I. Kinematics of hovering and forward flight *J. Exp. Biol.* **200** 2705–22

[25] Reid H, Zhou H, Maxcer M, Peterson R K, Deng J and Jankauski M 2021 Toward the design of dynamically similar artificial insect wings *Int. J. Micro Air Vehicles* **13**

[26] Casey C, Yager C, Jankauski M and Heveran C M 2022 The flying insect thoracic cuticle is heterogeneous in structure and in thickness-dependent modulus gradation *Acta Biomaterialia* 422–9

[27] Vincent J and Wegst U 2004 Design and mechanical properties of insect cuticle *Arthropod Struct. Dev.* **33** 187–99

[28] Norris A G, Palazotto A N and Cobb R G 2013 Experimental structural dynamic characterization of the hawkmoth (Manduca sexta) forewing *Int. J. Micro Air Vehicles* **5** 39–54

[29] Bergou A J, Xu S and Wang Z J 2007 Passive wing pitch reversal in insect flight *J. Fluid Mech.* **591** 321–37

[30] Hedrick T L and Daniel T 2006 Flight control in the Hawkmoth Manduca sexta: the inverse problem of hovering *J. Exp. Biol.* **209** 3114–30

[31] Altshuler D L, Dickson W B, Vance J T, Roberts S P and Dickinson M H 2005 Short-amplitude high-frequency wing strokes determine the aerodynamics of honeybee flight *Proc. Natl Acad. Sci. USA* **102** 18213–8

[32] Schmitz S 2020 *Aerodynamics of Wind Turbines: A Physical Basis for Analysis and Design* (New York: Wiley)

[33] Ando N and Kanzaki R 2016 Flexibility and control of thorax deformation during Hawkmoth flight *Biol. Lett.* **12** 20150733

[34] Dai H, Luo H and Doyle J F 2012 Dynamic pitching of an elastic rectangular wing in hovering motion *J. Fluid Mech.* **693** 473–99

[35] Tu M S and Daniel T L 2004 Submaximal power output from the dorsolongitudinal flight muscles of the Hawkmoth Manduca sexta *J. Exp. Biol.* **207** 4651–62

[36] Tanaka H and Wood R J 2010 Fabrication of corrugated artificial insect wings using laser micromachined molds *J. Micromech. Microeng.* **20** 075008

[37] Pornsin-Sirirak T N, Tai Y, Nassef H and Ho C 2001 Titanium-alloy MEMS wing technology for a micro aerial vehicle application *Sensors Actuators* A **89** 95–103

[38] Combes S and Daniel T 2003 Flexural stiffness in insect wings I. Scaling and the influence of wing venation *J. Exp. Biol.* **206** 2979–87

[39] Wang Z J, Birch J M and Dickinson M H 2004 Unsteady forces and flows in low Reynolds number hovering flight: two-dimensional computations vs robotic wing experiments *J. Exp. Biol.* **207** 449–60

[40] Whitney J P and Wood R J 2010 Aeromechanics of passive rotation in flapping flight *J. Fluid Mech.* **660** 197–220

[41] Liu L and Sun M 2018 The added mass forces in insect flapping wings *J. Theor. Biol.* **437** 45–50

[42] Santhanakrishnan A, Robinson A K, Jones S, Low A A , Gadi S, Hedrick T L and Miller L A 2014 Clap and fling mechanism with interacting porous wings in tiny insect flight *J. Exp. Biol.* **217** 3898–909

QUASI-3D DEFORMABLE BLADE ELEMENT AND UNSTEADY VORTEX LATTICE REDUCED-ORDER MODELING OF FLUID-STRUCTURE INTERACTION IN FLAPPING WINGS

Contribution of Authors and Co-Authors

Manuscript in following chapter

Author: Ryan Schwab

Contributions: Integrated computational fluid dynamics and finite element analysis solvers into a high fidelity flapping wing model used to validate reduced order models

Author: Joseph Reade

Contributions: Developed quasi-3D Unstead Vortex Latice Method reduced order model for flapping wings, two-way coupled to a modal-truncation based structural solver

Author: Mark Jankauski

Contributions: Developed blade element theory reduced order model for flapping wings and modal-truncation based structural solver, and two-way coubled these to form "Deformable Blade Element Theory" model

Manuscript Information

R. Schwab, J. Reade, M. Jankauski

Physics of Fluids

Status of Manuscript:
____ Prepared for submission to a peer-reviewed journal
____ Officially submitted to a peer-reviewed journal
____ Accepted by a peer-reviewed journal
_X_ Published in a peer-reviewed journal

American Institute of Physics
Submitted: October 3rd, 2022
Published: 7 December 2022
Volume: 34
doi: 10.1063/5.0129128

Physics of Fluids

RESEARCH ARTICLE | DECEMBER 07 2022

Quasi three-dimensional deformable blade element and unsteady vortex lattice reduced-order modeling of fluid–structure interaction in flapping wings

R. Schwab ; J. Reade ; M. Jankauski

Check for updates

Physics of Fluids 34, 121903 (2022)
https://doi.org/10.1063/5.0129128

View Online
Export Citation

08 July 2024 15:29:04

AIP Publishing



Physics of Fluids
Special Topic:
Kitchen Flows 2024
Guest Editors: Gerald G. Fuller, Maciej Lisicki, Arnold J.T.M. Mathijssen, Endre Joachim Mossige, Rossana Pesquino, Vivek Nagendra Prakash, Laurence Ramos
Submit Today!
AIP Publishing

Physics of Fluids ARTICLE scitation.org/journal/phf

Quasi three-dimensional deformable blade element and unsteady vortex lattice reduced-order modeling of fluid–structure interaction in flapping wings

Cite as: Phys. Fluids **34**, 121903 (2022); doi: 10.1063/5.0129128
Submitted: 3 October 2022 · Accepted: 21 November 2022 ·
Published Online: 7 December 2022

View Online Export Citation CrossMark

R. Schwab, J. Reade, and M. Jankauski[a)]

AFFILIATIONS

Department of Mechanical & Industrial Engineering, Montana State University, 220 Roberts Hall, Bozeman, Montana 59717, USA

[a)]Author to whom correspondence should be addressed: mark.jankauski@montana.edu

ABSTRACT

Flapping, flexible insect wings deform under inertial and fluid loading. Deformation influences aerodynamic force generation and sensorimotor control, and is thus important to insect flight mechanics. Conventional flapping wing fluid–structure interaction models provide detailed information about wing deformation and the surrounding flow structure, but are impractical in parameter studies due to their considerable computational demands. Here, we develop two quasi three-dimensional reduced-order models (ROMs) capable of describing the propulsive forces/moments and deformation profiles of flexible wings. The first is based on deformable blade element theory (DBET) and the second is based on the unsteady vortex lattice method (UVLM). Both rely on a modal-truncation based structural solver. We apply each model to estimate the aeromechanics of a thin, flapping flat plate with a rigid leading edge, and compare ROM findings to those produced by a coupled fluid dynamics/finite element computational solver. The ROMs predict wing deformation with good accuracy even for relatively large deformations of 25% of the chord length. Aerodynamic loading normal to the wing's rotation plane is well captured by the ROMs, though model errors are larger for in-plane loading. We then perform a parameter sweep to understand how wing flexibility and mass affect peak deflection, mean lift and average power. All models indicate that flexible wings produce less lift but require lower average power to flap. Importantly, these studies highlight the computational efficiency of the ROMs—compared to the convention modeling approach, the UVLM and DBET ROMs solve 4 and 6 orders of magnitude faster, respectively.

Published under an exclusive license by AIP Publishing. https://doi.org/10.1063/5.0129128

08 July 2024 15:29:04

I. INTRODUCTION

Flying insects often serve as model organisms in the study of sensorimotor and neuromuscular control because they have relatively simple neural systems, yet are able to perform sophisticated tasks.[1] Insects may utilize halteres to sense angular velocities of their bodies,[2] campaniform sensilla to detect strains of their legs and exoskeleton,[3] and Johnston's organs to detect vibrations in the antennae to sense airflow.[4] Some insects utilize campaniform sensilla (strain-sensitive mechanoreceptors) distributed across their wings to encode deformations such that they can adjust their flapping kinematics for improved flight control.[5–7] Information regarding the insect body's angular velocity is also believed to be encoded in wing deformation,[8,9] hence making wing-based mechanoreception an essential sensory modality in insects that lack dedicated gyroscopic sensing organs. Wing flexibility and deformation are, therefore, critical to flight in many insect species.

In addition to sensory functions, deformation also influences wings' aerodynamic performance. Insect wings undergo large deformations due to both aerodynamic and inertial forces.[10–12] The surrounding fluid affects the wing deformation and vice versa, leading to a strong fluid–structure coupling. Wing flexibility may reduce the energetic requirements of flapping, since strain energy stored in the wing during elastic deformations may be recovered later in the wingbeat.[13] Wing flexibility also has a significant influence on thrust production through passive wing pitching and bending, which lowers drag forces and strengthens vortex production near the wing surface, thereby increasing lift forces.[14–16] Wing mass and the relative contribution of inertial and aerodynamic forces also play a role in efficiency. Lift-to-drag ratio is higher in cases where aerodynamic forces dominate deformation (e.g., low wing mass), likely due to smaller shed vortices and thus lower drag forces.[17] Additionally, flexibility may benefit

Physics of Fluids ARTICLE scitation.org/journal/phf

wing–wing interactions, such as during clap and fling type flapping, to enhance force generation. Studies show that wing deformation improves leading edge vortex (LEV) attachment and wake capture, where the wing interacts with shed vortices from the previous flap cycle to enhance force production.[18]

Owing to the experimental limitations in real insects, the characterization of structural and fluid phenomena surrounding flapping wings often relies on computational modeling.[11,19–26] Fluid modeling usually involves computational fluid dynamics (CFD) to solve the Navier–Stokes equations—a set of partial differential equations that describe the conservation of mass and conservation of momentum in fluid flows.[27] This fluid model is often used in conjunction with structural solvers such as finite element analysis (FEA) to evaluate bilateral fluid–structure interactions (FSIs).[11,19,22] Computational models have driven much of our current understanding of flapping wing mechanics, such as the development of LEVs[28] and the influence of venation patterns on spatially variable stiffness.[29] Additionally, computational models provide a platform to compare the performance of flexible wings to idealized rigid wings, where the latter are mathematically convenient but unrealistic in natural contexts.[11,30] While these computational models are an accepted instrument for studying flapping wing flight, they necessitate considerable computational resources, often requiring several days to reach converged solutions for each simulation. They are consequently challenged by studies that consider large parameter spaces, for example variable wing morphologies, flapping kinematics and material properties.

Because of the solution times required by higher-order flapping wing models, reduced-order models (ROMs) have emerged as useful frameworks to efficiently perform parametric and optimization studies. The two most common ROMs in flapping wing flight are based on quasi-static blade element theory (BET) and unsteady vortex lattice method (UVLM).[22,26,31–34] BET functions by discretizing a wing into airfoils that run along the wing's chord. The local aerodynamic forces and moments are determined via thin airfoil theory and are subsequently integrated over the wing surface to give the net forces and moments. BET is typically used to model rigid wings but has been extended to flexible wings in some contexts. For example, a BET-based formulation was used to model flexible wings experiencing single-degree-of-freedom rotation,[35] but because of the simplified kinematics, such a model cannot accommodate lifting flow. Wang *et al.* used BET to describe the aerodynamics of twistable wings subject to multiple-degree-of-freedom rotation,[36] though the structural model in this work is not amendable to the anisotropic or spatially variable material properties present in real insect wings.[37] Walker and Taylor developed a similar BET model for twistable wings, where the twist angle must be prescribed within this approach.[38]

UVLM estimates pressure over the wing surface by treating the wing and shed wake as an infinitely thin sheet of discrete vortices. These vortices cause a velocity gradient across the wing and thus a pressure differential. This method has the advantage of being significantly faster than high-fidelity CFD while still accounting for many unsteady phenomena.[22,39] Compared to BET, UVLM is more commonly used to describe the mechanics of two-dimensional (2D) or three-dimensional (3D) flexible wings,[22,26,33] but is more computationally expensive as well. One method to reduce the computational costs of UVLM (perhaps at the expense of accuracy) is to use a quasi three-dimensional approximation, similar to the one employed by BET. For a wing discretized spanwise into n segments, a quasi-3D approach reduces the number of required calculations by at least a factor of n. Vector calculations being reduced to two dimensions further enhance computational savings. However, to our knowledge, no such model has been developed for flapping wing flight.

Given the importance of wing flexibility in insect flight and the limitations of existing flapping wing fluid–structure interaction (FSI) models, the goal of the present work is to develop two quasi-3D ROMs of flapping, flexible wings and to benchmark the accuracy and computational times enabled by these models against a more conventional high-fidelity (HiFi hereafter) approach. Each ROM must be capable of estimating wing deformation and the bulk propulsive forces and moments of flapping. The first ROM is rooted in BET but accommodates wing deformation; we, therefore, refer to this model as deformable blade element theory (DBET hereafter). The second ROM is based on a quasi-3D UVLM approach (simply UVLM hereafter).

The remainder of the paper is organized as follows. First, we formulate the ROMs and describe the basis of the HiFi computational model. Then, we apply each model to predict the deformation and aerodynamics of a thin rectangular plate flapping in a quiescent environment. We assume the wing has a rigid leading edge, since the vibration modes measured in insect wings indicate that deformation is more pronounced at the trailing edge relative to the leading edge.[40,41] Though the ROMs may generalize to more complex wing structures (e.g., realistic planforms, vein structures), it is prudent to first benchmark their accuracy in a simplified context. We then compare propulsive forces and wing deformations estimated by each model, and perform a parametric study to quantify how wing stiffness and mass affect lift, peak deflection and average power requirements. Finally, we discuss the utility of these models within the field of insect flight and address some of the model limitations.

II. MATHEMATICAL MODELING

A. Flapping kinematics

First, we establish a wing-fixed system that rotates with the wing's rigid body motion (Fig. 1). The reference frame kinematics are identical across all modeling efforts and originated in Ref. 42. A wing is situated in an $X-Y-Z$ inertial coordinate system. The $X-Y-Z$ coordinate system undergoes a finite rotation α about the positive X direction, where α denotes the roll angle (also called flap angle) of the wing. The resulting $x''-y''-z''$ coordinate system is then rotated about y'' by angle β, where β represents wing pitch (also called wing rotation). The ensuing $x'-y'-z'$ system experiences finite rotation γ about the z' axis, where γ is wing yaw (sometimes stroke deviation). The terminal wing-fixed $x-y-z$ coordinate system is bound to the wing's rigid body rotation, where the wing is rotating about fixed point O. The unit vectors in the wing fixed frame are $\mathbf{e}_x$, $\mathbf{e}_y$, $\mathbf{e}_z$ and are directed along the x, y, and z axes, respectively. The angular velocity $\boldsymbol{\Omega}$ is

$$\boldsymbol{\Omega} = \underbrace{(\dot{\alpha}\cos\beta\cos\gamma + \dot{\beta}\sin\gamma)}_{\Omega_x}\mathbf{e}_x + \underbrace{(\dot{\beta}\cos\gamma - \dot{\alpha}\cos\beta\sin\gamma)}_{\Omega_y}\mathbf{e}_y + \underbrace{(\dot{\gamma} + \dot{\alpha}\sin\beta)}_{\Omega_z}\mathbf{e}_z, \tag{1}$$

where Ω_x, Ω_y, and Ω_z are the x, y, and z components of angular velocity with respect to the wing-fixed coordinate system.

08 July 2024 15:29:04

Published under an exclusive license by AIP Publishing

Physics of Fluids ARTICLE scitation.org/journal/phf

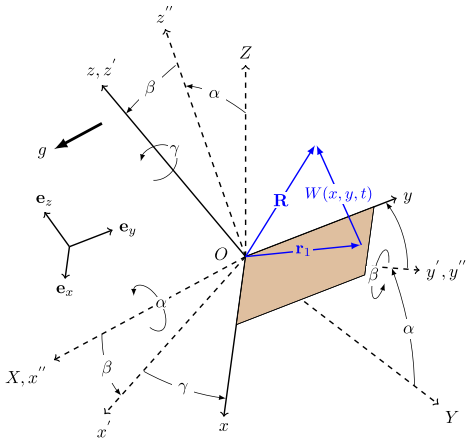


FIG. 1. Development of a $x - y - z$ coordinate system that rotates with the wing's rigid body motion. **R** is a position vector between the wing's fixed point of rotation O and a differential mass dm. Per our coordinate convention, gravity g acts in the $-X$ direction.

B. Reduced-order modeling

1. Structural modeling

Next, we derive a reduced-order structural modeling of the rotating, flexible wing. The structural model is general in the sense that it can incorporate any planar wing geometry and can interface with any appropriate fluid dynamic model. Within this work, we use this structural model in conjunction with the DBET and UVLM aerodynamic solvers. The benefit to this approach is that we must solve only for the time-response of the wing's vibration mode shapes rather than the time-response of the wing's individual degrees-of-freedom (assuming the wing can be discretized as a multiple-degree-of-freedom system). In practice, the number of modes needed to represent wing deformation is usually much smaller than the number of physical degrees of freedom, thereby representing a computational savings within the structural domain. The wing's vibration modes can be pre-computed analytically for simple structures or via finite element for more complex structures. The structural model framework originated in Ref. 43 and was extended in Ref. 44, and is summarized here to provide context to the present work. For a more thorough derivation, the reader is encouraged to refer to these references.

Consider a position vector **R** from the wing's fixed point of rotation O to a differential mass element dm located on the wing (Fig. 1). Position vector **R** is

$$\mathbf{R} = \underbrace{x\mathbf{e}_x + y\mathbf{e}_y}_{\mathbf{r}_1} + W(x,y,t)\mathbf{e}_z, \tag{2}$$

where x and y are the planar coordinates of dm (also described by position vector $\mathbf{r}_1$) and $W(x,y,t)$ is a small, unknown out-of-plane elastic deformation dependent on both space and time. The wing's in-plane motion is neglected. The velocity of dm is

$$\dot{\mathbf{R}} = \boldsymbol{\Omega} \times \mathbf{R} + \dot{W}(x,y,t)\mathbf{e}_z. \tag{3}$$

The wing's kinetic energy T is

$$T = \frac{1}{2}\int_m \dot{\mathbf{R}} \cdot \dot{\mathbf{R}}\, dm, \tag{4}$$

where the above represents an integration of the differential kinetic energy of dm over the wing's mass domain. Next, the potential energy U resulting from the wing's elastic deformation is

$$U = \frac{1}{2}\int_V \sigma(W,W)\, dV, \tag{5}$$

where σ is a symmetric, quadratic strain energy density function dependent on wing deformation $W(x,y,t)$ and V is the wing's volume. Next, we represent elastic deformation $W(x,y,t)$ via an eigenfunction expansion such that it can be calculated as space dependent mode shapes $\phi_k(x,y)$ multiplied by their time-dependent modal responses $q_k(t)$, given by

$$W(x,y,t) = \sum_{k=1}^{\infty} \phi_k(x,y) q_k(t). \tag{6}$$

Vibration modes $\phi_k(x,y)$ can be calculated via finite element or in some cases analytically. Mode shapes are normalized with respect to the wing's mass such that they satisfy

$$\int_m \phi_k \phi_r\, dm = \delta_{kr}, \tag{7}$$

$$\int_V \sigma(\phi_k, \phi_r)\, dV = \omega_k^2\, \delta_{kr}, \tag{8}$$

where δ_{kr} is the Kronecker delta function, and ω_k is the kth natural frequency associated with mode shape ϕ_k.

Finally, we expand the kinetic and potential energies in terms of Eq. (6) and apply Lagrange's equation to determine the equation of motion governing modal response q_k as follows:

$$\ddot{q}_k + 2\zeta_k\omega_k\dot{q} + \left[\omega_k^2 - (\Omega_x^2 + \Omega_y^2)\right] q_k = \dot{\boldsymbol{\Omega}} \cdot \mathbf{b_k} - \Omega_z\, \boldsymbol{\Omega} \cdot \mathbf{a}_k + Q_k, \tag{9}$$

where $\mathbf{a_k}$, $\mathbf{b_k}$ are constant vectors related to the position of the inertial force center of the kth vibration mode defined by

$$\mathbf{a}_k = \int_m \phi_k (x\,\mathbf{e}_x + y\,\mathbf{e}_y)\, dm, \tag{10}$$

$$\mathbf{b}_k = \int_m \phi_k (-y\,\mathbf{e}_x + x\,\mathbf{e}_y)\, dm. \tag{11}$$

The first term in the equation of motion is the modal acceleration. The second term is an empirical viscous damping term, where ζ_k is the wing's kth modal damping ratio. The third term is a time-varying stiffness term dependent on the wing's angular velocity. The modal excitation terms to the right-hand side of the equation of motion are the Euler force, the centrifugal force, and the kth non-conservative aerodynamic force Q_k. Non-conservative aerodynamic modal force Q_k can be determined via the principle of virtual work as follows:

$$Q_k = \int_{S_w} dF_z(x,y,t)\phi_k(x,y)\, dS_w, \tag{12}$$

08 July 2024 15:29:04

Published under an exclusive license by AIP Publishing

Physics of Fluids ARTICLE scitation.org/journal/phf

where dF_z is the differential aerodynamic force acting in the z direction and S_w is the wing's surface. The physical aerodynamic force F_z can be determined via any fluid model, including DBET and UVLM.

Finally, we determine the inertial moments $\mathbf{M}_0$ acting at the wing's point of rotation O. The inertial moments are needed to calculate the instantaneous power delivered to the flapping wing. We use a derivation from,[13] which derives $\mathbf{M}_0$ starting from angular momentum $\mathbf{H}_0$. The angular momentum of a rotating, flexible wing is

$$\mathbf{H}_0 = \int_m \mathbf{R} \times \dot{\mathbf{R}}\, dm, \tag{13}$$

which can be expanded via the wing's mode shapes and modal responses as follows:

$$\mathbf{H}_0 = \mathbf{I}_0\boldsymbol{\Omega} + \sum_{k=1}^{\infty}\left[-q_k(\mathbf{a}_k \cdot \boldsymbol{\Omega})\mathbf{e}_z - \mathbf{b}_k\dot{q}_k - (\mathbf{e}_z \cdot \boldsymbol{\Omega})\mathbf{a}_k q_k + (\boldsymbol{\Omega} - \omega_z\mathbf{e}_z)q_k^2\right], \tag{14}$$

with $\mathbf{I}_0$ being the inertial tensor of the wing. The inertial moments about fixed point O can then be determined by differentiating angular momentum $\mathbf{H}_0$ with respect to time, yielding

$$\mathbf{M}_0 = \boldsymbol{\Omega} \times \mathbf{H}_0 + \dot{\mathbf{H}}_{0,xyz}. \tag{15}$$

2. Deformable blade element theory

Blade element theory (BET) is a quasi-static modeling approach that is used frequently to estimate the aerodynamic forces and moments acting on flapping wings.[38,45,46] BET is usually formulated via multiple sets of algebraic equations and is thus computationally efficient. On the other hand, BET has several limitations; it neglects spanwise flows, vortex shedding, wing–wake interactions, and other phenomena that rely on the time history of the surrounding fluid. Further, BET does not provide information about the spatial force distribution acting over the wing. Nonetheless, BET provides order-of-magnitude propulsive force estimates and has been applied extensively to describe the aerodynamics of rigid wings. In the present work, we expand the BET approach to accommodate wing deformation. We refer to this framework as deformable blade element theory (DBET). We neglect added mass and rotational lift terms, which are included in some BET formulations.

A quasi-static differential aerodynamic force dF acting on an airfoil (Fig. 2) is described by

$$dF_{[\cdot]} = \frac{1}{2}\rho_f C_{[\cdot]}(\mathcal{A})\mathbf{V}_\infty \cdot \mathbf{V}_\infty\, dS, \tag{16}$$

where ρ_f is fluid density, $\mathbf{V}_\infty$ is the induced or free stream velocity, $C_{[\cdot]}$ is an aerodynamic coefficient ($[\cdot]$ is a placeholder to indicate either lift or drag) dependent on angle of attack $\mathcal{A}$, and dS is the differential surface over which the differential aerodynamic force acts. Assuming the wing flaps in a quiescent environment, the induced fluid velocity is equal in magnitude and opposite in direction to the wing's velocity, or $\mathbf{V}_\infty = -\dot{\mathbf{R}}$. Then, the differential surface can be described by $dS = c(y)dy$, where $c(y)$ is the wing's chord dependent on location

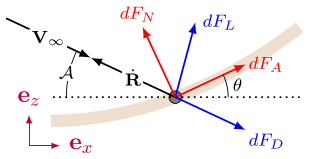


FIG. 2. Free-body diagram showing differential aerodynamic forces acting upon an individual blade element.

along the wing span y and dy is the blade element's width. We assume lift and drag coefficients of the form from[38] as follows:

$$C_P(\mathcal{A}) = C_P \sin(\mathcal{A})\cos(\mathcal{A}), \tag{17}$$

$$C_D(\mathcal{A}) = C_P \sin(\mathcal{A})^2 + C_{D,0}, \tag{18}$$

where C_P and $C_{D,0}$ are empirical aerodynamic coefficients. $C_{D,0}$ represents the drag the wing experiences at zero angle of attack. Since the wing is infinitely thin, this term effectively scales the total shear load acting over the wing's surface. The angle of attack $\mathcal{A}$ is defined as the angle between the wing's velocity vector and the x axis and is calculated via

$$\mathcal{A} = \tan^{-1}\left(\frac{\dot{\mathbf{R}} \cdot \mathbf{e}_z}{\dot{\mathbf{R}} \cdot \mathbf{e}_x}\right). \tag{19}$$

Drag acts collinear to the wing's velocity vector and lift acts orthogonal to drag. Differential lift and drag components dF_L and dF_D must be rotated by $\mathcal{A}$ to determine the differential aerodynamic forces acting normal to the deformed wing dF_N and axial to the deformed wing dF_A. This transformation is given by

$$dF_N = dF_D\cos(\mathcal{A}) + dF_L\sin(\mathcal{A}), \tag{20}$$

$$dF_A = -dF_D\cos(\mathcal{A}) + dF_L\sin(\mathcal{A}). \tag{21}$$

The normal and axial forces do not coincide with the wing's x–z coordinate basis (Fig. 2). To determine the aerodynamic forces acting in the x and z directions, the normal and axial forces must be rotated by the wing's local angle of rotation θ, where θ arises from wing deformation.

3. Quasi three dimensional unsteady vortex lattice method

The unsteady vortex lattice method (UVLM) is an established method, described in detail by Katz and Plotkin.[47] It is a potential flow method governed by

$$\nabla^2\boldsymbol{\Phi} = 0, \tag{22}$$

where $\boldsymbol{\Phi}$ is the velocity potential. As such, the fluid is considered incompressible throughout and irrotational except on the surface of the wing and in the wake. Viscous forces are ignored.

The wing is divided spanwise into multiple blades, each with a constant chord length. The aerodynamic loads on each blade are determined using a 2D UVLM solver. The blade is divided chordwise into panels. Each panel has a bound vortex attached at the quarter-chord and a control point at three-quarters-chord (Fig. 3).

08 July 2024 15:29:04

Published under an exclusive license by AIP Publishing

Physics of Fluids ARTICLE scitation.org/journal/phf

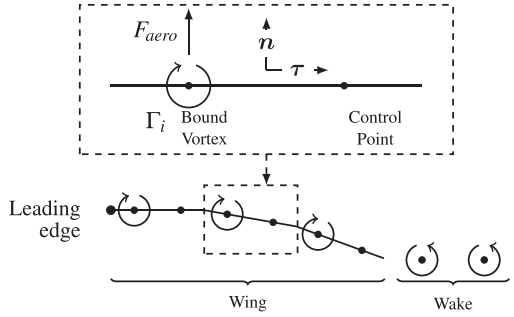


FIG. 3. Panel discretization used by the 2D UVLM solver.

Additionally, the trailing-edge panel sheds free wake vortices which are convected with the flow. Each vortex induces a tangential velocity field around it, described by the Biot–Savart law,

$$\boldsymbol{V}_{\text{ind}} = \frac{\Gamma_j}{2\pi}\frac{(r_{i,z} - r_{j,z})\mathbf{e}_x + (r_{j,x} - r_{i,x})\mathbf{e}_z}{|\boldsymbol{r_i}\text{-}\boldsymbol{r_j}|^2}, \tag{23}$$

where $\boldsymbol{V}_{\text{ind}}$ is the velocity at some point $\boldsymbol{r_i}$ induced by a vortex located at $\boldsymbol{r_j}$, and Γ_j is the vortex strength. This results in a singularity; as r gets smaller, the induced velocity becomes unreasonably large. To remedy this, a cutoff radius r_{co} is defined so that within this radius, the induced velocity decreases linearly as separation decreases, and the induced velocity function becomes

$$\begin{aligned} \boldsymbol{V}_{\text{ind}} &= \frac{\Gamma_j}{2\pi}\frac{(r_{i,z} - r_{j,z})\mathbf{e}_x + (r_{j,x} - r_{i,x})\mathbf{e}_z}{|\boldsymbol{r_i}\text{-}\boldsymbol{r_j}|^2}; \quad |\boldsymbol{r_i}\text{-}\boldsymbol{r_j}| > r_{co}, \\ \boldsymbol{V}_{\text{ind}} &= \frac{\Gamma_j}{2\pi}\frac{(r_{i,z} - r_{j,z})\mathbf{e}_x + (r_{j,x} - r_{i,x})\mathbf{e}_z}{r_{co}^2}; \quad |\boldsymbol{r_i}\text{-}\boldsymbol{r_j}| \le r_{co}. \end{aligned} \tag{24}$$

At each time step, the strengths of the bound vortices on the wing as well as the newly shed wake vortex are found by enforcing the non-penetration condition; the wing is a solid barrier through which the fluid is unable to flow. This means the fluid can only move across the surface, and the velocity component normal to the wing surface is zero, stipulated by

$$\boldsymbol{V} \cdot \mathbf{n} = 0, \tag{25}$$

where $\boldsymbol{n}$ is the surface-normal vector on the wing and the flow velocity $\boldsymbol{V}$ is in a wing-fixed frame of reference. When this condition is enforced at the control point of each wing panel, this takes the form

$$\begin{bmatrix} a_{1,1} & a_{1,2} & \cdots & a_{1,N_p} & a_{1,N_p+1} \\ a_{2,1} & a_{2,2} & \cdots & a_{2,N_p} & a_{2,N_p+1} \\ \vdots & \vdots & \ddots & \vdots & \vdots \\ a_{N_p,1} & a_{N_p,2} & \cdots & a_{N_p,N_p} & a_{N_p,N_p+1} \\ 1 & 1 & \cdots & 1 & 1 \end{bmatrix} \begin{Bmatrix} \Gamma_1 \\ \Gamma_2 \\ \vdots \\ \Gamma_{N_p} \\ \Gamma_{W_1} \end{Bmatrix} = \begin{Bmatrix} rhs_1 \\ rhs_2 \\ \vdots \\ rhs_{N_p} \\ rhs* \end{Bmatrix}, \tag{26}$$

where aerodynamic influence coefficient $a_{i,j}$ is the surface-normal velocity induced at the control point of panel i by a unit strength vortex on panel j. rhs_i is the total surface-normal velocity at the ith control point due to all other sources—rigid body kinematics, wing deformation, and wake vortices, and rhs^* is the total bound vorticity on the wing. $\Gamma_{1\ldots N_p}$ is the bound vortex strength of the corresponding panel and Γ_{W_1} is the strength of the newly shed wake vortex, equal to the change in total bound vorticity over the wing from the previous time step. The free wake vortices are massless, and follow the local flow velocity induced by the wing bound vortices and other wake vortices as determined from Eq. (23). The pressure jump at the ith panel is found using the unsteady Bernoulli equation[47]

$$\Delta P_i = -\rho_f \left[(-\dot{\boldsymbol{R}}_{\boldsymbol{i}} + \boldsymbol{V}_{ind,i}) \cdot \boldsymbol{\tau}_i \frac{\Gamma_i}{ds} + \frac{\partial}{\partial t}\sum_{j=1}^{i} \Gamma_j \right], \tag{27}$$

where ΔP_i is the pressure jump across the ith panel, $\dot{\boldsymbol{R}}_{\boldsymbol{i}}$ is the velocity of the panel ith in the inertial reference frame arising from the rigid body kinematics and the wing deformation, $\boldsymbol{V}_{ind,i}$ is the velocity induced by the ith bound and wake vortices, $\boldsymbol{\tau}$ is the panel surface-tangent vector, and ds is the panel length. The first term on the right-hand side describes the pressure resulting from quasi-steady aerodynamic forces such as lift and drag. The second term accounts for the pressure due to added mass, where the summation is from the leading edge to the ith panel. The aerodynamic force on each panel acts normal to the surface, and the total force on each blade is obtained by summing the x and z components of the panel forces.

C. High-fidelity computational model

Computational fluid dynamics (CFD) is a common approach to solving the Navier–Stokes equations across a discretized domain. These equations are derived from continuum mechanics and serve to maintain conservation of mass and momentum, and are accepted in the engineering community to encompass most physics pertinent to modeling a fluid domain. Finite element analysis (FEA) is a method for modeling the deformations and stresses throughout structures across a wide range of geometry, material properties, and composite assemblies. To build a two-way coupled model to use as a validation tool for the ROMs, we interface a CFD model using Siemens' Star-CCM+ (v15.04.008) to an FEA model using Dassault Systèmes Abaqus 2019 (6.19-1). Communication between the two commercial packages is handled through SIMULIA Co-simulation Engine (CSE).

For a reduction in computational expense, the CFD model uses a Spalart–Allmaras (SA) closure model in a Reynolds-averaged Navier–Stokes (RANS) scheme. RANS models are used throughout turbulent flow research, and the SA was chosen for its efficiency as a one-equation model as well as its previous use in studying flapping wing aerodynamics.[48,49] This modeling technique was used to calculate the pressure across the wing's surface as influenced by the entire flow field. To resolve this flow field accurately without remeshing the entire fluid domain at each time step, we used a Chimera mesh approach to keep a consistent discretization around the rotating wing.[50] This allows for a finely discretized region surrounding the wing (the *overset* mesh) to move with prescribed kinematics while the surround fluid domain discretization (the *background* mesh) remains motionless (Fig. 4). At each time step, the overset mesh region is cut from the background mesh, and overlapping cells along the edges of the overset region are used to interpolate data between the two meshes,

08 July 2024 15:29:04

Published under an exclusive license by AIP Publishing

Physics of Fluids ARTICLE scitation.org/journal/phf

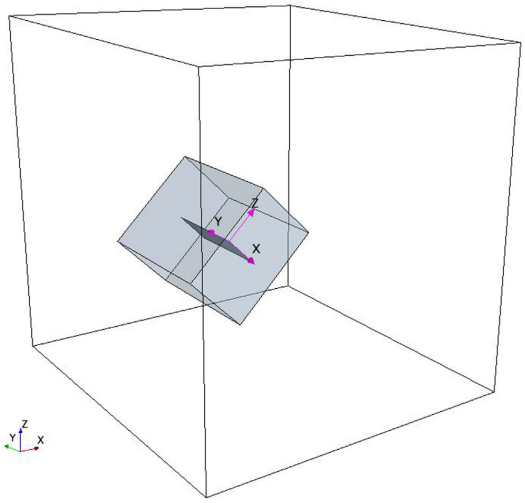


FIG. 4. Background mesh (outlined) and overset mesh (light gray) of the fluid domain in Star-CCM+. The rectangular wing is seen in the dark gray within the overset mesh. The wing-fixed coordinate system is shown in pink, with an origin at the wing root's leading edge. The background mesh must be large enough to accommodate flapping kinematics and encompass pertinant flow features, while the overset mesh must accommodate the out-of-plane deformation of the wing.

thereby maintaining the conservation of mass and momentum. A radial basis function (RBF) mesh morphing algorithm is also applied to the overset mesh, allowing these cells and the overset region boundary to stretch and compress to accommodate the deformation of the wing as calculated in FEA.

The deformations calculated in FEA are influenced by the centrifugal and Euler forces associated with flapping motions as well as the aerodynamic forces calculated by CFD at every time step. We applied the flapping kinematics by imposing angular velocity-dependent boundary conditions at the wing's fixed point of rotation. Abaqus' implicit solver was then used to resolve deformations, which were in turn sent back to CFD.

The communication between FEA and CFD facilitated by SIMULIA CSE allowed us to capture aeroelastic interactions through bilateral coupling, as data are transferred between both software at every time step specified in CFD (Fig. 5). After CFD initializes the motionless fluid domain, kinematics are applied in FEA, and deformations due to inertial and centrifugal forces are resolved. Abaqus uses a dynamic time step to allow for a converged structural solution at each time step, but when the time step specified in CFD has been reached, the new wing geometry is sent to Star-CCM+ CFD in the inertial and wing-fixed frames. This change in geometry is then interpreted as movement of the wing boundary in CFD caused by both the rotation and deformation. Next, the overset mesh region is rotated by the flapping kinematics, and then is morphed based on the wing deformations. Finally, the entire fluid domain in CFD is resolved, and the resulting distribution of aerodynamic forces is sent back to Abaqus FEA. In FEA, the process continues, now adding the aerodynamic forces into the calculation of wing deformation. This cycle continues until a user-specified solution time is reached.

The HiFi model makes minimal assumptions about insignificant physics parameters aside from those associated with the influence of turbulence on the fluid domain as modeled with the SA RANS model. This allows the HiFi model to capture some of the physics that the ROMs ignore, such as spanwise flow which is clearly resolved by the three-dimensional application of the Navier–Stokes equations, and the influence of added mass which is captured through the acceleration term of the conservation of momentum.

III. NUMERICAL SIMULATION PARAMETERS

We now establish the simulation parameters necessary to implement and compare the HiFi model and ROMs. We investigate a thin, homogeneous rectangular wing with flapping kinematics idealized from those of a flying insect. We consider three modulus values (flexible, medium, and stiff hereafter) to explore the influence of flexibility on deflection and aerodynamic forces/moments. The wing is assumed to have a rigid leading edge. All rotations are assumed harmonic.

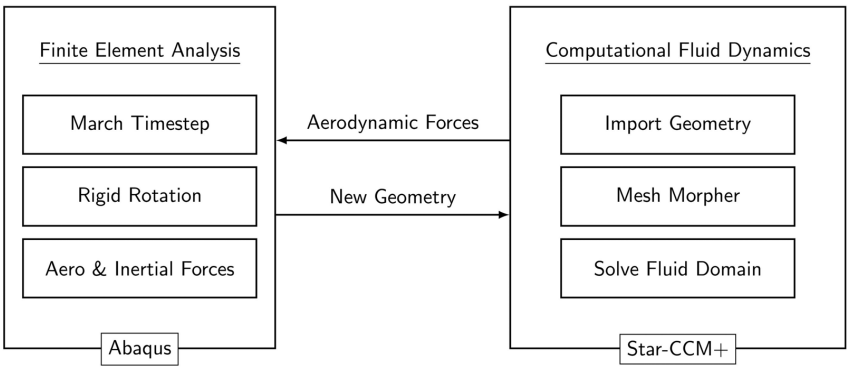


FIG. 5. Bilaterally coupled workflow between Abaqus FEA and Star-CCM+ CFD. This cycle continues at every time step described by CFD.

08 July 2024 15:29:04

Published under an exclusive license by AIP Publishing

Physics of Fluids ARTICLE scitation.org/journal/phf

TABLE I. Wing parameters.

Variable	Description	Value	Unit
L	Wing span	5	cm
c	Wing chord	2	cm
t	Wing thickness	0.17	mm
α_0	Roll amplitude	60	°
β_0	Pitch amplitude	45	°
γ_0	Yaw amplitude	0	°
⋯	Pitch phase	90	°
f	Flap frequency	10	Hz
ρ	Material density	235.5	kg m^{-3}
E	Elastic modulus	(Flexible) 7.3×10^7	Pa
		(Normal) 1.365×10^8	Pa
		(Stiff) 2.4×10^8	Pa
Re	Reynold's number	4400	⋯

The wing flaps about a stationary point in a quiescent environment, which is most representative of hovering flight. Wing parameters are summarized in Table I, and the geometry is shown in Fig. 6. Wing morphology and flapping kinematics are based roughly on the forewing of the monarch butterfly.[51]

The structural model used in DBET and UVLM ROMs [Eq. (9)] is fully defined by flapping kinematics, wing mode shapes ϕ_k, natural frequencies ω_k, damping ratios ζ_k, and the non-conservative load Q_k. We use a numerical modal analysis implemented via Abaqus to calculate ϕ_k and ω_k. The finite element model used for modal analysis is identical to that used for dynamic simulation in the HiFi model, with the primary difference residing in the solution procedure (finite element details are discussed with HiFi model parameters). Practically, we retain two vibration modes (Fig. 6) for the structural solver, which have natural frequencies ($\omega_1 = 40$ Hz, $\omega_2 = 52.2$ Hz) for the flexible wing, ($\omega_1 = 55$ Hz, $\omega_2 = 74.6$ Hz) for the medium wing and ($\omega_1 = 73$ Hz, $\omega_2 = 99$ Hz) for the stiff wing. Damping ratio ζ_k is set to 5% for both vibration modes. The structural model is solved using MATLAB (V2021b) "ode45" at time steps dictated by the DBET and UVLM ROMs.

Simulation parameters for the DBET and UVLM models are summarized in Table II. The DBET model requires empirical aerodynamic coefficients and reference locations for the angle of attack and where aerodynamic forces are assumed to act. We use aerodynamic coefficients in proximity to the values used in Ref. 38. The angle of attack is referenced from the three quarter chord and aerodynamic forces act at the quarter chord. The wing must be broken into ten blade elements for maximum wing deformation and mean force in the $-X$ direction (opposite of gravity, Fig. 1) to converge. The UVLM model requires the wing to be discretized into blades and both the wing and wake must be discretized into bound and shed vortices. The values for panel count, wake count and time step were determined based on convergence studies for a previous 2D model.[52] On each panel, the bound vortex is placed one quarter chord back from the leading edge and the control point is at three quarter chords from the leading edge. The cutoff radius is selected such that results largely match those found without a cutoff, except that large transient spikes should be reduced. Both models are coded in MATLAB (V2021b).

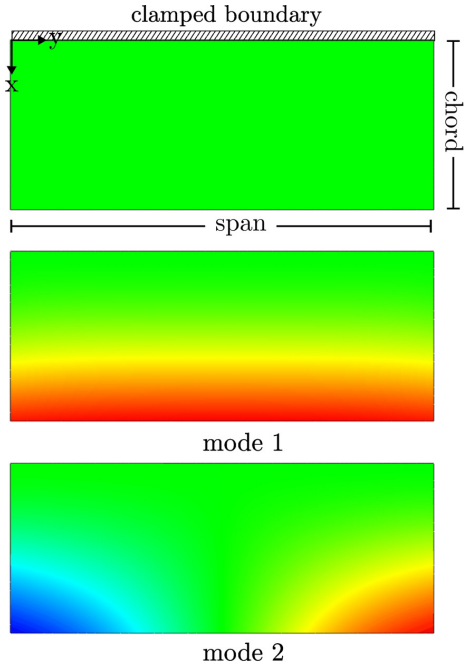


FIG. 6. Geometry and vibration modes of the rectangular wing used in numerical simulation. The first mode represents a chordwise-bending mode, and the second represents a chord-wise torsional mode. Red indicates positive out-of-plane motion, green indicates no motion and black indicates negative out-of-plane motion. Mode shapes are arbitrary in magnitude, which is why a colorbar is omitted.

Parameters for the HiFi model are summarized in Table III. The CFD domain size was chosen with sufficient distance behind the wing's trailing edge and away from the wing's tip to capture flow structures releasing from the wing that could affect the transient fluid forces acting on the wing. The overset mesh size was chosen to capture the

TABLE II. DBET and UVLM simulation parameters.

Variable	Description	Value	Unit
DBET			
C_P	Pressure coefficient	2.9	⋯
$C_{D,0}$	Drag offset coefficient	0.1	⋯
N_s	Number of blades	10	⋯
N_t	Steps-per-wingbeat	100	⋯
UVLM			
N_s	Number of blades	20	⋯
N_p	Number of panels-per-blade	20	⋯
N_w	Number of wake vortices	100	⋯
N_t	Steps-per-wingbeat	200	⋯
r_{co}	Cutoff radius	0.25c	cm

08 July 2024 15:29:04

Published under an exclusive license by AIP Publishing

Physics of Fluids ARTICLE scitation.org/journal/phf

TABLE III. High-fidelity modeling parameters.

Variable	Description	Value	Unit
Computational fluid dynamics			
μ	Dynamic viscosity of air	1.86×10^{-5}	Pa s
ρ	Density of air	1.18	kg m^{-3}
...	Domain dimensions	$0.19 \times 0.21 \times 0.2$	m
...	Overset dimensions	$0.04 \times 0.08 \times 0.06$	M
...	Mean element length (domain)	1.2	mm
...	Mean element length (overset)	0.6	mm
...	Total number of elements	3 319 937	...
...	Prism layers	5	...
...	Prism layer growth rate	1.5	...
Δt	Timestep	0.001	s
Finite element analysis			
...	Element type	S4R	...
α	Raleigh damping factor	(Flexible) 14.472	...
		(Normal) 19.858	...
		(Stiff) 26.344	...
...	Number of nodes	1071	...
...	Shell thickness	0.17	mm
...	Number of shell element integration points	5	...
Δt_{min}	Minimum automatic timestep	1×10^{-6}	s
Δt_{max}	Maximum automatic timestep	0.001	s

flow structures immediately surrounding the wing with higher resolution and to allow for large wing deformations without over-compression or elongation of any elements by the mesh morpher. An earlier study involving single degree of freedom flapping of a rigid wing with identical geometry revealed converged results with 1.2-mm-sized elements in the domain region and 0.6-mm elements in the overset region.[53] Within the same study, we determined an adequate time step for solution convergence was 0.001 s. At each time step, 25 inner iterations were used to resolve the Navier–Stokes equations, based on convergence of the model residuals. These meshing and time-stepping studies were performed with a rigid wing, so mesh refinement was increased modestly to account for the additional motion of the wing's deflection.

The finite element structural model was comprised of 1000 four-node quadrilateral (S4R) shell elements (1071 nodes), which was sufficient for the wing's first two natural frequencies to converge. We used an automated dynamic time step within FEA, where the minimum time step used was 1×10^{-6} s and the maximum time step was 0.001 s when deformation data were saved and passed to Star-CCM+ CFD. The wing was modeled with a rigid leading edge by applying kinematic constraints to all nodes along this edge to a control point at the wing's point of rotation *O*. At *O*, angular velocity boundary conditions were applied to prescribe the flapping kinematics which the entire leading edge rigidly followed. We use a Rayleigh damping model and select Rayleigh damping factor α such that the first two vibration modes have a damping ratio of 5%, consistent with the ROMs.

IV. RESULTS

Across all models and wing stiffness values considered, we compared wing deformation, aerodynamic forces in the inertial and wing-fixed reference frames, and total moments in the wing reference frame. Wing deformation was compared on the trailing edge at the wing root and wing tip (Fig. 7). In general, the agreement between all models is acceptable. In the most flexible case, the wingtip deflected about 5–5.5 mm, or 25% of the chord length. Maximum deflections predicted by each model are similar, with the ULVM over-predicting the peak value by about 10% compared to the HiFi model. Since both DBET and UVLM ROMs rely on the same structural solver, the difference in response amplitude must stem from differences in fluid loading. The UVLM induces greater deflection, possibly due to an added mass force that is absent from the DBET model. ROM error decreases as the wing becomes stiffer and deformations are reduced. All models indicated that the wing root experienced lower deflections than wing tip (maximally 3.5–4 mm), likely because of increased aerodynamic loading near the wingtip. Aerodynamic loads generally increase along the span (unless in close proximity to the wingtip, where pressure losses occur) due to increasing velocity. The difference in deformation between wingroot and wingtip indicates at least two vibration modes (Fig. 6) are excited during flapping. If deformation was dominated by the first mode, wing deformation would vary only from leading edge to trailing edge and would be nearly uniform from root to tip. At both wingtip and root, deformation occurred at the primary flapping frequency with lower harmonics at three times the flapping frequency superimposed on the response. The primary response from the HiFi model leads that of UVLM, which in turn leads the DBET model. The deformation time lag observed in the ROMs stems from a lag in aerodynamic loading relative to the HiFi model.

To better compare full-field deformation, we generated a contour plot of wing deformation at 1/8 intervals of a single wingbeat. Figure 8

08 July 2024 15:29:04

Published under an exclusive license by AIP Publishing

Physics of Fluids ARTICLE scitation.org/journal/phf

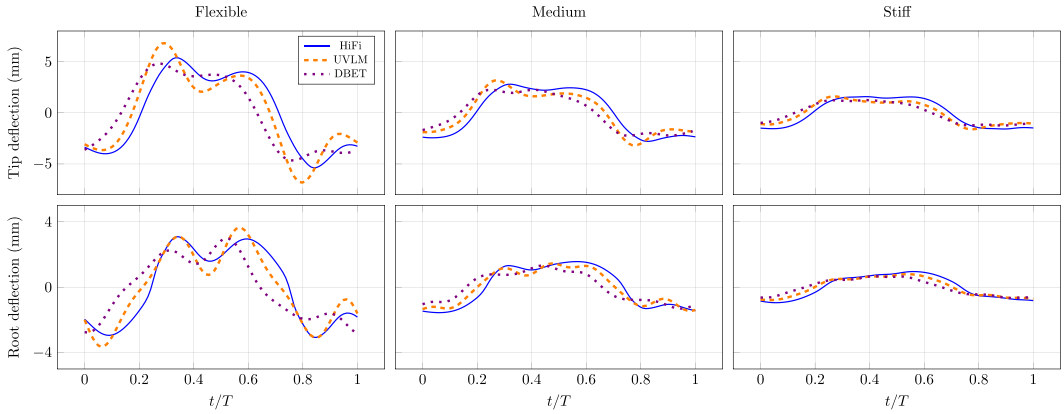


FIG. 7. Deflection of the wing's trailing edge at tip and root locations along the wing's span.

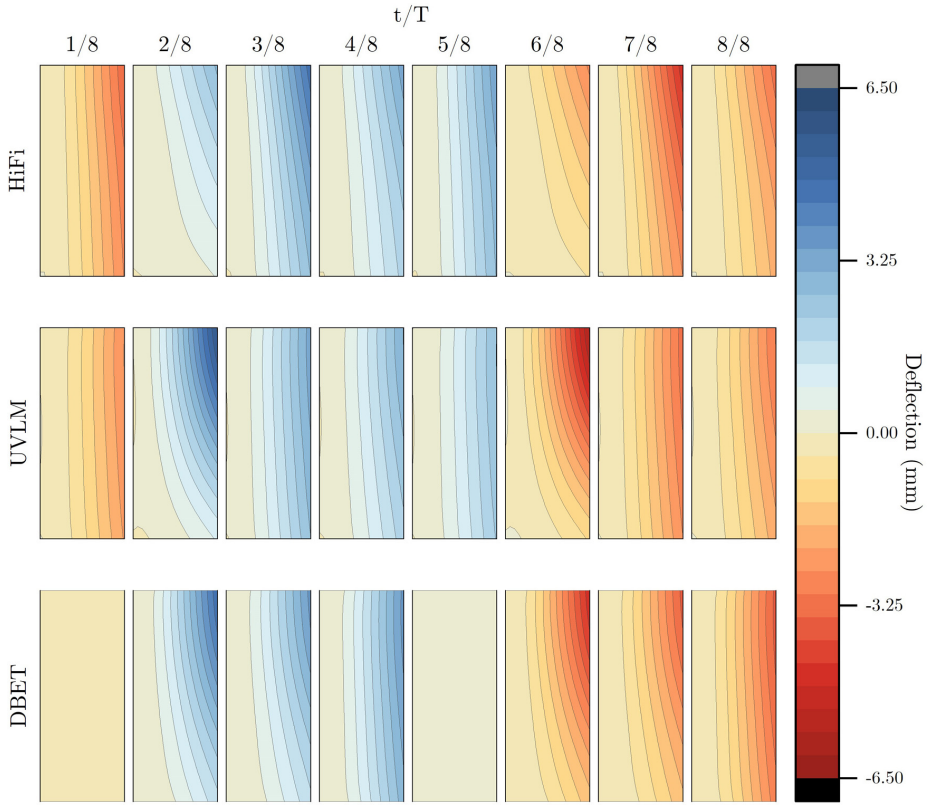


FIG. 8. Contour map showing out-of-plane deformation of the flexible wing as a function of wingbeat period *T*.

08 July 2024 15:29:04

Published under an exclusive license by AIP Publishing

Physics of Fluids ARTICLE scitation.org/journal/phf

shows the out-of-plane deflection predicted by each model for the flexible wing, which is the worst-case scenario in terms of model agreement since the ROMs more closely agree with the HiFi model at smaller deflections (Fig. 7). At most intervals, the deflection contour matches fairly well. Noticeably, DBET indicates near zero deflection at $T/8$ and $5T/8$, whereas the UVLM and HiFI models show non-zero contour profiles. This discrepancy occurs due to the time-lag between DBET and HiFI deflections. Those instances aside, these results suggest that the structural model employed by the ROMs captures deformation profiles reasonably well with only two vibration modes retained, at least for this wing design. As discussed previously, the largest deformation occurs near the wing tip while the root experienced lower deformation by comparison.

Aerodynamic forces with respect to the wing fixed reference frame are shown in Fig. 9. For all wing stiffnesses, the predominate forces act in the wing z direction. For the most flexible case, the absolute peak forces predicted via the HiFi model are about 4, 1, and 0.2 mN in the wing z, x, and y directions, respectively. F_z agrees well across all models. UVLM and CFD produce nearly identical results, while DBET indicates a slight phase lag and lower amplitude in F_z. All models show that F_z increases with wing stiffness, likely because the wing's normal vectors remain more closely aligned with z at lower deflections. The agreement between ROMs and HiFi models is not as strong within the wing-fixed x direction, due in part to differences in how shear is accounted for. The UVLM entirely lacks shear loads, leading to it underestimate F_x compared to CFD and DBET for stiffer wings. The difference is primarily in force amplitude, as the general waveforms agree reasonably well. The agreement is better for more flexible wings, where a larger percentage of F_x stems from pressure loading. DBET produces similar F_x from mid-stroke to stroke reversal ($t/T = 0$ to $t/T = 0.25$) for all wing stiffnesses, but force profile then diverges until next mid-stroke at $t/T = 0.5$. All three models predict a reduction in F_x as the wing is made stiffer, which is opposite to the trend observed in F_z. This is because at larger deflections, the wing's normal vectors have a larger component in the wing's x direction. Due to the lack of spanwise flow, neither DBET nor UVLM are well-positioned to estimate F_y; they are therefore omitted from Fig. 9. Nonetheless, the HiFi model shows the forces in y are considerably lower than the other two force components, and thus we believe it is reasonable to neglect them in ROM efforts.

We next look at total moments at point of rotation O in the wing fixed frame, where the total moments are the inertial moments less the aerodynamic moments (Fig. 10). M_x generally agrees across all three models and at each level of flexibility, though there is a phase discrepancy which may introduce error when calculating quantities from moments such as mechanical power. Moments M_y and M_z also agree well in magnitude across the models, but the phase lag of UVLM and DBET predictions with respect to HiFI predictions is more pronounced. The largest error occurs in M_z of the stiffest wing, which is influenced by the wing's F_x and F_y forces. This error likely occurs because neither DBET and UVLM models are capable of resolving F_y, and the UVLM model does not account for shear, thus leading to poor predictions of F_x for stiff wings (Fig. 9). Nonetheless, because the total moments are in large part driven by inertia, minor discrepancies between aerodynamic moments are not manifested as large discrepancies in the total moments.

We now compare aerodynamic forces with respect to the inertial frame, which is of practical importance because a flapping wing insect must produce sufficient lift to stay aloft during hover. Aerodynamic forces in the inertial frame generally shows close agreement between models (Fig. 11). The HiFi model and ROMs estimate lift forces F_X (recall that gravity is aligned in the $+X$ direction, Fig. 1) that are

08 July 2024 15:29:04

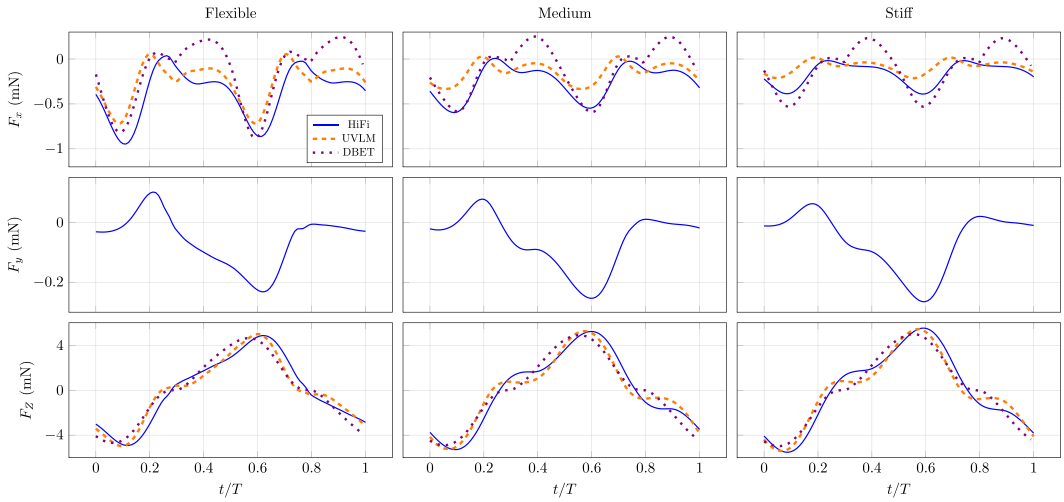


FIG. 9. Aerodynamic forces predicted by each model with respect to the wing-fixed reference frame. UVLM and DBET models do not resolve spanwise flow, so no F_y component is shown for these models.

Published under an exclusive license by AIP Publishing

Physics of Fluids ARTICLE scitation.org/journal/phf

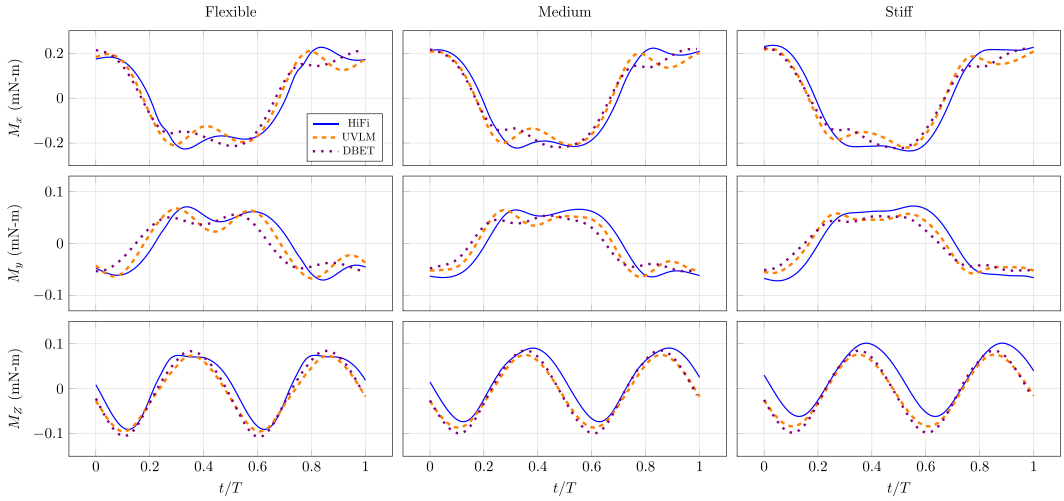


FIG. 10. Aerodynamic moments predicted by each model with respect to the wing-fixed reference frame.

similar in timing and magnitude for each wing stiffness considered. The largest difference in F_X between ROMs and the HiFi model occurs near $t/T = 0.3$, shortly after stroke reversal. This is during the portion of the wing beat when the highest acceleration and wing deflection occur, so this dissimilarity may relate to the differences in how the added mass force is calculated (or in the case of DBET, the lack of added mass). None of the models indicate an increase in lift with wing flexibility; in fact, the more flexible wing produces less lift relative to the stiff wing, though possibly with less input power (see Sec. IV A). The inertial-frame force F_Z is the largest force component in magnitude and agrees well across each model. Similar to wing fixed F_z, world frame F_Z increases with wing stiffness as well. Model agreement is somewhat worse for F_Y, again because neither of the ROMs can accommodate spanwise forces within the wing-fixed frame.

08 July 2024 15:29:04

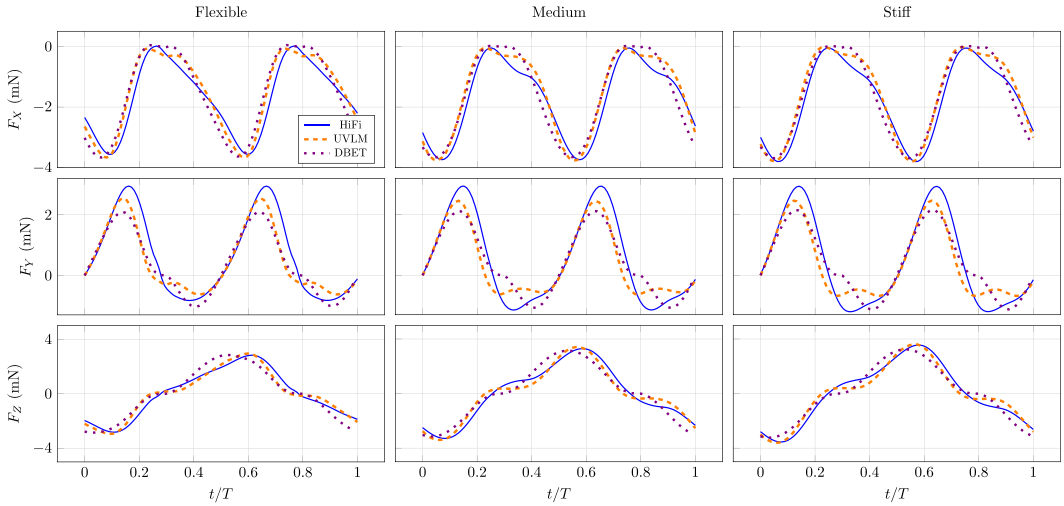


FIG. 11. Aerodynamic forces predicted by each model with respect to the inertial reference frame. Gravity acts in the $+X$ direction.

Published under an exclusive license by AIP Publishing

Physics of Fluids ARTICLE scitation.org/journal/phf

A. Parametric study

Finally, we perform a parametric study to demonstrate the computational efficiency of the ROMs in exploring wide parameter spaces. We aim to determine how wing stiffness (characterized by the wing's first natural frequency) and mass affect peak deflection, mean lift, and average power at steady state. The average power $\bar{P}$ is calculated via

$$\bar{P} = \frac{1}{T}\int_0^T \mathbf{M}_{total} \cdot \mathbf{\Omega}\, dt, \tag{28}$$

where the total moments are defined by $M_{total} = \mathbf{M}_0 - \mathbf{M}_{aero}$. This expression for power assumes that negative power offsets positive power, or that potential energy is stored in the system and is later recycled to do work. The first natural frequency of the wing was swept from 30 to 100 Hz in 0.1 Hz increments, and we considered discrete wing masses of 40, 60, and 80 mg. Due to the limiting computation time of the high-fidelity model, only the three wing stiffness discussed previously were used in this study. The results are shown in Fig. 12.

As the wing's natural frequency increases, the deflection tends toward zero at a similar rate for all models. The closest agreement was for the 80 mg wing, where the inertial forces dominate the deflection more so than in the lighter wings. In this case, the CFD and DBET line up well at all points, and the UVLM shows only slightly higher wing deformation. As the wing mass increases, the wing deflections predicted by DBET and UVLM diverge, indicating that the differences in the fluid models are responsible for variability in deflection.

The mean lift estimated by CFD is roughly 10% higher than that of the reduced-order models. However, all models show the same general trend, where the wing produces more lift as it becomes more rigid. The lower lift estimated by UVLM may result from the lack of LEV, a feature which is believed to contribute significantly to force production in flapping wings.[54] The lower lift estimated by DBET stems from the aerodynamic coefficient C_P, which may be inflated to increase the lift curve. Wing mass did not have a considerable effect on mean lift.

UVLM and DBET produce nearly the same mean lift ($-F_X$) from the stiffest case all the way down to moderate levels of flexibility. At higher wing masses, the similarity persists for lower natural frequencies. As the natural frequency is reduced toward 30 Hz (three times the flapping frequency), the DBET and UVLM begin to diverge. However, at this level of compliance, the wing deformation is about 75% of the chord length, and the linear structural framework is likely unsatisfactory. Aerodynamic forces in this range should be interpreted with caution.

The last quantity examined is power consumption. All three methods show that more flexible wings require less power than stiffer wings, and that more massive wings require more power than lighter wings. UVLM and HiFi models show that power steadily decreases with natural frequency. DBET predicts less of a dependence on wing stiffness, though it does still decrease with natural frequency. CFD shows a much steeper relation between stiffness and power than either of the ROMs, perhaps because of shear that is unmodeled by the UVLM model and underestimated by the DBET model. Errors in power are also sensitive to the relative phase between total moments and angular velocity, the latter which is identical across all models. Thus, small errors in total moment phase (Fig. 10) may cause larger

08 July 2024 15:29:04

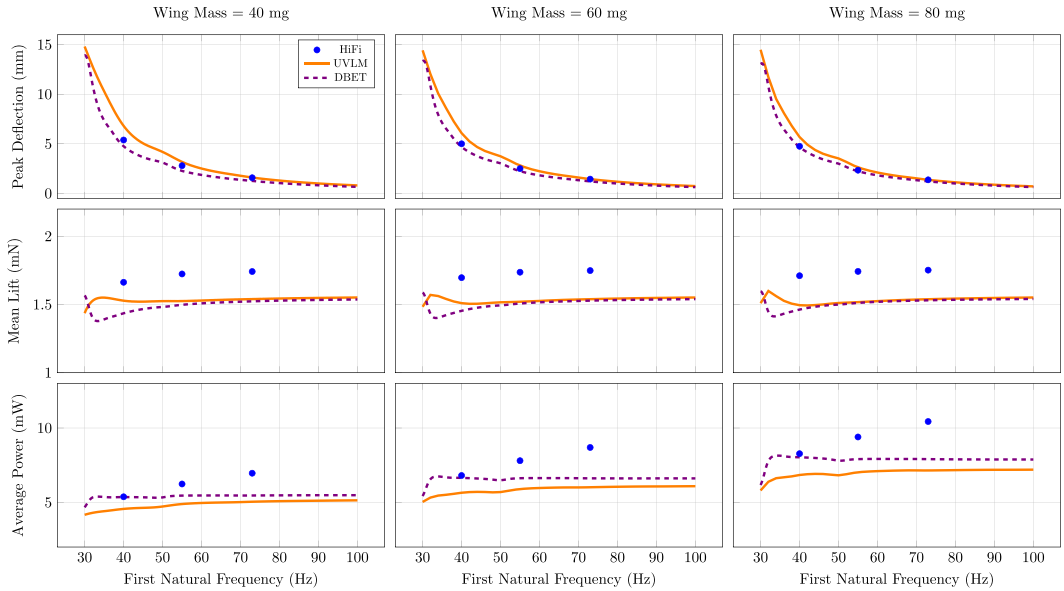


FIG. 12. Parameter study showing the effect of wing flexibility (parametrized by the wing's first natural frequency) and mass on peak deflection, mean lift, and average power. The corresponding time-series data for lift and deflection is shown for the 60 mg wing at natural frequencies of 40, 55, and 73 Hz in Figs. 7 and 11.

Published under an exclusive license by AIP Publishing

Physics of Fluids ARTICLE scitation.org/journal/phf

errors in power. Still, these studies support the idea that moderate wing flexibility can increase aerodynamic performance, and that the reduction in power consumption outweighs the reduction in lift.

V. DISCUSSION

Wing flexibility and deformation are essential to sensory function and aerodynamic performance in flapping wing insect flight. However, the high-order models used to evaluate flapping wing FSI usually require considerable computational resources, rendering them impractical for parameter studies that consider variable wing stiffness, morphology, or flapping kinematics. In this work, we present two quasi-3D ROMs capable of estimating wing deformation and the resulting aerodynamic forces and moments. Both ROMs rely on a modal truncation-based structural framework but differ in their fluid models. The first ROM uses an algebraic DBET fluid model, and the second ROM uses a UVLM approach. We applied the models to estimate the dynamics of a thin, flexible, rectangular plate with a rigid leading edge subject to rotational kinematics modeled after insect flapping. We compared wing deformation, aerodynamic forces, and total moments predicted by the ROMs to those determined by more conventional HiFi modeling. Both ROMs predicted wing deformation with good accuracy, even when deflections were as large as 25% of the chord length. The ROMs resolved predominate aerodynamic forcing in wing-fixed and inertial reference frames fairly well, but were less accurate in resolving the smaller forces acting in the wing's x–y plane. We then performed a parametric study to demonstrate the influence of wing mass and stiffness on wing deflection, average lift, and average power. The ROMs predicted peak deflection and mean lift fairly well, but had larger discrepancies in average power for stiffer wings. In the following, we discuss the relevance of these ROMs within the study of flapping wing FSI.

A. Computational efficiency

Overall, the computational savings conferred by the two ROMs render them useful tools for studies that require exploration of broad parameter spaces. Direct computational modeling is computationally intensive—within CFD, resolving only the conservation of mass, conservation of momentum, and closure model equations for 25 iterations on each element yields nearly 250×10^6 equations to solve at every time step. Within FEA, the wing is treated as geometrically nonlinear and consequently each time step of analysis must be broken into smaller increments such that a particular solution path may be followed. Considering each node of an S4R element has six degrees-of-freedom, and the plate model has 1071 nodes, about 6×10^3 equations must be solved at each increment within the FEA solver. Thus, computational expense is the biggest motivator for reduced order modeling.

The ROMs were determined to be much faster at modeling bulk propulsive forces and wing deformation relative to the high-fidelity modeling approach. All simulations were performed on a desktop computer custom built for this HiFi setup. We used 10 threads of an intel i9–9900K processor operating with a 4.7 GHz clockspeed, with 64 GB of available DDR4 RAM. When comparing solution times for the flexible wing, the HiFi model resolves the aerodynamic forces and wing deformation in about 5.4 h per wingbeat, the UVLM model about 2.5 s per wingbeat, and the DBET model about 0.093 s per wingbeat. This results in 4 and 6 orders of magnitude in time savings for UVLM and DBET, respectively, demonstrating that ROMs hold value anytime that computational efficiency in needed. We show a practical parameter study where 2100 mass/flexibility combinations were simulated by the ROMs (Fig. 12), taking 7.3 h of computation time for UVLM and 16.3 min for DBET. To gather the same data using the HiFi model would have taken approximately 6.5 years.

B. Applications of ROMs

ROMs play an important role in the study of insect flight. Across species, insect wings have distinct morphological features and flapping kinematics that influence wing strain profiles, sensing and aerodynamic performance. The effect of morphology and flapping kinematics is difficult to fully address using HiFi models. Though ROMs have lower accuracy relative to direct computational approaches, they allow parameter spaces to be explored more effectively. HiFi modeling can then be used for a subset of conditions to ensure ROM accuracy.

Both of the ROMs presented in this work are general in the sense that they can accommodate arbitrary wing geometry, morphology and flapping kinematics. As discussed in Sec. II B 1, the reduced-order structural model is versatile because it can interface with modal-based finite element solvers. The ability to pre-compute mode shapes in FEA allows the user significant freedom and creativity in the geometry and structural domain to investigate the effects of a wide range of biological or engineering-inspired wing designs. Further, physical experimentation like scanning laser vibrometry could be used to compute mode shapes of biological wings,[40] allowing for deeper study of real insect wings. Any number of mode shapes can be included in the models when deemed appropriate. Practically, the number of modes retained generally corresponds to the modes with natural frequencies that fall within ten times that of the predominant excitation frequency.

C. ROM limitations

Despite the advantage of the flapping wing FSI ROMs, each has limitations that constrain their accuracy in some contexts. First, both the quasi-3D DBET and UVLM ROMs neglect spanwise flow. Spanwise flow is a critical for modeling effects like shed vortices from the wingtip that result in downwash and induced drag.[55] Without spanwise flow, it is not possible for fluid to wrap around the wingtip in any way. Quasi-3D approaches will consequently overestimate the fluid loading near the wingtip of a structure, which may in turn amplify the deformation of modes with large displacements near the wingtip. If the rigid leading edge assumption employed in this work were relaxed, this modeling error may result in a larger discrepancy between deformations estimated via ROMs and HiFi methods.

Second, both ROMs have limited capacity to describe chordwise pressure distributions. The DBET model provides no force distribution information and instead assumes all aerodynamic forces simply act at the quarter chord. The UVLM model provides some information regarding chordwise pressure variation, but has limited accuracy near the leading edge because the LEV is not explicitly modeled. The LEV is considered a major factor in lift generation.[54] The UVLM method assumes that flow is always attached to the wing until wake vortices are shed from the trailing edge. This means that wing motions at angles of attack that would normally induce stall without the LEV are modeled such that flow remains attached over the leading edge, thereby requiring particularly strong V_{ind} used in pressure calculations.

08 July 2024 15:29:04

Published under an exclusive license by AIP Publishing

Physics of Fluids ARTICLE scitation.org/journal/phf

Consequently, we believe the LEV must be considered to improve chordwise pressure estimates.

Third, both ROMs provide limited or no information regarding the flow field surrounding the wing. The DBET model provides only bulk propulsive forces and moments. UVLM cannot resolve the entire fluid domain and, instead, is only tracking some flow features that are shed from the wing. These features are monitored for a user specified amount of time, which could be a cause of error in instances where flow features have a delayed interaction with the wing. This is potentially problematic when fluid flow causes a more spatially varying distribution of aerodynamic force.

These modeling limitations help define the scope and appropriate use these quasi-3D ROMs. While studies sensitive to changes in spanwise flow or spatial distribution of forces should perhaps be left to other methods, studies involving bulk aerodynamics and high computational efficiency benefit significantly. The 4 and 6 orders of magnitude time savings is a clear demonstration of why these models can be advantageous over conventional high-fidelity approaches in parameter studies.

ACKNOWLEDGMENTS

This research was supported the National Science Foundation under Award No. CBET-1855383 to M.J. Any opinions, findings, and conclusions or recommendations expressed in this material are those of the author(s) and do not necessarily reflect the views of the National Science Foundation.

AUTHOR DECLARATIONS

Conflict of Interest

The authors have no conflicts to disclose.

Author Contributions

R. Schwab and J. Reade contributed equally to this work.

Ryan Schwab: Formal analysis (equal); Investigation (equal); Methodology (equal); Software (equal); Validation (equal); Writing – original draft (equal); Writing – review & editing (equal). **Joseph Reade:** Formal analysis (equal); Investigation (equal); Methodology (equal); Software (equal); Validation (equal); Visualization (equal); Writing – original draft (equal); Writing – review & editing (equal). **Mark Jankauski:** Conceptualization (lead); Formal analysis (supporting); Funding acquisition (equal); Methodology (equal); Project administration (equal); Software (equal); Validation (equal); Visualization (equal); Writing – original draft (equal); Writing – review & editing (equal).

DATA AVAILABILITY

The data that support the findings of this study are available from the corresponding author upon reasonable request.

REFERENCES

[1]S. J. Huston and V. Jayaraman, "Studying sensorimotor integration in insects," Curr. Opin. Neurobiol. **21**, 527–534 (2011).
[2]B. H. Dickerson, J. L. Fox, and S. Sponberg, "Functional diversity from generic encoding in insect campaniform sensilla," Curr. Opin. Physiol. **19**, 194–203 (2021).
[3]W. Gnatzy, U. Grunert, and M. Bender, "Campaniform sensilla of *Calliphora vicina* (Insecta, Diptera)," Zoomorphology **106**, 312–319 (1987).
[4]S. P. Sane, A. Dieudonné, M. A. Willis, and T. L. Daniel, "Antennal mechanosensors mediate flight control in moths," Science **315**, 863–866 (2007).
[5]B. R. Aiello, K. E. Stanchak, A. I. Weber, T. Deora, S. Sponberg, and B. W. Brunton, "Spatial distribution of campaniform sensilla mechanosensors on wings: Form, function, and phylogeny," Curr. Opin. Insect Sci. **48**, 8–17 (2021).
[6]B. Pratt, T. Deora, T. Mohren, and T. Daniel, "Neural evidence supports a dual sensory-motor role for insect wings," Proc. R. Soc. B **284**, 20170969 (2017).
[7]B. H. Dickerson, Z. N. Aldworth, and T. L. Daniel, "Control of moth flight posture is mediated by wing mechanosensory feedback," J. Exp. Biol. **217**, 2301–2308 (2014).
[8]A. Eberle, B. Dickerson, P. Reinhall, and T. Daniel, "A new twist on gyroscopic sensing: Body rotations lead to torsion in flapping, flexing insect wings," J. R. Soc. Interface **12**, 20141088 (2015).
[9]B. T. Hinson and K. A. Morgansen, "Gyroscopic sensing in the wings of the hawkmoth *Manduca sexta*: The role of sensor location and directional sensitivity," Bioinspiration Biomimetics **10**, 056013 (2015).
[10]R. J. Wootton, "Support and deformability in insect wings," J. Zool. **193**, 447–468 (1981).
[11]T. Nakata and H. Liu, "A fluid–structure interaction model of insect flight with flexible wings," J. Comput. Phys. **231**, 1822–1847 (2012).
[12]S. A. Combes and T. L. Daniel, "Into thin air: Contributions of aerodynamic and inertial-elastic forces to wing bending in the hawkmoth *Manduca sexta*," J. Exp. Biol. **206**, 2999–3006 (2003).
[13]H. E. Reid, R. K. Schwab, M. Maxcer, R. K. D. Peterson, E. L. Johnson, and M. Jankauski, "Wing flexibility reduces the energetic requirements of insect flight," Bioinspiration Biomimetics **14**, 056007 (2019).
[14]S. Heathcote, Z. Wang, and I. Gursul, "Effect of spanwise flexibility on flapping wing propulsion," J. Fluids Struct. **24**, 183–199 (2008).
[15]M. Moore, "Analytical results on the role of flexibility in flapping propulsion," J. Fluid Mech. **757**, 599–612 (2014).
[16]N. Lee, S. Lee, H. Cho, and S. Shin, "Effect of flexibility on flapping wing characteristics in hover and forward flight," Comput. Fluids **173**, 111–117 (2018).
[17]B. Yin and H. Luo, "Effect of wing inertia on hovering performance of flexible flapping wings," Phys. Fluids **22**, 111902 (2010).
[18]M. Percin, Y. Hu, B. W. van Oudheusden, B. Remes, and F. Scarano, "Wing flexibility effects in clap-and-fling," Int. J. Micro Air Vehicles **3**, 217–227 (2011).
[19]F.-B. Tian, H. Dai, H. Luo, J. F. Doyle, and B. Rousseau, "Fluid–structure interaction involving large deformations: 3D simulations and applications to biological systems," J. Comput. Phys. **258**, 451–469 (2014).
[20]D. Ishihara, T. Horie, and M. Denda, "A two-dimensional computational study on the fluid–structure interaction cause of wing pitch changes in dipteran flapping flight," J. Exp. Biol. **212**, 1–21 (2009).
[21]M. Hamamoto, Y. Ohta, K. Hara, and T. Hisada, "Application of fluid–structure interaction analysis to flapping flight of insects with deformable wings," Adv. Rob. **21**, 1–21 (2007).
[22]T. Fitzgerald, M. Valdez, M. Vanella, E. Balaras, and B. Balachandran, "Flexible flapping systems: Computational investigations into fluid-structure interactions," Aeronaut. J. **115**, 593–604 (2011).
[23]J. Tang, S. Chimakurthi, R. Palacios, C. Cesnik, and W. Shyy, "Computational fluid-structure interaction of a deformable flapping wing for micro air vehicle applications," in *46th AIAA Aerospace Sciences Meeting and Exhibit* (AIAA, 2008), p. 615.
[24]T. Yamada and S. Yoshimura, "Line search partitioned approach for fluid-structure interaction analysis of flapping wing," Comput. Model. Eng. Sci. **24**, 51 (2008).
[25]D. Willis, E. Israeli, P.-O. Persson, M. Drela, J. Peraire, S. Swartz, and K. Breuer, "A computational framework for fluid structure interaction in biologically inspired flapping flight," in *25th AIAA Applied Aerodynamics Conference* (AIAA, 2007), p. 3803.
[26]B. A. Roccia, S. Preidikman, and B. Balachandran, "Computational dynamics of flapping wings in hover flight: A co-simulation strategy," AIAA J. **55**, 1806–1822 (2017).

08 July 2024 15:29:04

Published under an exclusive license by AIP Publishing

[27]J. A. John D., *Computational Fluid Dynamics: The Basics with Applications* (McGraw-Hill Education, 1995).
[28]H. Liu, C. P. Ellington, K. Kawachi, C. van den Berg, and A. P. Willmott, "A computational fluid dynamic study of hawkmoth hovering," J. Exp. Biol. **201**, 461–477 (1998).
[29]S. A. Combes and T. L. Daniel, "Flexural stiffness in insect wings I. Scaling and the influence of wing venation," J. Exp. Biol. **206**, 2979–2987 (2003).
[30]M. Smith, P. Wilkin, and M. Williams, "The advantages of an unsteady panel method in modelling the aerodynamic forces on rigid flapping wings," J. Exp. Biol. **199**(5), 1073–1083 (1996).
[31]M. S. Vest and J. Katz, "Unsteady aerodynamic model of flapping wings," AIAA J. **34**, 1435–1440 (1996).
[32]L. N. Long and T. E. Fritz, "Object-oriented unsteady vortex lattice method for flapping flight," J. Aircr. **41**, 1275–1290 (2004).
[33]M. F. Valdez, B. Balachandran, and S. Preidikman, "Comparative study on analytical and computational aerodynamic models for flapping wings MAVs," Aeronaut. J. **124**, 1636–1665 (2020).
[34]B. A. Roccia, S. Preidikman, J. C. Massa, and D. T. Mook, "Modified unsteady vortex-lattice method to study flapping wings in hover flight," AIAA J. **51**, 2628–2642 (2013).
[35]R. K. Schwab, H. E. Reid, and M. Jankauski, "Reduced-order modeling and experimental studies of bilaterally coupled fluid–structure interaction in single-degree-of-freedom flapping wings," J. Vib. Acoust. **142**, 021012 (2020).
[36]Q. Wang, J. Goosen, and F. van Keulen, "An efficient fluid–structure interaction model for optimizing twistable flapping wings," J. Fluids Struct. **73**, 82–99 (2017).
[37]S. Combes and T. Daniel, "Flexural stiffness in insect wings II. Spatial distribution and dynamic wing bending," J. Exp. Biol. **206**, 2989–2997 (2003).
[38]S. M. Walker and G. K. Taylor, "A semi-empirical model of the aerodynamics of manoeuvring insect flight," J. R. Soc. Interface **18**, 20210103 (2021).
[39]C. Fernandez-Escudero, M. Gagnon, E. Laurendeau, S. Prothin, G. Michon, and A. Ross, "Comparison of low, medium and high fidelity numerical methods for unsteady aerodynamics and nonlinear aeroelasticity," J. Fluids Struct. **91**, 102744 (2019).
[40]H. Reid, H. Zhou, M. Maxcer, R. K. Peterson, J. Deng, and M. Jankauski, "Toward the design of dynamically similar artificial insect wings," Int. J. Micro Air Veh. **13**, 1 (2021).
[41]A. G. Norris, A. N. Palazotto, and R. G. Cobb, "Experimental structural dynamic characterization of the hawkmoth (*Manduca sexta*) forewing," Int. J. Micro Air Veh. **5**, 39–54 (2013).
[42]M. Jankauski, T. L. Daniel, and I. Shen, "Asymmetries in wing inertial and aerodynamic torques contribute to steering in flying insects," Bioinspiration Biomimetics **12**, 046001 (2017).
[43]M. Jankauski and I. Shen, "Dynamic modeling of an insect wing subject to three-dimensional rotation," Int. J. Micro Air Veh. **6**, 231–251 (2014).
[44]R. Schwab, E. Johnson, and M. Jankauski, "A novel fluid–structure interaction framework for flapping, flexible wings," J. Vib. Acoust. **141**, 061002 (2019).
[45]G. J. Berman and Z. J. Wang, "Energy-minimizing kinematics in hovering insect flight," J. Fluid Mech. **582**, 153–168 (2007).
[46]S. P. Sane and M. H. Dickinson, "The aerodynamic effects of wing rotation and a revised quasi-steady model of flapping flight," J. Exp. Biol. **205**, 1087–1096 (2002).
[47]J. Katz and A. Plotkin, *Low-Speed Aerodynamics* (Cambridge university Press, 2001), Vol. 13.
[48]W. Geissler and B. G. van der Wall, "Dynamic stall control on flapping wing airfoils," Aerosp. Sci. Technol. **62**, 1–10 (2017).
[49]M. Jones and N. Yamaleev, "The effect of a gust on the flapping wing performance," in 50th AIAA Aerospace Sciences Meeting Including the New Horizons Forum and Aerospace Exposition, 2012.
[50]H. Hadzic, "Development and application of finite volume method for the computation of flows around moving bodies on unstructured, overlapping grids," Ph.D. thesis (Technische Universität Hamburg, Hamburg, 2006).
[51]A. T. Bode-Oke and H. Dong, "The reverse flight of a monarch butterfly (*Danaus plexippus*) is characterized by a weight-supporting upstroke and postural changes," J. R. Soc. Interface **17**, 20200268 (2020).
[52]J. Reade and M. Jankauski, "Investigation of chordwise functionally graded flexural rigidity in flapping wings using a two-dimensional pitch-plunge model," Bioinspiration Biomimetics **17**, 066007 (2022).
[53]R. Schwab, E. Johnson, and M. Jankauski, "Reduced-order modeling and the physics governing flapping wing fluid-structure interaction," bioRxiv (2021).
[54]W. Shyy, H. Aono, S. Chimakurthi, P. Trizila, C.-K. Kang, C. Cesnik, and H. Liu, "Recent progress in flapping wing aerodynamics and aeroelasticity," Prog. Aerosp. Sci. **46**, 284–327 (2010).
[55]J. D. Anderson, *Fundamentals of Aerodynamics*, 5th ed. (McGraw-Hill, 2011).

08 July 2024 15:29:04

Published under an exclusive license by AIP Publishing

REDUCED-ORDER MODELING AND OPTIMIZATION OF A FLAPPING-WING FLIGHT SYSTEM

Contribution of Authors and Co-Authors

Manuscript in following chapter

Author: Joseph Reade

Contributions: Development of fluid model, integration of system-level model, implmentation of model and optimization

Author: Braden Cote

Contributions: Assisted development of system-level model

Author: Mark Jankauski

Contributions: Development of structural model

Manuscript Information

J. Reade, B. Cote, M. Jankauski

Journal of Nonlinear & Computational Dynamics

Status of Manuscript:
_X_ Prepared for submission to a peer-reviewed journal
____ Officially submitted to a peer-reviewed journal
____ Accepted by a peer-reviewed journal
____ Published in a peer-reviewed journal

American Society of Mechanical Engineers

Reduced-Order Modeling and Optimization of a Flapping-Wing Flight System

J. Reade, B. Cote, M. Jankauski*

Montana State University, Mechanical & Industrial Engineering

(*Electronic mail: mark.jankauski@montana.edu.)

(Dated: 25 July 2024)

Flapping-wing micro air vehicles (FWMAVs) are an emerging technology inspired by flying insects that show promise in applications favoring maneuverability and vehicle compactness. However, current designs are limited by inefficient energetics, and current dynamical models of the flight system employ limiting assumptions when considering power demands. Here, we derive a system-level model of the insect flight system including the thorax, wing and wing hinge that can inform insect-inspired FWMAV design. We apply the model to study the flight system of a hawkmoth and use a genetic algorithm optimization to tune uncertain model parameters to minimize the power required to hover. Results show that performance is improved by utilizing multimodal excitation to produce favorable flapping kinematics. This is achieved by locating the flapping frequency of the moth between the nonlinear resonant frequencies, resulting in magnified flapping response and aerodynamically-advantageous phase. The optimal flapping frequency can be predicted from the system's underlying linear natural frequencies and is roughly 54% of the system's mean natural frequency. Furthermore, effective solutions are configured so that the timing of the applied load and thorax responses are matched such that little effort is spent reversing the wing stroke. The optimized model parameters and corresponding kinematics show moderate agreement with those reported for the hawkmoth. To maintain hovering flight, the successful moths in the population expend approximately 58.5W/kg, where previous estimates place the value nearer to $23-42$W/kg. The system-level model and the governing principles identified in this work can inform the design of energy-efficient FWMAVs moving forward.

I. INTRODUCTION

Flapping-wing micro air vehicles (FWMAVs) are an emerging technology with significant potential in several applications such as urban search-and-rescue or artificial pollination ([1,2]). As their name implies, FWMAVs use flapping wings to generate the lift and thrust necessary for flight ([3]). Flapping wings enable FWMAVs to maintain energetic efficiency at millimeter-centimeter length scales ([4–6]), whereas conventional fixed and rotary wing vehicles operate with reduced efficiency at these reduced sizes ([7,8]). The potential for reduced size is advantageous in scenarios with space-constricted environments, such as urban search and rescue in collapsed buildings. They may also operate in natural settings with minimal disruption to surrounding wildlife. However, before FWMAVs are widely adopted, certain obstacles must be overcome, such as determining optimal flapping kinematics and how these kinematics are practically realized ([3,9]).

Flapping wing flight is not yet as well understood as fixed-wing or rotating blade flight. To better understand flapping wings, researchers have turned to insect flight for inspiration. Hovering flight is energetically costly, and to accommodate high energetic demands, insects have evolved mechanisms to improve aerodynamic and energetic performance. One such trait is the use of indirect flight muscles (IFMs)([10–12]), which regulate both flight and other behaviors in many insects ([13–15]). In insects with IFMs, the primary flight muscles attach to opposing sides of the flexible thoracic exoskeleton ([16]). These muscles deform the thorax when activated, and this deformation is transmitted to the wing via a complex lever mechanism known as the wing hinge. The wing hinge converts small thoracic deflections into large wing rotations ([17]). The thorax acts as a spring, storing elastic potential energy when it is deformed and releasing that energy when it returns to its original state. During flight, this mechanism reduces the effort invested during stroke reversal, leading to lower overall energetic requirements ([18]). Many insect species are also believed to flap near the resonant frequency of the coupled thorax-wing system, further reducing the load borne by the flight muscles to achieve the same wing motion ([19]).

Although the thorax is an essential component in the flight mechanism of many insects, modeling efforts have generally examined only a single component of the flight system in isolation ([20–25]). For example, there is a substantial body of work focused on the aerodynamics of flapping-wing flight ([26–29]). Simpler fluid models may use quasi-steady aerodynamics, where the flow history is neglected and lift is purely circulatory, generated by redirecting the induced airflow downwards ([30,31]. More complex methods can account for unsteady lift-enhancement mecha-

nisms such as leading-edge vortex shedding and clap-and-fling, believed to aid in the flight of some insects ([32–34]). However, these models are limited in their ability to accurately estimate energy expenditures. Negative power is often ignored by these models because it is assumed to result from unmodeled restorative forces (e.g., spring forces from the thorax) upstream of the flapping wing. Practically, negative power could also result from non-conservative muscular forces if the muscles are functioning to decelerate the wing's flapping motion. By modeling the thorax explicitly, the assumptions surrounding the source of negative power can be removed.

Dynamical models that account for both the wing and thorax often have other limitations. For example, thorax deformation is usually prescribed within these models, thereby neglecting interactions between the wing and thorax ([35,36]). Other efforts that account for coupled wing-thorax dynamics explicitly reduce wing kinematics to unrealistic non-lifting single-degree-of-freedom rotation ([37]). Non-lifting models are useful in providing physical insights into the system dynamics of flight, but are limited in informing the design of real robotic vehicles that must support their own weight. Thus, there remains a need for a system-level model that considers wing-thorax interactions and realistic wing kinematics and aerodynamics.

Here, we develop a mathematical model of a coupled thorax-wing system and demonstrate the utility of the model using the hawmkoth *Manduca sexta*. This system-level model (SLM) allows the wing two rotational degrees of freedom, pitch and roll, permitting better estimates of aerodynamic loading when compared to single-degree-of-freedom flapping kinematics. The model uses a quasi-3D vortex lattice method to estimate aerodynamic loads on the wing, thereby enabling predictions the lift generated by the system. The inclusion of the thorax allows power calculations to inherently account for elastic energy storage, whereas most existing fluid models of insect wings must assume some recycling efficiency ([38,39]). We assume that the overall thorax-wing assembly cannot translate or rotate, so our model best represents hovering. We employ a genetic algorithm based optimization to tune unknown system parameters in an effort to minimize the energetic cost of hovering. General evolutionary trends of the population are presented and discussed, before discussing a select few optimized configurations in greater depth. From these results, we draw conclusions about the behavior of the system that may guide FWMAV design principles.

II. METHODS

A. Structural Modeling

We developed a simplified dynamical model of the flight system of a flapping wing insect. The system-level model (SLM, Fig. 1) was extended from the efforts of ([37]) to accommodate multiple degree-of-freedom wing rotation and unsteady aerodynamics.

The thorax is treated as a spring-mass with stiffness k_T and mass m_T and is constrained to move along a single axis with displacement x_T. The wing is a rigid, thin plate with uniform properties and has two rotational degrees of freedom, pitch ϕ and roll θ. Roll is defined about a globally fixed axis 'X' passing through the wing hinge. Pitch is defined as rotation about a 'y' axis fixed to the leading edge of the wing. The thorax and the wing are connected via a lever representative of the wing hinge. Thorax deformation x_T is linearly related the wing roll angle θ by

$$x_T = \lambda\theta \tag{1}$$

where λ is the transmission ratio of the hinge. The indirect flight muscles generate a prescribed harmonic force $F(t)$ that acts on the thorax collinear to x_T. Indirect flight muscle force and thorax motion are transmitted through the hinge to the wing to generate rolling motion. Pitch occurs passively as a result of inertial and aerodynamic moments. Previous work suggests that passive wing pitching due to these loads occurs in multiple insect species, including *M. sexta*([40]). We assume that the system is symmetrical, so only a single wing is modeled. Although insect wings are flexible in nature, the model wing was kept rigid so that the wing-thorax interactions could be studied without the complexity of wing deformation. Future modeling efforts will incorporate wing flexibility.

Equations governing the pitch and roll system dynamics were formulated using the Lagrangian approach. Kinetic energy T and potential energy V for the wing and thorax are

$$T_{thorax} = \frac{1}{2}m_T(\lambda\dot{\theta})^2 \tag{2}$$

$$T_{wing} = \frac{1}{2}\vec{\Omega}^T\mathbf{I}_0\vec{\Omega} \tag{3}$$

$$V_{thorax} = \frac{1}{2}k_T(\lambda\theta)^2 \tag{4}$$

$$V_{wing} = \frac{1}{2}k_\phi(\phi)^2 \tag{5}$$

where $\vec{\Omega}$ is the angular velocity vector of the wing referenced from a xyz wing-fixed reference

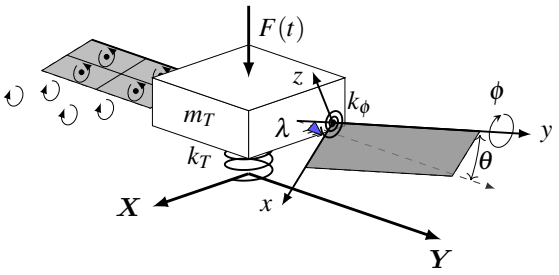


FIG. 1. System-level model configuration. Note that only one wing is explicitly modeled, and the other is accounted for via symmetry arguments. XYZ denotes a globally fixed Cartesian coordinate system and xyz denotes a wing-fixed Cartesian reference frame

frame (Fig. 1) and given by

$$\vec{\Omega} = \begin{Bmatrix} \dot{\theta}\cos\phi \\ \dot{\phi} \\ \dot{\theta}\sin\phi \end{Bmatrix} \tag{6}$$

$\mathbf{I}_0$ is the inertia tensor of the wing, and for a thin flat plate takes the form of

$$\mathbf{I}_0 = \begin{bmatrix} I_{xx} & I_{xy} & 0 \\ I_{yx} & I_{yy} & 0 \\ 0 & 0 & I_{xx}+I_{yy} \end{bmatrix} \tag{7}$$

where I_{xx} and I_{yy} are the mass moments of inertia about the wing root and leading edge, respectively, and I_{xy} is the product of inertia. The Lagrangian formulation gives the equations of motion governing wing roll and pitch as

$$\ddot{\theta}[m_T\lambda^2 + I_{xx} + I_{yy}\sin^2\phi] + \ddot{\phi}[I_{xy}\cos\phi] + \dot{\theta}\dot{\phi}[I_{yy}\sin 2\phi] + \dot{\phi}^2[-I_{xy}\sin\phi] + \theta[k_T\lambda^2] \;=\; Q_\theta \tag{8}$$

$$\ddot{\theta}[I_{xy}\cos\phi] + \ddot{\phi}[I_{yy}] + \dot{\theta}^2[-\frac{1}{2}I_{yy}\sin 2\phi] + \phi[k_\phi] \;=\; Q_\phi \tag{9}$$

where Q_θ and Q_ϕ are the non-conservative moments about the roll and pitch axes, respectively. These loads comprise applied loads, aerodynamic moments, and system viscous damping. The applied load is the prescribed thorax force converted to a moment about the roll axis, and the aerodynamic moments are determined using the unsteady vortex lattice solver described in Section II B. Aerodynamic moments were found by integrating the product of the local pressure δp over

the wing surface S_{wing} and distance from the relevant axis, i.e,

$$M_{X,aero} = \cos\phi \int_{S_{wing}} y\delta p \tag{10}$$

$$M_{y,aero} = \int_{S_{wing}} x\delta p \tag{11}$$

The power P_{appl} of the applied load acting on the thorax is

$$P_{appl} = \dot{x}_T F(t) \tag{12}$$

where $\dot{x}_T$ is the thorax velocity and F is the prescribed muscle force acting on the thorax. The mean total power exerted by the moth is simply the time-averaged rectified input power, i.e

$$\bar{P}_{in} = \frac{1}{T}\int_T |P_{appl}|dt \tag{13}$$

Where T is the duration of one loading cycle, or wingbeat.

B. Fluid Modeling

Aerodynamic loads on the wing were estimated using a quasi three-dimensional unsteady vortex lattice method (UVLM). The specific formulation used here was developed in ([39,41]), and is discussed in-depth in Appendix A. The UVLM, described in detail by Katz & Plotkin ([42]), is a potential flow method that makes several simplifying assumptions about the fluid. The fluid is incompressible and inviscid, so shear forces are neglected. Flow features must be specifically modeled, e.g. vortex shedding and leading-edge separation. Despite these limitations, the balance of accuracy and speed means the UVLM is frequently used when modeling flapping wings ([43–46]). In contrast to many high-fidelity methods, such as Reynolds-averaged Navier-Stokes, the flow field surrounding the wing does not need to be resolved, thereby enabling solutions to be obtained in a small fraction of the time.

To employ the quasi-3D UVLM, the wing is divided spanwise into multiple blades, each of which runs from the leading edge of the wing to the trailing edge. The aerodynamics of each blade are solved individually using a 2D UVLM method. Time-dependent effects are modeled via the inclusion of wake shedding, where wake vortices are generated at the trailing edge of the wing and advected with the flow. The aerodynamic pressures on each blade are estimated individually using a 2D fluid solver. These are then converted into moments about the pitch and roll axes (Eqs. 10-11) and used in the system equations of motion (Eqs. 8- 9) as applied loads. The results for each blade are summed together to obtain total forces and moments acting on the wing.

TABLE I. **SLM fixed parameters**

Quantity	Value	Unit
Wing span	5	cm
Wing chord	2	cm
Wing mass	50	mg
Thorax mass	350	mg
Moth weight	10	mN
Flapping frequency	25	Hz

C. Implementation and Optimization

1. Simulation Parameters

Here, we implement the SLM using the hawkmoth *M. sexta* as the model insect. The parameters used in the SLM are approximated from the morphology of *M sexta*. Thorax mass and the total body weight are based on ([38]). The wing is idealized as rectangular with values for span and average chord taken from ([47]) and wing mass from ([38]). The IFM actuation frequency, assumed equal to the flapping frequency, was taken from ([48]). All fixed parameters are shown in Table I. Rayleigh damping was implemented to facilitate numerical stability. Rayleigh damping constants were determined based on the system's two undamped natural frequencies such that a 5% modal damping ratio was achieved for the two modes of the underlying linear system. Rayleigh damping took the form of viscous damping terms inside the non-conservative moments Q_θ and Q_ϕ in Eqs. 8 and 9.

Within the UVLM aerodynamic model, the wing is discretized into blades, and the blades subsequently discretized into panels. UVLM simulation parameters are listed in Table II. The wake is separated into point vortices, one of which is generated at each time step. To maintain computational efficiency, only a set number of wake vortices are retained, with the oldest being eliminated to make room for the newly-shed vortex. Values for panels-per-blade, maximum wake vortices, and time-steps-per-wingbeat are set based on convergence studies performed in ([39]). The model is implemented in MATLAB (V2023b), and integration of the equations of motion (Eqs. 8-9) between time steps is performed using ode15s, a built-in MATLAB function.

TABLE II. **UVLM simulation parameters**

Quantity	Value
Number of blades	5
Panels per blade	20
Time steps per period	200
Wakes stored per blade	100
Number of wingbeats	13

TABLE III. **Evolved parameters and bounds**

Quantity	Symbol	Lower	Upper	Unit
Pitching Stiffness	k_ϕ	0.05	2.5	mNm/rad
Transmission Ratio	λ	0.1	4.0	mm/rad
Thorax Stiffness	k_T	0.005	2.5	kN/m
Thorax Force Amplitude	$F_{T,0}$	0.5	1.25	N

2. Optimization

The system model described in the previous sections is defined by parameters such as wing geometry, thorax mass, thorax stiffness, and so on. Many of these model parameters are easily accessible within the literature (Tab. I. However, other model parameters, such as transmission ratio, are not reported explicitly but instead would need to be inferred from previous studies. Thus, we use a constrained optimization to determine values for model parameters that do not have values readily available from the literature. The objective of the optimization routine is to minimize the average power required to maintain hovering flight. In the discussion, we compare our optimized set of parameters with estimates of these parameters reported in the literature. The fixed system parameters are detailed in Table I. The parameters to be varied, as well as their permissible lower and upper bounds, are detailed in Table III.

Optimization is conducted via a user-defined genetic algorithm (GA). GA is a broad class of optimization technique inspired by biological evolution([49,50]). At any point in the GA process, there exists a number of candidate solutions to the optimization problem. Collectively, these are called the population, and each candidate solutions is an individual, or in this case, a moth. Each

moth has one chromosome containing four genes, each representing one of the parameters listed in Table III. At each iteration, or generation, all moths in the population are individually simulated using the SLM. The population performance is then evaluated, and a new population is generated from the current one. Moths that better meet the objective and constraints are more likely to be represented in the next generation than are under-performing moths.

The goal of this optimization is to maximize the hovering efficiency of the configuration. Accordingly, our objective function value (OFV) is

$$OFV = \frac{1}{\bar{P}_{in}} \tag{14}$$

where $\bar{P}_{in}$ is the steady-state mean power consumption. For sustained hovering flight, we constrain the lift to be equal to weight, with a 1% margin of error (Table IV). The margin of error is introduced because the semi-random nature of genetic algorithms, as well as lift being a simulation constraint, make meeting exact equality constraints difficult ([51]). This constraint was used to prevent lift becoming a confounding variable, as flight efficiency is likely to be dependent on total lift production, with proportionally lower power requirements at decreased lift values. To keep the solutions within the realm of plausibility, we also constrain the wing kinematics. As there is no wing-wing or wing-body collision, there is nothing inherent to the model that prevents the wing from experiencing excessive pitch and roll deflections, e.g. the wing roll performing full rotations around the body. In addition to being physically unrealistic, these kinematics would likely break certain limits of the UVLM and result in inaccurate aerodynamic force and, through the coupling, the system dynamics. Therefore, the steady-state pitch and roll angles are limited to not exceed a predefined angle, listed in Table IV.

Objective function and constraints are implemented as described in ([51]). A constraint violation (CV) is calculated for each individual. The CV is a single measure of how well a solution meets all the constraints collectively. If $CV = 0$, then a solution is feasible. If $CV > 0$ then a solution is infeasible. Once every individual in the population has been evaluated, they are ranked in order of desirability. A feasible moth is always preferable to an infeasible moth. If both are feasible or both are infeasible, the one with the better objective function value or lower CV is preferred, respectively. A new population is then created using the current ranked population as a guide. The implementation of the GA is described in more detail in Appendix B.

Once a new generation has been formed through the process described above, the individuals in it are simulated using the described system level model, and the process repeats until the maximum

TABLE IV. **Optimization constraints**

	Lower	Upper	Units
Mean Lift	9.9	10.1	mN
Roll	−70	70	degrees
Pitch	−70	70	degrees

number of generations is reached. The full GA optimization process was repeated 300 times, each producing an independent set of solutions. The best-performing moth produced by each run was identified and collected into a new population, presented in Section III.

III. RESULTS

Here, we discuss the population results of the genetic algorithm. We investigate where the four parameters evolved towards, and how this correlates to efficiency, defined as mean lift production divided by mean applied power $\bar{P}_{in}$. Also discussed are system energetic losses resulting from braking power due to mismatched muscle and velocity phase, and aerodynamic power resulting from the fluid moments on the wing. Then, we analyze the frequency responses of specific individuals from the optimization to better understand the proximity in which they operate with respect to non-linear resonances.

1. Parameter Trends

Figure 2 shows the evolved parameters versus efficiency for all individuals optimized through the genetic algorithm. Pitching stiffness k_ϕ evolves towards a narrow band of values, with 47% of solutions falling between 0.5 and 0.6 mNm/rad. A single solution lands below 0.5 mNm/rad, and the remaining solutions are approximately uniformly distributed between 0.6 and 1.8 mNm/rad. The median value is 0.61 mNm/rad. There is a clear relationship between pitching stiffness and maximum efficiency, with the highest efficiency occurring at the lower end of the range, and decreasing as pitching stiffness is increased. The transmission ratio λ similarly converges to a narrow region at high efficiencies, typically in the range of 0.8 to 1.7 mm/rad, and the median transmission ratio is 1.54 mm/rad.

In contrast to the first two parameters, there is significant variation in thorax stiffness k_T and

thorax forcing amplitude $F_{T,0}$, even at high efficiency. There is perhaps no clear trend in the thorax parameters because the influence of the thorax quantities on the system dynamics are also dependent on the transmission ratio. For example, in Eq. 8, the term containing k_T is multiplied by the square of λ, and the applied component of the load Q_θ is the product of thorax force and λ. If translational thorax quantities are converted to angular roll stiffness k_θ and applied roll moment $M_{\theta,0}$ via

$$k_\theta = \lambda^2 k_T \tag{15}$$

$$M_{\theta,0} = \lambda F_{T,0} \tag{16}$$

convergence trends become more apparent (Fig. 3). Maximum efficiency generally increases as either parameter is lowered, and both converge on relatively narrow bands compared to the range of values present. Angular roll stiffness and roll moment have median values of 1.63 mNm/rad and 1.32 mNm, respectively. Lower values of roll stiffness may result less favorable dynamics, or in the roll angle exceeding the constraint.

2. Energetic Losses

To identify why certain individuals within the population are more efficient than others, we analyze the energetic losses present in the flapping wing system. There are two mechanisms of energetic inefficiency –'braking' the wing kinematics and aerodynamic dissipation (e.g., pressure drag). Braking losses occur when the applied muscular force acts counter to the motion of the thorax. This means that effort is spent to actively reduce the energy of the system rather than relying on the passive elasticity of the thorax or aerodynamics. The braking power $\bar{P}_{brake}$, or time-averaged power spent to slow the wing motion is the total negative energy expenditure per wing beat divided by the duration of the wing beat T, is

$$\bar{P}_{brake} = \frac{1}{T}\int_T P^-_{appl} dt \tag{17}$$

where P^-_{appl} is just the negative component of P_{appl}. Figure 4 shows efficiency as a function of the braking power relative to the total input power, i.e $(\bar{P}_{brake}/\bar{P}_{in}) \times 100$, or the percentage of the effort by the moth is spent decelerating the wing. This indicates that while reduced braking power is required for high efficiency, it is not sufficient in itself. While all high-efficiency solutions require minimal braking power, a significant fraction of the lower-efficiency individuals also have minimal braking power. Over 60% of the moths use less than one-percent braking power.

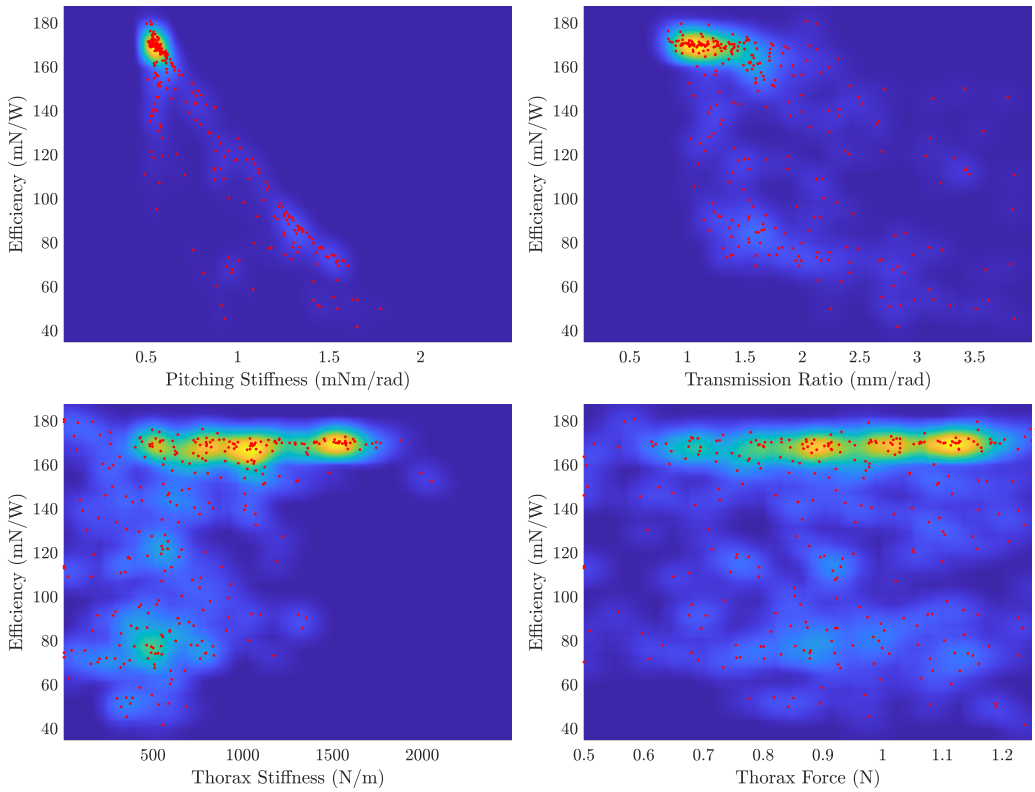


FIG. 2. Population results for evolved parameters. Clockwise from top left: pitching stiffness k_ϕ, transmission ratio λ, thorax force amplitude $F_{T,0}$, thorax stiffness k_T. Red dots indicate individual solutions. Colored background is relative density of solutions

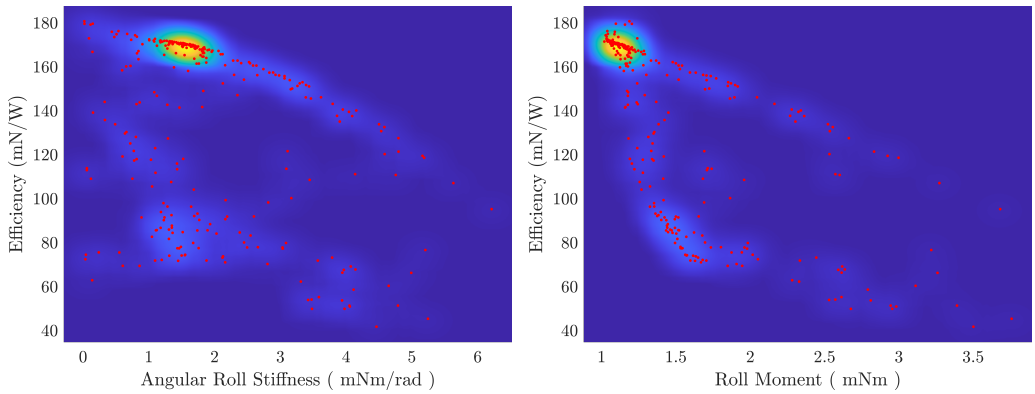


FIG. 3. Angular equivalent of evolved parameters. Left: angular stiffness k_θ. Right: applied moment amplitude $M_{\theta,0}$. Red dots indicate individual solutions. Colored background is relative density of solutions

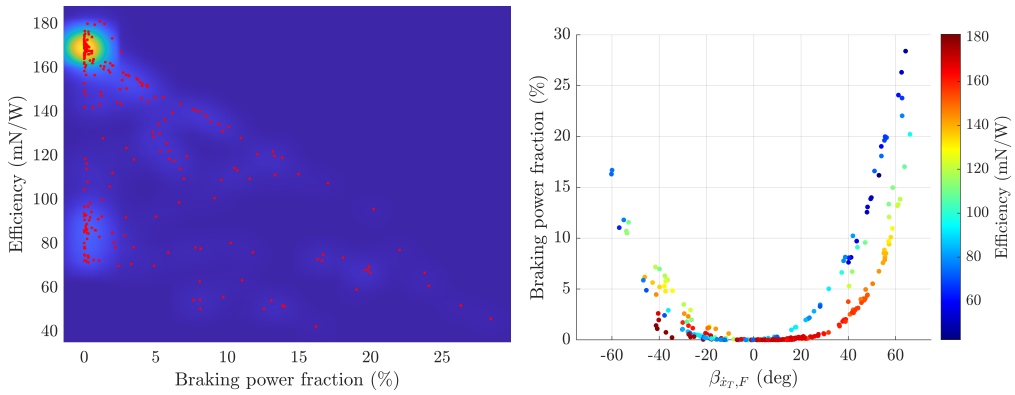


FIG. 4. (Left) Population distribution, efficiency vs braking power percent of total power. Red dots indicate individual solutions, colored background is relative density of solutions. (Right) Braking power percent of total power, relative to phase delay between thorax velocity and applied load

As a measure of how closely the thorax deformation matches the applied thorax force, we calculate the phase difference $\beta_{\dot{x}_T,F}$ between the thorax velocity $\dot{x}_T$ and the prescribed load F. The thorax response is periodic but not strictly harmonic, so only the component of thorax velocity corresponding to the flapping frequency is used. We see that for the population as a whole, braking losses as a percent of total power are minimized when $\beta_{\dot{x}_T,F}$ is near zero (Fig. 4). This is expected, as a small phase difference suggests that the thorax load is typically acting in the same direction as the velocity. When they are opposed, the load and velocity are likely to be small, thereby reducing the magnitude of the loss. The high-efficiency group is centered around $\beta_{\dot{x}_T,F} = 10°$. Braking losses appear to be easily minimized, and a relatively insignificant contributor to energetic requirements.

The second driver of energetic dissipation is aerodynamic power P_{aero}. Aerodynamic power is due to the fluid forces acting on the wing, typically opposing the motion of the system, and is given by

$$P_{aero} = \dot{\theta} M_{X,aero} + \dot{\phi} M_{y,aero} \tag{18}$$

Aerodynamic power accounts for a large share of the total energetic cost in a majority of moths (Fig. 5). The fluid forces that act on the wing can be separated into lift and drag. Lift is responsible for the flight ability of moth, while drag (defined here as pressure drag and not viscous drag) is the primary contributor to aerodynamic energy losses. Here, drag is the aerodynamic force acting in opposition to the rolling motion of the wing. Efficiency can be improved by decreasing drag and aerodynamic dissipation while still maintain the same mean lift. Half of the solutions have

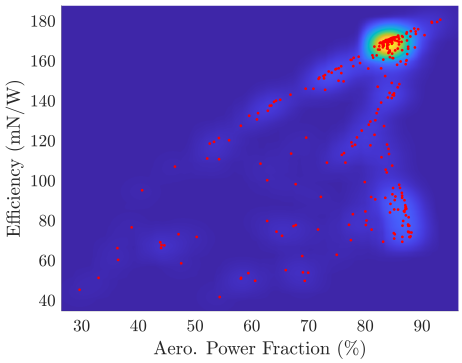


FIG. 5. Efficiency vs aerodynamic power P_{aero} as a percentage of the total input power P_{in}. Red dots indicate individual solutions, colored background is relative density of solutions

aerodynamic dissipation equaling at least 84% of the total input power, and there is a strong positive relationship between the aerodynamic power fraction and the maximum attainable efficiency. Minimizing the overall aerodynamic power while keeping it at a high fraction of the total power is a priority when optimizing the configuration.

The total pressure force on the wing will be strongly tied to the instantaneous roll rate $\dot{\theta}$ and pitch angle ϕ. Since the pressure acts normal to the wing, the relative magnitudes of lift and drag acting on the wing are determined by the pitch angle, with more drag being produced the closer ϕ is to zero. Based on stady-state aerodynamics, lift and aerodynamic power should scale quadratically and cubically with roll rate $\dot{\theta}$, respectively. In Figure 6, there are two clusters of solutions, one with high pitch and low roll amplitudes (ϕ_0 and θ_0), and a second with the opposite. The first group is made up of moths that have much lower aerodynamic dissipation than those in the second group. Under the hover constraint, all viable solutions have nearly the same mean lift production. If the pitch angle is decreased, the aerodynamic force tilts towards drag and lift is typically reduced. To produce enough lift to maintain hovering flight, the overall aerodynamic force must be increased, and this is accomplished by sweeping the wing faster, over a greater distance each wing beat. In addition to increasing drag, the faster roll rate $\dot{\theta}$ leads to higher power since both the applied load and the aerodynamic load are acting on faster-moving objects.

In a similar manner, the phase between the roll and pitch kinematics also impacts the energetic losses through aerodynamics. The phase, $\beta_{\theta,\phi}$, indicates the timing of roll relative to pitch. Since θ and ϕ are periodic but not strictly harmonic, the phase between the two was evaluated only at the flapping frequency. If $\beta_{\theta,\phi}$ is close to 0°, hereafter referred to as 'in-phase', then the wing velocity

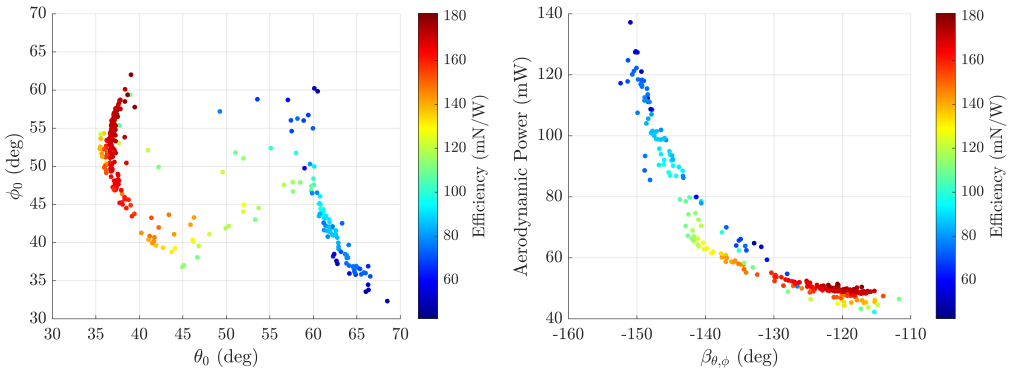


FIG. 6. (Left) Energetic efficiency as a function of kinematic amplitudes, and (Right) of aerodynamic power and roll-pitch phase

is greatest when the pitch angle is near zero. This will generate a significant amount of drag and little lift, requiring high overall force production in order to maintain hover, therefore reducing efficiency. In contrast, if $\beta_{\theta,\phi}$ is near $-90°$, then lift production should be less costly in terms of aerodynamic dissipation. Lift would be negative if $\beta_{\theta,\phi}$ were near $+90°$. From Fig. 6, there is a clear correlation between $\beta_{\theta,\phi}$ and the aerodynamic power dissipated. The phases present in the population range approximately from $-150°$ to $-110°$.

3. Frequency Response

The population-level results above do not inform us about the response of individual moths to changing conditions or their resonant behavior. Because the system is highly nonlinear due to inertial and aerodynamic effects, the system's effective resonant frequencies are most easily determined through numerical sweeps. We are interested in identifying nonlinear resonances because many insects are believed to flap at the resonant frequency of their flight system ([19]). Such insights may further explain why the population traits evolved towards specific values, and how these configurations are most efficient.

We narrow our focus to two of the moths from the above population to examine in greater detail. The first moth selected is the solution with the lowest efficiency, at roughly 42 mN/W. Out of the 300 optimized moths, this is considered 'worst'. We also select an individual that falls within the typical high-efficiency clusters, and refer to this as the 'common' moth, representative of the bulk of successful solutions. The common moth operates at an efficiency of 171 mN/W, just 10 mN/W

TABLE V. **Selected individuals**

	Common	Worst
k_ϕ (mNm/rad)	0.54	1.65
λ (mm/rad)	1.04	2.83
k_T (N/m)	1536	557
$F_{T,0}$ (N)	1.1	1.24
ω_1 (Hz)	27.6	45.1
ω_2 (Hz)	78.6	128.9
ω_m (Hz)	46.6	76.2
Efficiency (mN/W)	171	42.4

or 5% shy of the maximum efficiency produced by the GA.

The 'best' moth is ignored for most of this discussion, for a couple reasons. The low stiffness of this moth thorax made analysis difficult, and the failure of the numerical solver prevented us from fully exploring it's frequency response. It also likely resulted in the normal system dynamics being overpowered by the aerodynamic effects, making the response less predictable, so inferences about broader population behaviour may be erroneous. Lastly, we believe the high efficiency may be in part an artifact of the Rayleigh damping, and the significantly lower damping coefficients in the 'best' moth result in lower viscous energy dissipation compared to the stiffer moths. We therefore focus primarily on the 'common' and 'worst' moths.

The evolved parameters of these moths, as well as the natural frequencies of the underlying linear system and the identified efficiencies, are shown in Table V. For each moth, the excitation frequency is varied from 10 Hz to 160 Hz in increments of 0.5 Hz. At each frequency increment, the model is started from rest and run to 50 cycles of the applied force (hereafter referred to as wing beats). Steady-state wing kinematics are taken from the final five simulated wing beats. We do not consider variable forcing amplitude within individual moths, but note that the depicted responses will vary with force amplitude as well.

To facilitate data interpretation, we introduce several additional quantities. The natural frequencies of the underlying linear system, denoted ω_1 and ω_2, are calculated from the linearized versions of the equations of motion described (Eqs. 8-9). Using these, we calculate a single value representing the overall natural frequency of the linear system. We call this the mean natural

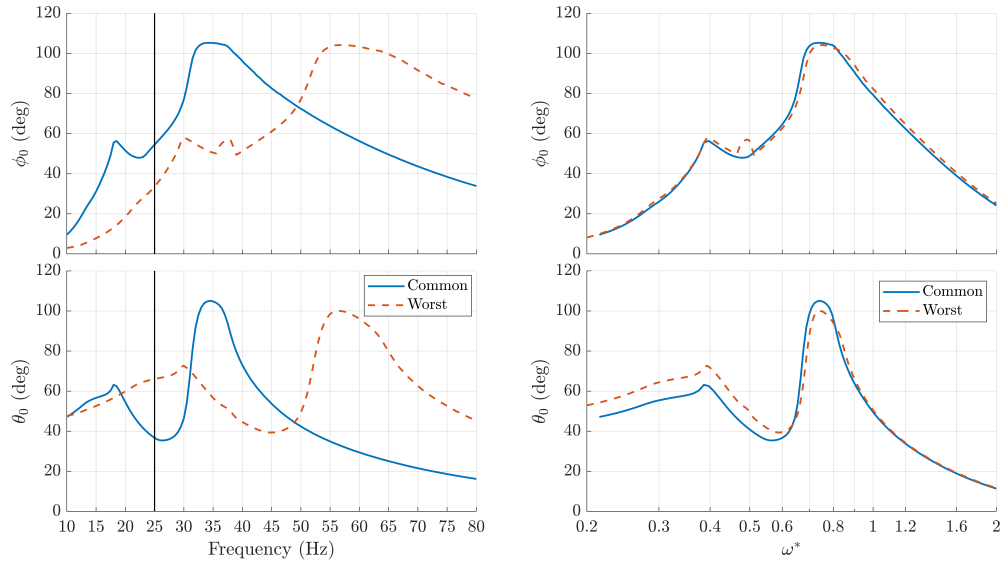


FIG. 7. Relation between maximum kinematic responses and flapping frequency (left) and non-dimensional flapping frequency (right). Vertical black line on the left indicates the flapping frequency used in the GA

frequency ω_m, and it is obtained by taking the geometric mean of the first and second natural frequencies, i.e. $\omega_m = \sqrt{\omega_1 \omega_2}$. Flapping frequency is non-dimensionalized by dividing it by this mean frequency: $\omega^* = \omega_F / \omega_m$.

We first investigate the maximum pitch and roll responses ϕ_0 and θ_0, as a function of flapping frequency ω_F (Fig. 7). Using these results, we estimate the nonlinear resonant frequencies of each moth (Table VI). Pitch and roll nonlinear resonant peaks occur at similar frequencies, so they will not be distinguished from one another. The first and second nonlinear resonant frequencies of the 'common' moth bracket the flapping frequency used in the optimization (25 Hz), while the 'worst' moth has both resonant peaks occurring at frequencies greater than the flapping frequency. When the kinematic response is viewed against non-dimensional flapping frequency ω^*, both cases appear similar. The first and second resonance peaks occur at $\omega^* \approx 0.4$ and $\omega^* \approx 0.75$, respectively. Furthermore, across an order-of-magnitude change in ω^*, pitch amplitude ϕ_0 is nearly identical for both cases. Agreement is likewise seen in the roll amplitude response θ_0, though the cases diverge slightly at reduced ω^*. The 'common' and 'worst' moths both have their first nonlinear resonant frequency at about 66% of ω_1, and the second nonlinear resonance at about 44% of ω_2. It follows that the mean nonlinear resonant frequency Ω_m is approximately $0.54\omega_m$ for both moths. The aerodynamic dissipation drives this reduction of resonant frequencies between the linear and

TABLE VI. **Nonlinear resonant frequency**

	Common	Worst
Ω_1 (Hz)	18	30
Ω_2 (Hz)	34.5	56.5
Ω_m (Hz)	24.9	41.2

nonlinear system.

Next, we examine lift and efficiency across flapping frequencies (Fig. 8). Starting at low frequency, lift production is near zero due to the reduced velocity of the wing. Lift increases with ω^* until the first resonant frequency Ω_1 is reached, where it rapidly climbs until plateauing near $\omega^* = 0.43$ Maximum lift production is at a frequency roughly 80% higher than that at the first resonance. Lift remains relatively constant, decreasing slightly until $\omega^* = 0.6$ before the second resonant frequency Ω_2 Increasing frequency past this point results in lift dropping rapidly, reaching large negative values (-50 mN for 'common' and -118 mN for 'worst'). Lift remains negative for all higher frequencies tested, but does approach zero as the kinematics amplitudes θ_0, ϕ_0 and phase $\beta_{\theta,\phi}$ approach zero as well. Efficiency has a similar frequency response, with the highest lift-per-unit-power occurring at flapping frequencies roughly between Ω_1 and Ω_2. When viewing the response to dimensional flapping frequency, the 'common' moth performs best, in terms of lift production and efficiency, near the flapping frequency used in the GA optimization. The 'worst' moth, in contrast, has an optimal flapping frequency above that used in the optimization.

IV. DISCUSSION

Flying insects are popular model organisms for flapping wing micro air vehicles. However, the models used to evaluate the performance of the insect flight mechanism often focus narrowly on the flapping wing without considering interactions with other components, such as the thorax or wing hinge. Here, we derived a system-level model (SLM) of the insect flight system. Included in the SLM are the insect thorax, the wing hinge and the wing, enabling a more accurate estimation of the energetic requirements compared to existing models. We applied the SLM to simulate the flight system of a hawkmoth *M. sexta*, and used a genetic algorithm to optimize certain model parameters to minimize the power consumed during flight. We identified multiple trends that led to high efficiency in the evolved population of moths.

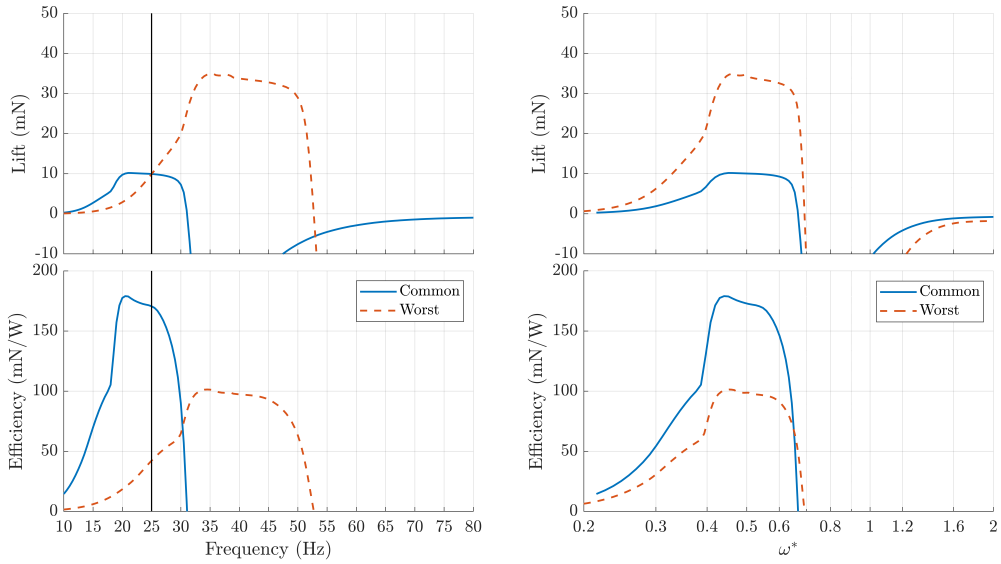


FIG. 8. Mean lift production (top) and efficiency (bottom) as a function of flapping frequency, dimensional (left) and non-dimensional (right). Vertical black line on the left indicates the flapping frequency used in the GA

In this section, we discuss how the optimal solutions, arrived at by the genetic algorithm, resemble the actual *M. sexta*. Then we examine how the successful moth configurations may be taking advantage of multimodal excitation to produce aerodynamically-favorable flapping kinematics to increase efficiency. This is followed by a discussion on modeling energy recycling in the thorax, and a comparison of power estimates to previous estimates. Lastly, we put forward conclusions that could help inform the design of FWMAVs in the future.

1. Biological Comparison

How does the model of the insect flight system compare to the insect that it is based on? Here, we compare the findings of our model with the data available for the hawkmoth *M. sexta* or similar species. We specifically consider the 'common' moth discussed in the results section, which best represents the population of moths evolved through GA.

Ando and Kanzaki simultaneously recorded thorax deformation and wing rotation in *Agrius convolvuli*, a hawkmoth with morphology similar to *M. sexta* ([52]). From their data, we estimate the transmission ratio to be approximately 0.9 mm/rad. In comparison, the 'common' moth has a

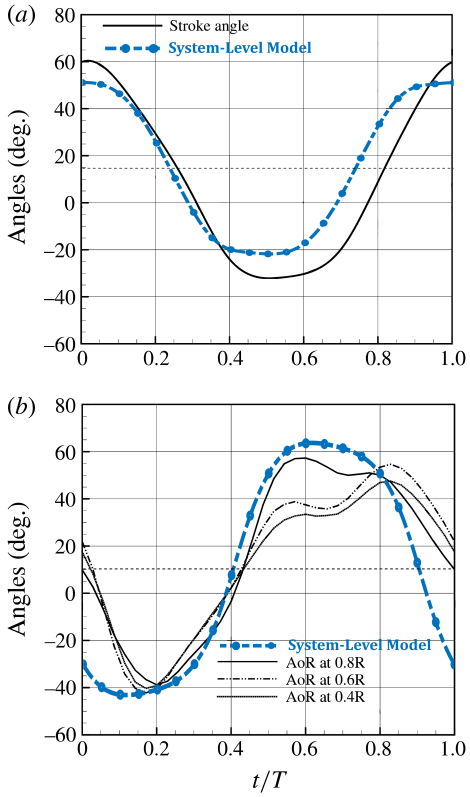


FIG. 9. Hawkmoth wing kinematics in hovering flight for (a) roll (stroke angle) and (b) pitch (called AoR in the comparison study). Dashed blue indicates data from the SLM for 'common' moth, set over results from ([55]). To account for upstroke-downstroke asymmetry, SLM data has been translated vertically so that the mean lies midway between the extrema of the experimental data. In (b), the angle from ([55]) is given at three spanwise locations due to wing twist, denoted 0.4R, 0.6R and 0.8R, where R is the wing length

transmission ratio of 1.04 mm/rad, and the median transmission ratio among the final population was roughly 1.54 mm/rad. Gau et al. found the thorax dorsolongitudinal stiffness to be roughly 3 kN/m ([18]), while the 'common' moth has a thorax stiffness of 1.54 kN/m. Since only half of the moth is modeled, these thorax stiffness values are similar. In-vivo muscle force estimates vary, but tend to be in the range of about 1.0 - 2.25 N ([53,54]). The muscle force converged at about 1.1 N for the 'common' moth and consequently falls within this range. To our knowledge, the effective pitching stiffness of the hawkmoth wing has not been reported in the literature. Thus, the parameters estimated by the GA optimization for the 'common' moth agree reasonably well with the parameters measured in the *M. sexta*.

Next, we compare the model kinematics with those measured in hovering hawkmoths (Fig. 9). The model moth has a roll amplitude θ_0 of 37°, which is similar to the wing roll angle of 41° reported in the hawkmoth *Agrius convolvuli* during tethered flight ([52]). Other studies show a larger roll amplitude closer to 50° in *M. sexta* ([48]). However, observations of *M. sexta* during hovering flight indicate a distinct upstroke and downstroke with different kinematics ([48,55]), whereas this trend is not recapitulated by the mathematical model. We hypothesize this is because we have constrained the thorax force to be purely harmonic. In real moths, the dorsolongitudinal muscle is used to depress the thorax and generate the downstroke ([53]). The dorsolongitudinal muscle group is the largest muscle in the body at $5-8\%$ of the total mass ([53]) and is believed to be significantly more powerful than the dorsoventral muscle ([56]). We expect this muscle anatomy generates an asymmetric forcing on the thorax, and thus an asymmetric wing stroke. Additionally, the wings of many insects exhibit some degree of camber. Experimental and computational work has shown that camber does not greatly impact the net aerodynamic forces over a rigid model insect wing rotating at constant velocity ([57,58]). However, as the force largely acts normal to the local wing surface, positive wing camber will typically result in greater lift and lower drag, as the leading-edge of the wing is more vertical-facing than in flat or negatively-cambered wings, and also experiences the highest pressure. Camber may also impact the flexibility and deformation of insect wings ([59,60]). Due to these factors, significantly more lift is produced on the downstroke than during the upstroke ([61]), and the asymmetry of lift over a wingbeat may affect stroke kinematics.

The model moth has wing pitching amplitude near that of a hovering hawkmoth, measured near the wing tip (Fig. 9b). A flexible wing, such as in a real moth, experiences twist along the span, changing the apparent pitch angle based on location and aerodynamic loads. Our model assumes a rigid wing and thus cannot capture variable pitch over the length of the wing. Moreover, as with the roll angle, asymmetrical pitch over the wing stroke in *M. sexta* is not reproduced in our results due to symmetric loads and geometry.

Despite the limitations in this implementation, the model produces results that agree reasonably well with data previously obtained for the hawkmoth. Certain changes, especially regarding the fore-aft symmetry of the applied load and the wing geometry, could be made to more closely mimic real insect flight.

2. Multimodal Excitation

The lift/thrust generated by flapping wings is highly dependent on the phase relation between pitch and roll ([5,62]). As seen in Fig. 6, there is strong relationship between the roll-pitch phase $\beta_{\theta,\phi}$, and aerodynamic dissipation and overall efficiency. We now explore how advantageous phasing of kinematics is achieved within the flight system, which we hypothesize stems from excitation of two vibration modes.

In the absence of active pitch control, the system relies on inertial and aerodynamic loading to pitch the wing. A significant body of work points to resonance being an important phenomenon in flapping-wing insect flight ([19]), but more recent studies have suggested that moths may not be flapping *at* resonance, but post resonance ([54]). However, given that the flight system may be viewed as a multiple-degree-of-freedom system, it may have multiple resonant frequencies; it is unclear which resonant frequency the moth is flapping at or above. When the frequency of a load acting on a system is near the resonant frequency of one of the system's modes, the response of that mode will be magnified. Excitation between two resonant frequencies will elicit a response to which two vibration modes contribute. We note that these arguments do not scale identically to a strongly nonlinear system such as the insect flight system, but can provide at least some guiding insights into its dynamics.

In the system-level model presented, two modes are present. Each mode has a corresponding natural frequency and relative pitch and roll deflections. Individually, the system's first and second linear modes can only produce pitch-roll phases of -180° or 0°, respectively. Therefore, exciting both modes in unison is necessary to produce the desired $\beta_{\theta,\phi}$, phase through inertial loading. Producing advantageous phases closer to -90° therefore requires the simultaneous excitation of both modes. This was explored in ([62]), in which a test platform was built to generate large flapping and twisting motion by flapping between resonances.

From Fig. 10, the bulk of the optimized solutions have first natural frequencies above the flapping frequency, which initially seems to contradict the hypothesis that multimodal excitation is a significant factor. However, as seen in the frequency response (Fig. 7), the nonlinear resonant frequencies are significantly lower than the values predicted by the linearized system. There are multiple causes of this, particularly aerodynamic damping and added mass. As mentioned previously, in both the 'common' and 'worst' moths, the first and second nonlinear resonant frequencies were approximately 66% and 44% of their respective linear natural frequencies. The 'common'

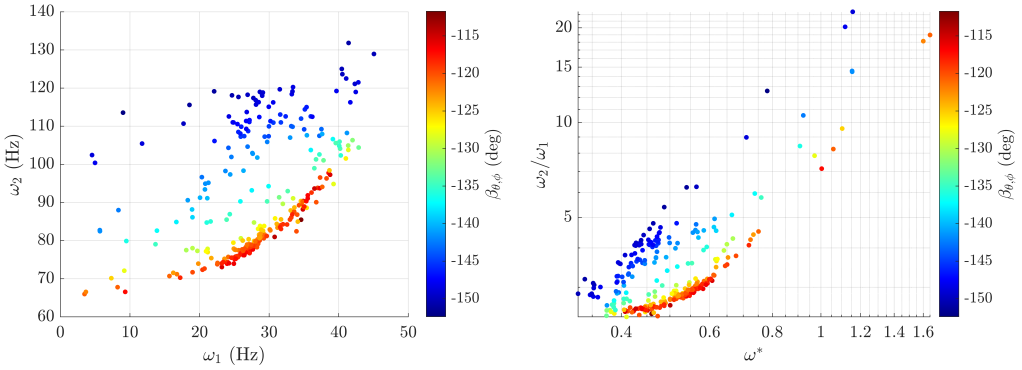


FIG. 10. Roll-pitch phase as a function of the linear natural frequencies (left) and natural frequency ratio and flapping frequency ratio (right). Each dot is a member of the population discussed in section III

moth has a mean nonlinear resonant frequency Ω_m that is nearly equal to the flapping frequency. In Fig. 10, the population subsection that has more favorable $\beta_{\theta,\phi}$ is centered roughly around $\omega^* = 0.5$, whereas the less-efficient solutions have lower ω^* on average. Extrapolating these findings to the population, this suggests that the most successful moths are flapping close to their mean nonlinear resonant frequency, well-placed for multimodal excitation. Furthermore, we see that the efficient moths have lower ω_2/ω_1 ratios, meaning their natural frequencies are closer together. A smaller gap between resonant frequencies should allow greater multimodal excitation when flapping at the mean resonant frequency, producing larger pitch and roll amplitudes.

The moth configuration produced through the genetic algorithm, particularly those that more efficiently produce lift, rely on multimodal excitation to generate advantageous flapping kinematics through inertial loading. By having an optimized phase relation between roll and pitch, aerodynamic losses due to drag are minimized, reducing the required energy expenditure by the moth. This multimodal excitation is achieved by applying a force on the thorax at a frequency between the two resonant peaks. Using inertial loads to passively generate the desired wing motion reduces the reliance on active pitch control by the moth. Inclusion of an active control moment about the pitch axis could be used to improve robustness to disturbance and for active control, as is the case in *M. sexta* ([63]).

3. Energy Recycling

A primary benefit of the system-level modeling approach is that elastic energy recycling via the thorax does not require special consideration. Instead, it is inherently accounted for by the thorax spring, permitting more accurate estimates of the overall energy expenditure. The mechanical power required by insect flight is typically estimated by using aerodynamic and wing inertial loading to calculate the appropriate power components ([38,64]). Previous studies apply limiting assumptions in estimating the energetic expenditures of flying insects. For example, negative work is 'recycled' at some efficiency, typically assumed to be either perfectly efficient, or fully inefficient, i.e., no recycling. Under the perfect efficiency assumption, negative work is added as-is to the positive work, resulting in the lowest possible power requirement. Conversely, when the recycling is treated as fully inefficient, the negative work is rectified and added to the positive work. Using this model, we can relax these assumptions, as energy recycling is intrinsically considered withing modeling efforts.

Work by Willmott et al. ([38]) placed the positive mechanical power for hovering flight between 23.06 and 30.22 W/kg for one female hawkmoth, assuming perfect elastic storage and zero elastic storage, respectively. Mao et al. estimated the mechanical power to between 33 and 42 W/kg ([64]). The first value assumes that negative power is dissipated without impacting energy requirements, and the second assumes negative power is elastically recycled. In contrast, our 'common' moth requires approximately 58.5 W/kg to hover. The discrepancy is likely in part due to differences in wing geometry and aerodynamic modeling.

4. FWMAV Design

Our study can inform the design and optimization of insect-inspired flapping wing micro air vehicles. Matching the timing of the applied load and the thorax response allows system elasticity to reduce the overall power consumption through energy recycling. Multimodal excitation can be utilized to generate flapping kinematics favorable to energetic efficiency in hovering flight. This is achieved by flapping at a frequency between resonant peaks. For the configuration here, a mean linear natural frequency approximately double the flapping frequency produced efficient solutions. If the relationship between nonlinear resonant and linear natural frequencies is known, the performance can be roughly estimated before simulation, reducing the effort required for optimization

studies. Additionally, bringing the linear natural frequencies closer together may make it easier to activate both modes, further decreasing the power cost of flight.

The reduced-order methods in the SLM allow fast solution evaluation while maintaining acceptable accuracy. Further modifications to the SLM could be made, such as series wing-hinge flexibility or delayed stretch activation, to better model certain insect species. Improvements to the aerodynamic modeling could be made, e.g., full 3D implementation, though at a computational cost. When coupled with an effective optimization scheme, a wide variety of configurations can be rapidly tested and iterated upon. Over the course of the 300 individual optimizations run, a total of just over a quarter-million moth configurations were tested, requiring roughly 36 hours. The computer used had a Intel i7-13700K 3.4 GHz 16-core CPU and 64 GB of DDR5 RAM. Using high fidelity modeling, a single moth simulation is estimated to take roughly 30 hours on a comparable machine, and therefore the full GA optimization set could require many thousands of years. While there are limitations to the reduced-order modeling, it has potential to be a powerful design tool for FWMAVs moving forward.

FUNDING

This research was supported the National Science Foundation under awards Nos. CBET-1855383 and CMMI-1942810 to MJ. Any opinions, findings, and conclusions or recommendations expressed in this material are those of the author(s) and do not necessarily reflect the views of the National Science Foundation.

DATA AVAILABILITY

The data that support the findings of this study are available from the corresponding author upon reasonable request.

REFERENCES

[1] S. Abdullah, P. Appari, S. R. Patri, and S. Katkoori, "Smart agriculture using flapping-wing micro aerial vehicles (fwmavs)," in *IFIP International Internet of Things Conference* (Springer, 2021) pp. 32–47.

[2]Y. Chen and Y. Li, "Intelligent autonomous pollination for future farming-a micro air vehicle conceptual framework with artificial intelligence and human-in-the-loop," IEEE Access **7**, 119706–119717 (2019).

[3]S. Xiao, K. Hu, B. Huang, H. Deng, and X. Ding, "A review of research on the mechanical design of hoverable flapping wing micro-air vehicles," Journal of Bionic Engineering **18**, 1235–1254 (2021).

[4]C. P. Ellington, C. Van Den Berg, A. P. Willmott, and A. L. Thomas, "Leading-edge vortices in insect flight," Nature **384**, 626–630 (1996).

[5]M. H. Dickinson, F.-O. Lehmann, and S. P. Sane, "Wing rotation and the aerodynamic basis of insect flight," science **284**, 1954–1960 (1999).

[6]D. R. Warrick, B. W. Tobalske, and D. R. Powers, "Aerodynamics of the hovering hummingbird," Nature **435**, 1094–1097 (2005).

[7]L. W. Traub and C. Coffman, "Efficient low-reynolds-number airfoils," Journal of Aircraft **56**, 1987–2003 (2019).

[8]J. Winslow, H. Otsuka, B. Govindarajan, and I. Chopra, "Basic understanding of airfoil characteristics at low reynolds numbers (10 4–10 5)," Journal of aircraft **55**, 1050–1061 (2018).

[9]H. J. Peters, J. F. Goosen, and F. van Keulen, "Optimal fwmav wing design for a combination of energy-effective hovering and roll control," International Journal of Micro Air Vehicles **7**, 41–53 (2015).

[10]M. H. Dickinson and M. S. Tu, "The function of dipteran flight muscle," Comparative Biochemistry and Physiology Part A: Physiology **116**, 223–238 (1997).

[11]J. Fernandes, M. Bate, and K. Vijayraghavan, "Development of the indirect flight muscles of drosophila," Development **113**, 67–77 (1991).

[12]M. Kobayashi and H. Ishikawa, "Breakdown of indirect flight muscles of alate aphids (acyrthosiphon pisum) in relation to their flight, feeding and reproductive behavior," Journal of Insect Physiology **39**, 549–554 (1993).

[13]M. Jankauski, C. Casey, C. Heveran, M. K. Busby, and S. Buchmann, "Carpenter bee thorax vibration and force generation inform pollen release mechanisms during floral buzzing," Scientific Reports **12**, 12654 (2022).

[14]M. Jankauski, R. Ferguson, A. Russell, and S. Buchmann, "Structural dynamics of real and modelled solanum stamens: implications for pollen ejection by buzzing bees," Journal of the Royal Society Interface **19**, 20220040 (2022).

[15]C. Casey, C. Heveran, and M. Jankauski, "Experimental studies suggest differences in the distribution of thorax elasticity between insects with synchronous and asynchronous musculature," Journal of the Royal Society Interface **20**, 20230029 (2023).

[16]J. Pringle, "The excitation and contraction of the flight muscles of insects," The Journal of physiology **108**, 226 (1949).

[17]A. Hollenbeck and A. Palazotto, "Mechanical characterization of flight mechanism in the hawkmoth manduca sexta," Experimental Mechanics **53**, 1189–1199 (2013).

[18]J. Gau, N. Gravish, and S. Sponberg, "Indirect actuation reduces flight power requirements in manduca sexta via elastic energy exchange," Journal of the Royal Society Interface **16**, 20190543 (2019).

[19]M. A. Jankauski, "Measuring the frequency response of the honeybee thorax," Bioinspiration & Biomimetics **15**, 046002 (2020).

[20]W. Shyy and H. Liu, "Flapping wings and aerodynamic lift: the role of leading-edge vortices," AIAA journal **45**, 2817–2819 (2007).

[21]Z. Terze, V. Pandža, M. Andrić, and D. Zlatar, "Reduced coupled flapping wing-fluid computational model with unsteady vortex wake," Nonlinear dynamics **109**, 975–987 (2022).

[22]T. Fitzgerald, M. Valdez, M. Vanella, E. Balaras, and B. Balachandran, "Flexible flapping systems: Computational investigations into fluid-structure interactions," The Aeronautical Journal **115**, 593–604 (2011).

[23]W. Johns, L. Davis, and M. Jankauski, "Reconstructing full-field flapping wing dynamics from sparse measurements," Bioinspiration & Biomimetics **16**, 016005 (2020).

[24]R. K. Schwab, H. E. Reid, and M. Jankauski, "Reduced-order modeling and experimental studies of bilaterally coupled fluid–structure interaction in single-degree-of-freedom flapping wings," Journal of Vibration and Acoustics **142**, 021012 (2020).

[25]M. Jankauski and I. Shen, "Dynamic modeling of an insect wing subject to three-dimensional rotation," International Journal of Micro Air Vehicles **6**, 231–251 (2014).

[26]B. A. Roccia, S. Preidikman, J. C. Massa, and D. T. Mook, "Modified unsteady vortex-lattice method to study flapping wings in hover flight," AIAA journal **51**, 2628–2642 (2013).

[27]B. A. Roccia, S. Preidikman, and B. Balachandran, "Computational dynamics of flapping wings in hover flight: a co-simulation strategy," AIAA Journal **55**, 1806–1822 (2017).

[28]J. D. Eldredge and A. R. Jones, "Leading-edge vortices: mechanics and modeling," Annual Review of Fluid Mechanics **51**, 75–104 (2019).

[29]R. Schwab, E. Johnson, and M. Jankauski, "A novel fluid–structure interaction framework for flapping, flexible wings," Journal of Vibration and Acoustics **141**, 061002 (2019).

[30]C. P. Ellington, "The aerodynamics of hovering insect flight. iv. aerodynamic mechanisms," Philosophical Transactions of the Royal Society of London. B, Biological Sciences **305**, 79–113 (1984).

[31]F.-O. Lehmann, "The mechanisms of lift enhancement in insect flight," Naturwissenschaften **91**, 101–122 (2004).

[32]L. A. Miller and C. S. Peskin, "Flexible clap and fling in tiny insect flight," Journal of Experimental Biology **212**, 3076–3090 (2009).

[33]R. Srygley and A. Thomas, "Unconventional lift-generating mechanisms in free-flying butterflies," Nature **420**, 660–664 (2002).

[34]A. P. Willmott, C. P. Ellington, and A. L. Thomas, "Flow visualization and unsteady aerodynamics in the flight of the hawkmoth, manduca sexta," Philosophical Transactions of the Royal Society of London. Series B: Biological Sciences **352**, 303–316 (1997).

[35]J. Lynch, J. Gau, S. Sponberg, and N. Gravish, "Dimensional analysis of spring-wing systems reveals performance metrics for resonant flapping-wing flight," Journal of the Royal Society Interface **18**, 20200888 (2021).

[36]A. Pons and T. Beatus, "Distinct forms of resonant optimality within insect indirect flight motors," Journal of The Royal Society Interface **19**, 20220080 (2022).

[37]B. Cote, S. Weston, and M. Jankauski, "Modeling and analysis of a simple flexible wing—thorax system in flapping-wing insects," Biomimetics **7**, 207 (2022).

[38]A. P. Willmott and C. P. Ellington, "The mechanics of flight in the hawkmoth manduca sexta ii. aerodynamic consequences of kinematic and morphological variation," Journal of Experimental Biology **200**, 2723–2745 (1997).

[39]J. Reade and M. Jankauski, "Investigation of chordwise functionally graded flexural rigidity in flapping wings using a two-dimensional pitch–plunge model," Bioinspiration & Biomimetics **17**, 066007 (2022).

[40]A. J. Bergou, S. Xu, and Z. J. Wang, "Passive wing pitch reversal in insect flight," Journal of Fluid Mechanics **591**, 321–337 (2007).

[41]R. Schwab, J. Reade, and M. Jankauski, "Quasi three-dimensional deformable blade element and unsteady vortex lattice reduced-order modeling of fluid–structure interaction in flapping wings," Physics of Fluids **34** (2022).

[42]J. Katz and A. Plotkin, *Low-speed aerodynamics*, Vol. 13 (Cambridge university press, 2001).

[43]L. N. Long and T. E. Fritz, "Object-oriented unsteady vortex lattice method for flapping flight," Journal of Aircraft **41**, 1275–1290 (2004).

[44]T. Faure, K. Roncin, B. Viaud, T. Simonet, and L. Daridon, "Flapping wing propulsion: Comparison between discrete vortex method and other models," Physics of Fluids **34** (2022).

[45]A. T. Nguyen, J.-K. Kim, J.-S. Han, and J.-H. Han, "Extended unsteady vortex-lattice method for insect flapping wings," Journal of Aircraft **53**, 1709–1718 (2016).

[46]T. Lambert, "Modeling of aerodynamic forces in flapping flight with the unsteady vortex lattice method," (2015).

[47]S. A. Combes and T. L. Daniel, "Flexural stiffness in insect wings i. scaling and the influence of wing venation," Journal of experimental biology **206**, 2979–2987 (2003).

[48]A. P. Willmott and C. P. Ellington, "The mechanics of flight in the hawkmoth manduca sexta i. kinematics of hovering and forward flight," Journal of experimental Biology **200**, 2705–2722 (1997).

[49]J. H. Holland, "Genetic algorithms," Scientific american **267**, 66–73 (1992).

[50]A. Lambora, K. Gupta, and K. Chopra, "Genetic algorithm-a literature review," in *2019 international conference on machine learning, big data, cloud and parallel computing (COMITCon)* (IEEE, 2019) pp. 380–384.

[51]M. Hellwig and H.-G. Beyer, "Benchmarking evolutionary algorithms for single objective real-valued constrained optimization–a critical review," Swarm and evolutionary computation **44**, 927–944 (2019).

[52]N. Ando and R. Kanzaki, "Flexibility and control of thorax deformation during hawkmoth flight," Biology letters **12**, 20150733 (2016).

[53]M. S. Tu and T. L. Daniel, "Submaximal power output from the dorsolongitudinal flight muscles of the hawkmoth manduca sexta," Journal of Experimental Biology **207**, 4651–4662 (2004).

[54]J. Gau, E. S. Wold, J. Lynch, N. Gravish, and S. Sponberg, "The hawkmoth wingbeat is not at resonance," Biology Letters **18**, 20220063 (2022).

[55]L. Zheng, T. L. Hedrick, and R. Mittal, "A multi-fidelity modelling approach for evaluation and optimization of wing stroke aerodynamics in flapping flight," Journal of Fluid Mechanics **721**, 118–154 (2013).

[56]B. Cranston and A. Palazotto, "Evaluation of the thorax of manduca sexta for flapping wing micro air vehicle applications," International Journal of Micro Air Vehicles **6**, 191–210 (2014).

[57]J. R. Usherwood and C. P. Ellington, "The aerodynamics of revolving wings i. model hawkmoth wings," Journal of Experimental biology **205**, 1547–1564 (2002).

[58]R. R. Harbig, J. Sheridan, and M. C. Thompson, "Relationship between aerodynamic forces, flow structures and wing camber for rotating insect wing planforms," Journal of Fluid Mechanics **730**, 52–75 (2013).

[59]A. Ennos, "Mechanical behaviour in torsion of insect wings, blades of grass and other cambered structures," Proceedings of the Royal Society of London. Series B: Biological Sciences **259**, 15–18 (1995).

[60]S. A. Combes and T. Daniel, "Flexural stiffness in insect wings ii. spatial distribution and dynamic wing bending," Journal of Experimental Biology **206**, 2989–2997 (2003).

[61]S. Lionetti, T. L. Hedrick, and C. Li, "Aerodynamic explanation of flight speed limits in hawkmoth-like flapping-wing insects," Physical Review Fluids **7**, 093104 (2022).

[62]D. Faux, O. Thomas, E. Cattan, and S. Grondel, "Two modes resonant combined motion for insect wings kinematics reproduction and lift generation," Europhysics Letters **121**, 66001 (2018).

[63]S. A. Combes and T. L. Daniel, "Into thin air: contributions of aerodynamic and inertial-elastic forces to wing bending in the hawkmoth manduca sexta," Journal of Experimental Biology **206**, 2999–3006 (2003).

[64]S. Mao and D. Gang, "Lift and power requirements of hovering insect flight," Acta Mechanica Sinica **19**, 458–469 (2003).

[65]A. E. Eiben and J. E. Smith, *Introduction to evolutionary computing* (Springer, 2015).

[66]M. De la Maza and B. Tidor, "Boltzmannn weighted selection improves performance of genetic algorithms," (1991).

[67]M. Obitko, "Introduction to genetic algorithms," Czech Technical University: Prague, Czech Republic (1998).

[68]A. Hassanat, K. Almohammadi, E. Alkafaween, E. Abunawas, A. Hammouri, and V. S. Prasath, "Choosing mutation and crossover ratios for genetic algorithms—a review with a new dynamic approach," Information **10**, 390 (2019).

Appendix A: Unsteady Vortex Lattice Method

In this appendix, the quasi-3D UVLM solver is described in greater detail. The rectangular wing is divided spanwise into multiple blades, each of which runs from the leading edge of the

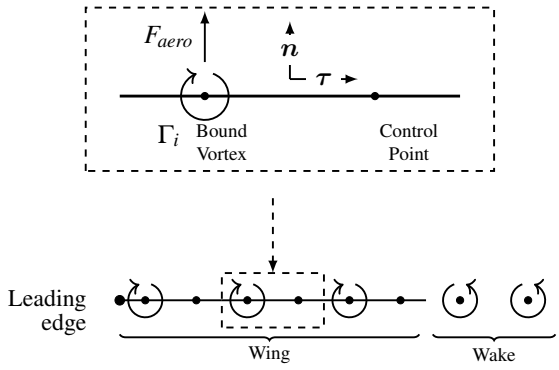


FIG. 11. Discretization of a blade into panels. Top section shows bound vortex and control point placement on a panel

wing to the trailing edge. The aerodynamics of each blade are solved individually using a two-dimensional UVLM method. Each blade is divided chordwise into panels, and on each panel a bound vortex is placed at the quarter-chord and a control point at the three-quarters-chord (Fig. 11).

Time-dependent effects are modeled via the inclusion of wake shedding, where wake vortices are generated at the trailing edge of the wing and convected with the flow. Each point vortex generates an induced tangential velocity field around itself, with magnitude proportional to vortex and inversely proportional to separation. The velocity at a point i induced by a vortex j is given by the Biot-Savart law

$$\boldsymbol{V}_{i,j} = \frac{\Gamma_j}{2\pi} \frac{(r_{i,z} - r_{j,z})\mathbf{e}_x + (r_{j,x} - r_{i,x})\mathbf{e}_z}{|\boldsymbol{r_i} - \boldsymbol{r_j}|^2} \tag{A1}$$

where $V_{i,j}$ is velocity at position r_i induced by a vortex at position r_j that has strength Γ_j. While adequate for larger separations, this equation results in unreasonably high velocity when the vortex is close to the point if interest. To remedy this, we introduce a cutoff radius r_{co}. Outside of this radius, the induced velocity is as above. When the separation between the vortex and the point of interest is less than r_{co}, however, the induced velocity decreases linearly as separation decreases. Equation A1 becomes

$$\begin{aligned} \boldsymbol{V}_{i,j} &= \frac{\Gamma_j}{2\pi}\frac{(r_{i,z}-r_{j,z})\mathbf{e}_x+(r_{j,x}-r_{i,x})\mathbf{e}_z}{|\boldsymbol{r_i}-\boldsymbol{r_j}|^2};\ |\boldsymbol{r_i}-\boldsymbol{r_j}|>r_{co} \\ \boldsymbol{V}_{i,j} &= \frac{\Gamma_j}{2\pi}\frac{(r_{i,z}-r_{j,z})\mathbf{e}_x+(r_{j,x}-r_{i,x})\mathbf{e}_z}{r_{co}^2};\ |\boldsymbol{r_i}-\boldsymbol{r_j}|\leq r_{co} \end{aligned} \tag{A2}$$

The cutoff radius can be imagined as the radius of the vortex core, and the vorticity is uniformly distributed throughout this core.

Initially unknown, the strengths of the bound vortices are determined by enforcing the non-penetration boundary condition. At the surface of the wing, the fluid flow normal to that surface must be zero. We also calculate the strength of the newly-shed trailing-edge wake vortex via the Kelvin-Helmholtz condition, stating that the total vorticity in the inviscid fluid must remain constant over time. When the non-penetration condition is enforced at the control points of each panel, these conditions become

$$\begin{bmatrix} a_{1,1} & a_{1,2} & \cdots & a_{1,N_p} & a_{1,N_p+1} \\ a_{2,1} & a_{2,2} & \cdots & a_{2,N_p} & a_{2,N_p+1} \\ \vdots & \vdots & \ddots & \vdots & \vdots \\ a_{N_p,1} & a_{N_p,2} & \cdots & a_{N_p,N_p} & a_{N_p,N_p+1} \\ 1 & 1 & \cdots & 1 & 1 \end{bmatrix} \begin{Bmatrix} \Gamma_1 \\ \Gamma_2 \\ \vdots \\ \Gamma_{N_p} \\ \Gamma_{W_1} \end{Bmatrix} = \begin{Bmatrix} rhs_1 \\ rhs_2 \\ \vdots \\ rhs_{N_p} \\ rhs* \end{Bmatrix} \tag{A3}$$

where $a_{i,j}$ is the aerodynamic influence coefficient, or velocity induced at control point i, normal to the wing surface, by either the bound vortex on panel j ($j = 1...N_p$), or the newly shed wake vortex ($j = N_{p+1}$), assuming unit-strength. N_p is the total number of panels on the blade, and N_p+1 indicates the newly-shed trailing-edge vortex. rhs_i is the surface-normal velocity at control point i due to rigid-body kinematics and wake-induced velocity. rhs^* is the total bound vorticity on the wing from the previous time step. Γ_i is the new bound vortex strength of the i^{th} panel, and Γ_{W_1} is the new wake vortex strength.

Once the bound vorticity is known, the pressure over the wing surface is calculated using the unsteady Bernoulli equation

$$\Delta p_i = -\rho_f \left[(-\dot{\boldsymbol{R}}_{\boldsymbol{i}} + \boldsymbol{V}_{ind,i}) \cdot \boldsymbol{\tau}_i \frac{\Gamma_i}{ds} + \frac{\partial}{\partial t} \sum_{j=1}^{i} \Gamma_j \right] \tag{A4}$$

where Δp_i is the total pressure acting on the i^{th} panel, ρ_f is the fluid density, $\dot{\boldsymbol{R}}_{\boldsymbol{i}}$ is the motion of the i^{th} panel in the global reference frame, $\boldsymbol{V}_{ind,i}$ is the total wake-induced velocity on the panel,

τ is the panel surface-tangent vector, and ds is the panel length. The time-dependent summation term estimates the unsteady added mass force, and the summation is from the leading-edge to the i^{th} panel. The pressure is assumed to act normal to the panel. As the wing is a rigid flat plate and viscous forces are neglected, the total aerodynamic force is always normal to the wing.

Wake vortices are modeled as massless, meaning they perfectly follow the local flow velocity. The velocity of a wake vortex is determined by summing the velocity induced at its position by all other bound and wake vortices. From there a simple forward-difference Euler update is used to estimate the new wake positions in space. Once these steps have been completed, the aerodynamic pressures are converted into moments about the pitch and roll axes (Eqs. 10 - 11), and fed into the system equations of motion (Eqs. 8 - 9) as applied loads.

Appendix B: Genetic Algorithm

In this section we discuss the implementation of the genetic algorithm technique, starting with how the population is ranked, and followed by the process through which the new generation is created from the current population.

Candidate solutions are ranked according to desirability. Between any two solutions, any feasible ($CV = 0$) solution is preferred over any infeasible ($CV > 0$) solution. If both solutions are feasible, then the individual that has the better objective function value (OFV) is preferable. Finally, if both solutions are infeasible, than the individual that is nearest to being feasible, i.e. the lowest CV, is preferred over that with the greater CV. From this rule set, every individual has a ranking R_i, ranging from $R_i = 1$ for the best solution and $R_i = N$ for the least desirable solution.

From here, each solutions is assigned a selection probability μ_{select}. This determines the likelihood of a solution being chosen for recombination, described below. We use linear rank selection in this implementation, slightly modified from that described in ([65]). Selection probability is dependent only on the ranked position of the individual, and not directly on the actual objective function or constraint violation values. The selection probability for an individual is given by

$$\mu_{select,i} = \frac{1}{N}\left(\eta - (2\eta - 2)\frac{R_i - 1}{N - 1}\right) \tag{B1}$$

where η is the selection pressure parameter, controlling how competitive selection is. When $\eta = 1$, there is no dependence on rank R_i when selection pressures are assigned, and every individual has equal selection pressure, i.e. $\mu_{select} = 1/N$. At $\eta = 2$, the best individual has double the median selection probability, and the worst-ranked solution has $\mu_{select} = 0$.

Low selection pressure emphasizes exploration, and high selection pressure leans more into exploitation. The implementation here uses a form of Boltzmann weighted selection ([66]), where the selection pressure is increased over the course of the optimization In our implementation of the GA algorithm, we start the optimization using a mid-range selection pressure, $\eta = 1.5$. With this pressure, the middle-ranked and best-ranked individuals were two and three times as likely to be chosen as the worst-ranked, respectively. This exhibits a preference for the better-performing individuals, but still allows the worse solutions to evolve, so that the parameter space is more broadly explored. After some number of generations have been passed, the selection pressure is increased to $\eta = 2$. This shifts the focus off of exploration and onto exploitation, so that the best existing solutions are optimized further.

For each offspring formed by recombination, two solutions from the current population are randomly chosen. The initial probability that an individual will be selected as a specific parent is equal to its selection probability $\mu_{select,i}$. If the same solution is selected as both parents, then the second parent is re-selected using the same set of selection probabilities. The offspring's chromosome is randomly determined based on those of the parents.

Offspring created via recombination are then acted on by the mutation operator. Mutation is used to explore potential solutions that exist outside the current population. In an individual chromosome, every gene has a fixed independent chance to be mutated, ξ. When a gene is mutated, it is given a new value at random from a Gaussian distribution, centered on the current gene value. The Gaussian distribution is used so that small mutations are more likely than large mutations. We set the standard deviation for each gene to initially be one-sixth of the allowable range for the parameter. After a set number of generations, the standard deviation of the distribution is reduced, so that the magnitude of the mutations is much smaller. This better allows the method to make smaller adjustments to existing solutions, since it is assumed that solutions are closer to optimal at this point in the optimization. Increased ξ prevents the search from too easily settling into a local optimum. If the probability is too large, and the deviation is significant, the optimization becomes more of a random search ([67,68])

Due to the randomness inherent in this process, it is possible for a population to perform worse than did the previous generation, degrading the solution. To address this problem, we utilize elitism, wherein the N_{elite} best-ranked solutions in a population are carried over into the next generation, unaltered by mutation or recombination. This ensures that the best solution in a generation is always at least as fit as that in the previous generation. Generally, N_{elite} is kept to a relatively

TABLE VII. **Genetic algorithm parameters**

Quantity	Value
Number of Generations	30
Population Size	28
Mutation Probability	30%
Selection Pressure (initial)	1.5
Selection Pressure (final)	2

small number compared to the total population size. Because the elites will hive the highest selection probability and are available as parents in the recombination step, a larger N_{elite} can lead to low population diversity and early convergence on a local optimum. In addition to elitism, we use parthenogenesis to advance the best solutions. Here, copies are made of the elites and then mutated, producing similar but not identical offspring. This enforces some minimum level of focus on exploitation, so that even when selection pressure is low there is some effort dedicated to optimization of the current best solution via small tweaks. When the objective space is complex or when near an optimum, this may more reliably progress the solution.

Once a new generation has been formed through the process described above, the individuals in it are simulated using the described system level model, and the process repeats until some termination criteria is met.

CONCLUSION

Flapping wings enable insects to fly with high maneuverability and efficiency at the centimeter and millimeter scales, utilizing unsteady aerodynamic phenomena. These benefits make flapping-wing micro air vehicles (FMWAVs) attractive options for tasks where maneuverability and compactness are important, such as in collapsed buildings or in dense flora. Distributed sensing applications would also benefit from the reduced per-unit cost of these UAVs. The enhanced capability at low Reynolds numbers would allow FWMAVs to operate in low-density atmospheres where a conventional aircraft would underperform. Understanding the effects of wing flexibility on aerodynamics and performance is key to the further development of FWMAVs. Careful tuning of flexibility can result in greater lift at lower energetic cost compared to a rigid wing, while also allowing for a lighter structure. Development of FWMAVs is impeded by technological limitations and an incomplete understanding of the aerodynamics and fluid-structure interaction surrounding flexible flapping wings. The unsteady, complex airflow and fast multiple-degree-of-freedom rotations make them difficult to study, both experimentally and computationally. Physical study using insects is made difficult by all the uncertainties and confounding variables inherent to complex biological systems. Testing with artificial systems faces obstacles from the high-speed, high-amplitude rotations and flexible structure. Aerodynamic forces on the wing must be separated from the inertial loads of the system, which may be difficult when testing flexible wings. Computational study faces different challenges. Computational fluid dynamics (CFD) and finite element analysis (FEA) are often considered the standard of accuracy in numerical fluid methods, and are used to study complex problems over multiple flow regimes. The high potential fidelity comes at the cost of highly resource-intensive simulations that often require highly refined discretization and are slow to reach solutions. This makes them infeasible for use in broader studies where multiple configurations of

a problem must be tested. For this reason, high-fidelity methods are often replaced or augmented by reduced-order models (ROMs).

By considering only the most salient physics, ROMs can produce a solution in a small fraction of the time required by high-fidelity methods, at the cost of accuracy and generalizability. The rapid solution iteration, which may be several orders of magnitude faster, make them highly suited to tasks such as parametric or optimization studies, often an important early step in the design process. Furthermore, as they typically place a reduced load on system resources, reduced-order models are often able to be heavily parallelized on standard computer systems, amplifying the already-significant speed-up over conventional CFD and FEA when performing these studies. Given that reduced-order models function by neglecting the physics considered to be unimportant, they require a greater prior understanding of the phenomena present than do high-fidelity methods. Development of reduced-order models is aided by high-fidelity methods by allowing the identification of physical mechanisms, such as the leading-edge vortex (LEV) over the wing. In turn, these phenomena may be added or subtracted from reduced-order models depending on the desired computational fidelity, and the effects of the phenomena may be quantified more readily than is possible using CFD. High-fidelity methods and reduced-order modeling are complimentary in the development of FWMAVs. ROMs can be used to explore broad design spaces and identify parametric relationships, while high-fidelity models are used to investigate a restricted number of configurations and produce estimates with high certainty.

The research presented in this dissertation adds to the growing body of work investigating exploring flapping wing flight. The unsteady vortex lattice method (UVLM) fluid model developed and utilized in this research can estimate aerodynamic forces on flapping wings at very low computational cost. However, some components are neglected which may limit accuracy and applicability - namely, leading-edge vortex shedding and spanwise flow. The LEV is a prominent flow feature in flapping wing flight that influences

the pressure distribution. The LEV also carries a significant spanwise velocity component. While the current UVLM formulation accurately predicts net aerodynamic force, measured against high-fidelity methods, it cannot satisfactorily reproduce the pressure distribution over the wing. The pressure distribution is used to determine the aerodynamic moments acting on the wing, and is therefore a significant factor in wing deformation, aerodynamic power, and wing kinematics in the system-level model. Inclusion of the LEV and extension to true three-dimensional fluid flow would undoubtedly increase the potential accuracy of the ROM. However, this comes at increased computational cost. A full-3D UVLM would require significantly more calculations per time-step compared to the quasi-3d method due to spanwise interaction between panel and wake vortices. Tracking the motion and influence of the trailing-edge wake vortices is already a considerable resource burden in the quasi-3D method, and adding the LEV would exacerbate this. Ultimately, a computational study, comparing the quasi-3D UVLM method presented here to a modified method capable of true 3D flow and LEV shedding, would be valuable, to inform future work as to whether the added fidelity is worth the trade-off of increased cost and complexity.

The system-level model (SLM) described in chapter 5 may be further developed, to better reproduce the behaviour found in insect flight. In its current form the SLM is useful for examining elastic energy recycling in the thorax and how resonance may be used to improve performance. There are species of flying insect that are of great interest to researchers, but presently cannot be well-approximated by our SLM. Many smaller insects with high wingbeat frequencies have asynchronous flight muscles [Pringle, 1949; Josephson et al., 2000]. In these insects, the timing of each wingbeat does not correspond directly to one neural signal. Instead, once flapping is initiated, stretching of muscle fibers during flapping triggers an response to initiate another wingbeat. These insects also may have a more flexible wing hinge than synchronous fliers, so that the wing roll angle may not be considered directly linked to thorax deformation [Casey et al., 2023]. Modifying the SLM to allow the thorax muscle

force to be a function of kinematics and introducing a roll-stiffness element in series with the thorax would better enable the model to simulate a larger number of insect species and potential FWMAV designs. Many insects, particularly smaller species, use clap-and fling to enhance lift production [Miller and Peskin, 2009]. Modeling the entire insect including both the left and right wings, along with full 3D fluid modeling, would allow the SLM to account for aerodynamic forces generated from this mechanism. Furthermore, the applicability of the model would be improved, better allowing the SLM to simulate asymmetric aerial maneuvers and the response to external disturbances like wind gusts.

Reduced-order modeling allows for the effective and efficient study of flapping-wing flight and the aeroelastic behaviour that comes with wing flexibility. The short solution time lends itself to parametric studies where using high-fidelity modeling is impractical if not impossible. The modeling of various physical phenomena can be added or subtracted, trading speed for accuracy depending on the application. Reduced-order models, working cooperatively with high-fidelity models, will grow the body of knowledge surrounding flapping-wing flight and accelerate the advancement of flapping-wing micro air vehicles as a technology.

REFERENCES CITED

Abdullah, S., Appari, P., Patri, S. R., and Katkoori, S. (2021). Smart agriculture using flapping-wing micro aerial vehicles (fwmavs). In *IFIP International Internet of Things Conference*, pages 32–47. Springer.

Addo-Akoto, R., Han, J.-S., and Han, J.-H. (2021). Roles of wing flexibility and kinematics in flapping wing aerodynamics. *Journal of Fluids and Structures*, 104:103317.

Ahn, C. W. and Ramakrishna, R. S. (2003). Elitism-based compact genetic algorithms. *IEEE Transactions on Evolutionary Computation*, 7(4):367–385.

Aiello, B. R., Stanchak, K. E., Weber, A. I., Deora, T., Sponberg, S., and Brunton, B. W. (2021). Spatial distribution of campaniform sensilla mechanosensors on wings: form, function, and phylogeny. *Current Opinion in Insect Science*, 48:8–17.

Altshuler, D. L., Dickson, W. B., Vance, J. T., Roberts, S. P., and Dickinson, M. H. (2005). Short-amplitude high-frequency wing strokes determine the aerodynamics of honeybee flight. *Proceedings of the National Academy of Sciences*, 102(50):18213–18218.

Anderson, J. D. (2011). *Fundamentals of aerodynamics*. McGraw-Hill, 5th edition.

Anderson, J. D. and Wendt, J. (1995). *Computational fluid dynamics*, volume 206. Springer.

Ando, N. and Kanzaki, R. (2004). Changing motor patterns of the 3rd axillary muscle activities associated with longitudinal control in freely flying hawkmoths. *Zoological science*, 21(2):123–130.

Ando, N. and Kanzaki, R. (2016). Flexibility and control of thorax deformation during hawkmoth flight. *Biology letters*, 12(1):20150733.

Ando, N., Kono, T., Ogihara, N., Nakamura, S., Yokota, H., and Kanzaki, R. (2022). Modeling the musculoskeletal system of an insect thorax for flapping flight. *Bioinspiration & Biomimetics*, 17(6):066010.

Ashraf, M., Lai, J., and Young, J. (2007). Numerical analysis of flapping wing aerodynamics. In *16th Australasian Fluid Mechanics Conference*, pages 1283–1290.

Baumeister, T. and Sadegh, A. M. (1978). *Marks' standard handbook for mechanical engineers*, volume 1. McGraw-Hill New York.

Bazoune, A. and Khulief, Y. (1992). A finite beam element for vibration analysis of rotating tapered timoshenko beams. *Journal of Sound and Vibration*, 156(1):141–164.

Benra, F.-K., Dohmen, H. J., Pei, J., Schuster, S., and Wan, B. (2011). A comparison of one-way and two-way coupling methods for numerical analysis of fluid-structure interactions. *Journal of applied mathematics*, 2011.

Bergou, A. J., Xu, S., and Wang, Z. J. (2007). Passive wing pitch reversal in insect flight. *Journal of Fluid Mechanics*, 591:321–337.

Berman, G. J. and Wang, Z. J. (2007). Energy-minimizing kinematics in hovering insect flight. *Journal of Fluid Mechanics*, 582:153–168.

Birch, J. M. and Dickinson, M. H. (2001). Spanwise flow and the attachment of the leading-edge vortex on insect wings. *Nature*, 412(6848):729–733.

Bluman, J. E., Kang, C.-K., Landrum, D. B., Fahimi, F., and Mesmer, B. (2017). Marsbee-can a bee fly on mars? In *55th AIAA Aerospace Sciences Meeting*, page 0328.

Bode-Oke, A. T. and Dong, H. (2020). The reverse flight of a monarch butterfly (danaus plexippus) is characterized by a weight-supporting upstroke and postural changes. *Journal of the Royal Society Interface*, 17(167):20200268.

Burrows, M., Shaw, S. R., and Sutton, G. P. (2008). Resilin and chitinous cuticle form a composite structure for energy storage in jumping by froghopper insects. *BMC biology*, 6:1–16.

Casey, C., Heveran, C., and Jankauski, M. (2023). Experimental studies suggest differences in the distribution of thorax elasticity between insects with synchronous and asynchronous musculature. *Journal of the Royal Society Interface*, 20(201):20230029.

Casey, C., Yager, C., Jankauski, M., and Heveran, C. M. (2021). The flying insect thoracic cuticle is heterogenous in structure and in thickness-dependent modulus gradation. *bioRxiv*.

Chen, C. and Zhang, T. (2019). A review of design and fabrication of the bionic flapping wing micro air vehicles. *Micromachines*, 10(2):144.

Chen, Y. and Li, Y. (2019). Intelligent autonomous pollination for future farming-a micro air vehicle conceptual framework with artificial intelligence and human-in-the-loop. *IEEE Access*, 7:119706–119717.

Chimakurthi, S. K., Stanford, B. K., Cesnik, C. E., and Shyy, W. (2009a). Flapping wing cfd/csd aeroelastic formulation based on a co-rotational shell finite element. In *50th AIAA/ASME/ASCE/AHS/ASC Structures, Structural Dynamics, and Materials Conference 17th AIAA/ASME/AHS Adaptive Structures Conference 11th AIAA No*, page 2412.

Chimakurthi, S. K., Tang, J., Palacios, R., S. Cesnik, C. E., and Shyy, W. (2009b). Computational aeroelasticity framework for analyzing flapping wing micro air vehicles. *AIAA journal*, 47(8):1865–1878.

Combes, S. and Daniel, T. (2003a). Flexural stiffness in insect wings i. scaling and the influence of wing venation. *Journal of experimental biology*, 206(17):2979–2987.

Combes, S. and Daniel, T. (2003b). Flexural stiffness in insect wings ii. spatial distribution and dynamic wing bending. *Journal of Experimental Biology*, 206(17):2989–2997.

Combes, S. A. and Daniel, T. L. (2003c). Flexural stiffness in insect wings I. Scaling and the influence of wing venation. *Journal of Experimental Biology*, 206(17):2979–2987.

Combes, S. A. and Daniel, T. L. (2003d). Into thin air: contributions of aerodynamic and inertial-elastic forces to wing bending in the hawkmoth manduca sexta. *Journal of Experimental Biology*, 206(17):2999–3006.

Cote, B., Weston, S., and Jankauski, M. (2022). Modeling and analysis of a simple flexible wing—thorax system in flapping-wing insects. *Biomimetics*, 7(4):207.

Cranston, B. and Palazotto, A. (2014). Evaluation of the thorax of manduca sexta for flapping wing micro air vehicle applications. *International Journal of Micro Air Vehicles*, 6(3):191–210.

Cressman, K. (2016). Desert locust. *Biological and environmental hazards, risks, and disasters*, pages 87–105.

Dai, H., Luo, H., and Doyle, J. F. (2012). Dynamic pitching of an elastic rectangular wing in hovering motion. *Journal of Fluid Mechanics*, 693:473–499.

De la Maza, M. and Tidor, B. (1991). Boltzmannn weighted selection improves performance of genetic algorithms. Technical report, Massachusetts Institute of Technology.

Dickerson, B. H., Aldworth, Z. N., and Daniel, T. L. (2014). Control of moth flight posture is mediated by wing mechanosensory feedback. *Journal of Experimental Biology*, 217(13):2301–2308.

Dickerson, B. H., Fox, J. L., and Sponberg, S. (2021). Functional diversity from generic encoding in insect campaniform sensilla. *Current Opinion in Physiology*, 19:194–203.

Dickinson, M. H., Lehmann, F.-O., and Sane, S. P. (1999). Wing rotation and the aerodynamic basis of insect flight. *science*, 284(5422):1954–1960.

Dickinson, M. H. and Tu, M. S. (1997). The function of dipteran flight muscle. *Comparative Biochemistry and Physiology Part A: Physiology*, 116(3):223–238.

Dickson, W., Straw, A., Poelma, C., and Dickinson, M. (2006). An integrative model of insect flight control. In *44th AIAA Aerospace Sciences Meeting and Exhibit*, page 34.

Du, G. and Sun, M. (2010). Effects of wing deformation on aerodynamic forces in hovering hoverflies. *Journal of Experimental Biology*, 213(13):2273–2283.

Durbin, P. A. (2017). *Turbulence Closure Models for Computational Fluid Dynamics*, pages 1–22. John Wiley & Sons, Ltd.

Eberle, A., Dickerson, B., Reinhall, P., and Daniel, T. (2015). A new twist on gyroscopic sensing: body rotations lead to torsion in flapping, flexing insect wings. *Journal of the Royal Society Interface*, 12(104):20141088.

Edgerton, K., Throneberry, G., Takeshita, A., Hocut, C., Shu, F., and Abdelkefi, A. (2019). Numerical and experimental comparative performance analysis of emerging spherical-caged drones. *Aerospace Science and Technology*, 95:105512.

Eiben, A. E. and Smith, J. E. (2015). *Introduction to evolutionary computing*. Springer.

Eldredge, J. D. and Jones, A. R. (2019). Leading-edge vortices: mechanics and modeling. *Annual Review of Fluid Mechanics*, 51:75–104.

Ellington, C. P. (1984). The aerodynamics of flapping animal flight. *American Zoologist*, 24(1):95–105.

Ellington, C. P. (1999). The novel aerodynamics of insect flight: applications to micro-air vehicles. *Journal of Experimental Biology*, 202(23):3439–3448.

Ellington, C. P., Van Den Berg, C., Willmott, A. P., and Thomas, A. L. (1996). Leading-edge vortices in insect flight. *Nature*, 384(6610):626–630.

Elliott, S., Tehrani, M. G., and Langley, R. (2015). Nonlinear damping and quasi-linear modelling. *Philosophical Transactions of the Royal Society A: Mathematical, Physical and Engineering Sciences*, 373(2051):20140402.

Ennos, A. (1995). Mechanical behaviour in torsion of insect wings, blades of grass and other cambered structures. *Proceedings of the Royal Society of London. Series B: Biological Sciences*, 259(1354):15–18.

Farrell Helbling, E. and Wood, R. J. (2018). A review of propulsion, power, and control architectures for insect-scale flapping-wing vehicles. *Applied Mechanics Reviews*, 70(1).

Faure, T., Roncin, K., Viaud, B., Simonet, T., and Daridon, L. (2022). Flapping wing propulsion: Comparison between discrete vortex method and other models. *Physics of Fluids*, 34(3).

Faux, D., Thomas, O., Cattan, E., and Grondel, S. (2018). Two modes resonant combined motion for insect wings kinematics reproduction and lift generation. *Europhysics Letters*, 121(6):66001.

Fernandes, J., Bate, M., and Vijayraghavan, K. (1991). Development of the indirect flight muscles of drosophila. *Development*, 113(1):67–77.

Fernandez-Escudero, C., Gagnon, M., Laurendeau, E., Prothin, S., Michon, G., and Ross, A. (2019). Comparison of low, medium and high fidelity numerical methods for unsteady aerodynamics and nonlinear aeroelasticity. *Journal of Fluids and Structures*, 91:102744.

Fitzgerald, T. (2013). *Nonlinear fluid-structure interactions in flapping wing systems*. PhD thesis, University of Maryland, College Park.

Fitzgerald, T., Valdez, M., Vanella, M., Balaras, E., and Balachandran, B. (2011). Flexible flapping systems: Computational investigations into fluid-structure interactions. *The Aeronautical Journal*, 115(1172):593–604.

Fuller, S. B., Karpelson, M., Censi, A., Ma, K. Y., and Wood, R. J. (2014). Controlling free flight of a robotic fly using an onboard vision sensor inspired by insect ocelli. *Journal of The Royal Society Interface*, 11(97):20140281.

Gao, H., Zhu, J., Sun, C., Li, Z.-a., and Peng, Q. (2024). Visualized neural network-based vibration control for pigeon-like flexible flapping wings. *ISA transactions*.

Gau, J., Gravish, N., and Sponberg, S. (2019a). Indirect actuation reduces flight power requirements in manduca sexta via elastic energy exchange. *Journal of the Royal Society Interface*, 16(161):20190543.

Gau, J., Gravish, N., and Sponberg, S. (2019b). Indirect actuation reduces flight power requirements in manduca sexta via elastic energy exchange. *J. R. Soc. Interface*, 16(161).

Gau, J., Wold, E. S., Lynch, J., Gravish, N., and Sponberg, S. (2022). The hawkmoth wingbeat is not at resonance. *Biology Letters*, 18(5):20220063.

Geissler, W. and van der Wall, B. G. (2017). Dynamic stall control on flapping wing airfoils. *Aerospace Science and Technology*, 62:1–10.

Ghalamchi, B., Jia, Z., and Mueller, M. W. (2019). Real-time vibration-based propeller fault diagnosis for multicopters. *IEEE/ASME Transactions on Mechatronics*, 25(1):395–405.

Ghayesh, M. H., Farokhi, H., and Amabili, M. (2013). Nonlinear dynamics of a microscale beam based on the modified couple stress theory. *Composites Part B: Engineering*, 50:318–324.

Gilmanov, A., Le, T. B., and Sotiropoulos, F. (2015). A numerical approach for simulating fluid structure interaction of flexible thin shells undergoing arbitrarily large deformations in complex domains. *Journal of computational physics*, 300:814–843.

Gnatzy, W., Grunert, U., and Bender, M. (1987). Campaniform sensilla of calliphora vicina (insecta, diptera). *Zoomorphology*, 106:312–319.

Goldsworthy, G. J. and Wheeler, C. H. (1989). *Insect flight*. CRC Press Boca Raton, FL.

Gordnier, R. E., Chimakurthi, S. K., Cesnik, C. E., and Attar, P. J. (2013). High-fidelity aeroelastic computations of a flapping wing with spanwise flexibility. *Journal of Fluids and Structures*, 40:86–104.

Greeter, J. S. and Hedrick, T. L. (2016). Direct lateral maneuvers in hawkmoths. *Biology open*, 5(1):72–82.

Gresho, P. M. (1991). Some current cfd issues relevant to the incompressible navier-stokes equations. *Computer Methods in Applied Mechanics and Engineering*, 87(2-3):201–252.

Guariso, G. and Sangiorgio, M. (2020). Improving the performance of multiobjective genetic algorithms: An elitism-based approach. *Information*, 11(12):587.

Hadzic, H. (2006). Development and application of finite volume method for the computation of flows around moving bodies on unstructured, overlapping grids. *Ph.D. thesis, Technische Universität Hamburg, Hamburg*.

Hamamoto, M., Ohta, Y., Hara, K., and Hisada, T. (2007). Application of fluid–structure interaction analysis to flapping flight of insects with deformable wings. *Advanced Robotics*, 21(1-2):1–21.

Harbig, R. R., Sheridan, J., and Thompson, M. C. (2013). Relationship between aerodynamic forces, flow structures and wing camber for rotating insect wing planforms. *Journal of Fluid Mechanics*, 730:52.

Hassanat, A., Almohammadi, K., Alkafaween, E., Abunawas, E., Hammouri, A., and Prasath, V. S. (2019). Choosing mutation and crossover ratios for genetic algorithms—a review with a new dynamic approach. *Information*, 10(12):390.

Heathcote, S., Wang, Z., and Gursul, I. (2008). Effect of spanwise flexibility on flapping wing propulsion. *Journal of Fluids and Structures*, 24(2):183–199.

Hedrick, T. L. (2008). Software techniques for two-and three-dimensional kinematic measurements of biological and biomimetic systems. *Bioinspiration & biomimetics*, 3(3):034001.

Hedrick, T. L. and Daniel, T. (2006). Flight control in the hawkmoth manduca sexta: the inverse problem of hovering. *Journal of Experimental Biology*, 209(16):3114–3130.

Hellwig, M. and Beyer, H.-G. (2019). Benchmarking evolutionary algorithms for single objective real-valued constrained optimization–a critical review. *Swarm and evolutionary computation*, 44:927–944.

Hengstenberg, R. (1991). Gaze control in the blowfly calliphora: a multisensory, two-stage integration process. *Seminars in Neuroscience*, 3(1):19–29.

Hinson, B. T. and Morgansen, K. A. (2015). Gyroscopic sensing in the wings of the hawkmoth manduca sexta: the role of sensor location and directional sensitivity. *Bioinspiration & biomimetics*, 10(5):056013.

Ho, S., Nassef, H., Pornsinsirirak, N., Tai, Y.-C., and Ho, C.-M. (2003). Unsteady aerodynamics and flow control for flapping wing flyers. *Progress in Aerospace Sciences*, 39(8):635–681.

Hoffmann, J., Donoughe, S., Li, K., Salcedo, M. K., and Rycroft, C. H. (2018). A simple developmental model recapitulates complex insect wing venation patterns. *Proceedings of the National Academy of Sciences*, 115(40):9905–9910.

Holland, J. H. (1992). Genetic algorithms. *Scientific american*, 267(1):66–73.

Hollenbeck, A. and Palazotto, A. (2013). Mechanical characterization of flight mechanism in the hawkmoth manduca sexta. *Experimental Mechanics*, 53:1189–1199.

Huston, S. J. and Jayaraman, V. (2011). Studying sensorimotor integration in insects. *Current Opinion in Neurobiology*, 21(4):527–534.

Ishihara, D., Horie, T., and Denda, M. (2009). A two-dimensional computational study on the fluid–structure interaction cause of wing pitch changes in dipteran flapping flight. *Journal of Experimental Biology*, 212(1):1–10.

Jankauski, M., Casey, C., Heveran, C., Busby, M. K., and Buchmann, S. (2022a). Carpenter bee thorax vibration and force generation inform pollen release mechanisms during floral buzzing. *Scientific Reports*, 12(1):12654.

Jankauski, M., Daniel, T., and Shen, I. (2017). Asymmetries in wing inertial and aerodynamic torques contribute to steering in flying insects. *Bioinspiration & biomimetics*, 12(4):046001.

Jankauski, M., Ferguson, R., Russell, A., and Buchmann, S. (2022b). Structural dynamics of real and modelled solanum stamens: implications for pollen ejection by buzzing bees. *Journal of the Royal Society Interface*, 19(188):20220040.

Jankauski, M., Guo, Z., and Shen, I. (2018). The effect of structural deformation on flapping wing energetics. *Journal of Sound and Vibration*, 429:176–192.

Jankauski, M. and Shen, I. (2014). Dynamic modeling of an insect wing subject to three-dimensional rotation. *International Journal of Micro Air Vehicles*, 6(4):231–251.

Jankauski, M. and Shen, I. (2016). Experimental studies of an inertial-elastic rotating wing in air and vacuum. *International Journal of Micro Air Vehicles*, 8(2):53–63.

Jankauski, M. A. (2018a). Low-order aeroelastic modeling of flapping, flexible wings. In *ASME 2018 International Design Engineering Technical Conferences and Computers and Information in Engineering Conference*, pages V008T10A021–V008T10A021. American Society of Mechanical Engineers.

Jankauski, M. A. (2018b). Passive pitch mechanics of elastic flapping wings. In *Dynamic Systems and Control Conference*, volume 51913, page V003T39A003. American Society of Mechanical Engineers.

Jankauski, M. A. (2020). Measuring the frequency response of the honeybee thorax. *Bioinspiration & Biomimetics*, 15(4):046002.

John D., J. A. (1995). *Computational Fluid Dynamics: The Basics with Applications*. McGraw-Hill Education.

Johns, W., Davis, L., and Jankauski, M. (2020). Reconstructing full-field flapping wing dynamics from sparse measurements. *Bioinspiration & Biomimetics*, 16(1):016005.

Jones, A. B. and Smith, J. M. (2013). Article Title. *Journal Title*, 13(52):123–456.

Jones, M. and Yamaleev, N. (2012). The effect of a gust on the flapping wing performance. In *50th AIAA aerospace sciences meeting including the new horizons forum and aerospace exposition*, page 1080.

Josephson, R. K., Malamud, J. G., and Stokes, D. R. (2000). Asynchronous muscle: a primer. *Journal of Experimental Biology*, 203(18):2713–2722.

Kang, C.-K., Aono, H., Cesnik, C. E., and Shyy, W. (2011). Effects of flexibility on the aerodynamic performance of flapping wings. *Journal of fluid mechanics*, 689:32–74.

Kang, C.-k. and Shyy, W. (2014). Analytical model for instantaneous lift and shape deformation of an insect-scale flapping wing in hover. *Journal of the Royal Society Interface*, 11(101):20140933.

Katz, J. and Plotkin, A. (2001). *Low-speed aerodynamics*, volume 13. Cambridge university press.

Kim, D.-K., Lee, J.-S., and Han, J.-H. (2011). Improved aerodynamic model for efficient analysis of flapping-wing flight. *AIAA journal*, 49(4):868–872.

Kobayashi, M. and Ishikawa, H. (1993). Breakdown of indirect flight muscles of alate aphids (acyrthosiphon pisum) in relation to their flight, feeding and reproductive behavior. *Journal of Insect Physiology*, 39(7):549–554.

Kodali, D. and Kang, C.-k. (2016). An analytical model and scaling of chordwise flexible flapping wings in forward flight. *Bioinspiration & biomimetics*, 12(1):016006.

Kodali, D., Kang, C.-K., and Aono, H. (2017). Analytical aerodynamic model of spanwise flexible flapping wings in forward flight. In *55th AIAA Aerospace Sciences Meeting*, page 0331.

Kou, J. and Zhang, W. (2016). An approach to enhance the generalization capability of nonlinear aerodynamic reduced-order models. *Aerospace Science and technology*, 49:197–208.

Kovacic, I. and Brennan, M. J. (2011). *The Duffing equation: nonlinear oscillators and their behaviour*. John Wiley & Sons.

Kurtulus, D. F. (2011). Introduction to micro air vehicles: concepts, design and applications. *feedback*, 3:5.

Kweon, J. and Choi, H. (2010). Sectional lift coefficient of a flapping wing in hovering motion. *Physics of Fluids*, 22(7):071703.

Lambert, T. (2015). Modeling of aerodynamic forces in flapping flight with the unsteady vortex lattice method. Master's thesis, ULiège-Université de Liège.

Lambora, A., Gupta, K., and Chopra, K. (2019). Genetic algorithm-a literature review. In *2019 international conference on machine learning, big data, cloud and parallel computing (COMITCon)*, pages 380–384. IEEE.

Lang, X., Song, B., Yang, W., and Yang, X. (2022). Effect of wing membrane material on the aerodynamic performance of flexible flapping wing. *Applied Sciences*, 12(9):4501.

Lau, G.-K., Chin, Y.-W., Goh, J. T.-W., and Wood, R. J. (2014). Dipteran-insect-inspired thoracic mechanism with nonlinear stiffness to save inertial power of flapping-wing flight. *IEEE Transactions on Robotics*, 30(5):1187–1197.

Lee, N., Lee, S., Cho, H., and Shin, S. (2018). Effect of flexibility on flapping wing characteristics in hover and forward flight. *Computers Fluids*, 173:111–117.

Lionetti, S., Hedrick, T. L., and Li, C. (2022). Aerodynamic explanation of flight speed limits in hawkmoth-like flapping-wing insects. *Physical Review Fluids*, 7(9):093104.

Liu, H. and Aono, H. (2009). Size effects on insect hovering aerodynamics: an integrated computational study. *Bioinspiration & Biomimetics*, 4(1):015002.

Liu, H., Ellington, C. P., Kawachi, K., van den Berg, C., and Willmott, A. P. (1998). A computational fluid dynamic study of hawkmoth hovering. *Journal of Experimental Biology*, 201(4):461–477.

Liu, L. and Sun, M. (2018). The added mass forces in insect flapping wings. *Journal of theoretical biology*, 437:45–50.

Long, L. N. and Fritz, T. E. (2004). Object-oriented unsteady vortex lattice method for flapping flight. *Journal of Aircraft*, 41(6):1275–1290.

Luo, G. and Sun, M. (2005). The effects of corrugation and wing planform on the aerodynamic force production of sweeping model insect wings. *Acta Mechanica Sinica*, 21(6):531–541.

Lynch, J., Gau, J., Sponberg, S., and Gravish, N. (2021). Dimensional analysis of spring-wing systems reveals performance metrics for resonant flapping-wing flight. *Journal of the Royal Society Interface*, 18(175):20200888.

Maeda, M., Gao, N., Nishihashi, N., and Liu, H. (2010). A free-flight simulation of insect flapping flight. *Journal of Aero Aqua Bio-mechanisms*, 1(1):71–79.

Malatkar, P. (2003). *Nonlinear vibrations of cantilever beams and plates*. PhD thesis, Virginia Tech.

Manohar, K., Brunton, S. L., and Kutz, J. N. (2017). Environment identification in flight using sparse approximation of wing strain. *Journal of Fluids and Structures*, 70:162–180.

Mao, S. and Gang, D. (2003). Lift and power requirements of hovering insect flight. *Acta Mechanica Sinica*, 19(5):458–469.

McLean, D. (2012). *Understanding Aerodynamics: Arguing from the Real Physics*. Aerospace Series. Wiley.

Meng, X., Liu, Y., and Sun, M. (2017). Aerodynamics of ascending flight in fruit flies. *Journal of Bionic Engineering*, 14(1):75–87.

Meng, X. G., Xu, L., and Sun, M. (2011). Aerodynamic effects of corrugation in flapping insect wings in hovering flight. *Journal of Experimental Biology*, 214(3):432–444.

Miller, L. A. and Peskin, C. S. (2009). Flexible clap and fling in tiny insect flight. *Journal of Experimental Biology*, 212(19):3076–3090.

Moore, M. (2014). Analytical results on the role of flexibility in flapping propulsion. *Journal of fluid mechanics*, 757:599–612.

Mountcastle, A. and Daniel, T. (2010). Vortexlet models of flapping flexible wings show tuning for force production and control. *Bioinspiration & biomimetics*, 5(4):045005.

Mountcastle, A. M. and Combes, S. A. (2013). Wing flexibility enhances load-lifting capacity in bumblebees. *Proceedings of the Royal Society B: Biological Sciences*, 280(1759):20130531.

Mueller, T. J. (2001). *Fixed and flapping wing aerodynamics for micro air vehicle applications*. American Institute of Aeronautics and Astronautics.

Mueller, T. J. and JANSEN, JR, B. (1982). Aerodynamic measurements at low reynolds numbers. In *12th Aerodynamic Testing Conference*, page 598.

Nakata, T. and Liu, H. (2012). A fluid–structure interaction model of insect flight with flexible wings. *Journal of Computational Physics*, 231(4):1822–1847.

Nakata, T., Liu, H., and Bomphrey, R. J. (2015). A cfd-informed quasi-steady model of flapping-wing aerodynamics. *Journal of fluid mechanics*, 783:323–343.

Nakata, T., Liu, H., Tanaka, Y., Nishihashi, N., Wang, X., and Sato, A. (2011). Aerodynamics of a bio-inspired flexible flapping-wing micro air vehicle. *Bioinspiration & biomimetics*, 6(4):045002.

Neville, A. (1965). Energy and economy in insect flight. *Science Progress (1933-)*, pages 203–219.

Nguyen, A. T., Kim, J.-K., Han, J.-S., and Han, J.-H. (2016). Extended unsteady vortex-lattice method for insect flapping wings. *Journal of Aircraft*, 53(6):1709–1718.

Nguyen, A. T., Le, V. D. T., Duc, V., et al. (2020a). Study of vertically ascending flight of a hawkmoth model. *Acta Mechanica Sinica*, 36(5):1031–1045.

Nguyen, D. Q., Loianno, G., et al. (2020b). Towards design of a deformable propeller for drone safety. In *2020 3rd IEEE International Conference on Soft Robotics (RoboSoft)*, pages 464–469. IEEE.

Norris, A., Palazotto, A., and Cobb, R. (2010). Structural dynamic characterization of an insect wing. In *51st AIAA/ASME/ASCE/AHS/ASC Structures, Structural Dynamics, and Materials Conference 18th AIAA/ASME/AHS Adaptive Structures Conference 12th*, page 2790.

Norris, A. G., Palazotto, A. N., and Cobb, R. G. (2013). Experimental structural dynamic characterization of the hawkmoth (manduca sexta) forewing. *International Journal of Micro Air Vehicles*, 5(1):39–54.

Obitko, M. (1998). Introduction to genetic algorithms. *Czech Technical University: Prague, Czech Republic*.

O'hara, R. and Palazotto, A. (2012). The morphological characterization of the forewing of the manduca sexta species for the application of biomimetic flapping wing micro air vehicles. *Bioinspiration & biomimetics*, 7(4):046011.

Percin, M., Hu, Y., van Oudheusden, B. W., Remes, B., and Scarano, F. (2011). Wing flexibility effects in clap-and-fling. *International Journal of Micro Air Vehicles*, 3(4):217–227.

Peters, H. J., Goosen, J. F., and van Keulen, F. (2015). Optimal fwmav wing design for a combination of energy-effective hovering and roll control. *International Journal of Micro Air Vehicles*, 7(1):41–53.

Phan, H. V. and Park, H. C. (2019). Insect-inspired, tailless, hover-capable flapping-wing robots: Recent progress, challenges, and future directions. *Progress in Aerospace Sciences*, page 100573.

Phillips, N. and Knowles, K. (2011). Effect of flapping kinematics on the mean lift of an insect-like flapping wing. *Proceedings of the Institution of Mechanical Engineers, Part G: Journal of Aerospace Engineering*, 225:723–736.

Pines, D. J. and Bohorquez, F. (2006). Challenges facing future micro-air-vehicle development. *Journal of aircraft*, 43(2):290–305.

Platzer, M. F., Jones, K. D., Young, J., and Lai, J. C. (2008). Flapping wing aerodynamics: progress and challenges. *AIAA journal*, 46(9):2136–2149.

Pons, A. and Beatus, T. (2022). Distinct forms of resonant optimality within insect indirect flight motors. *Journal of The Royal Society Interface*, 19(190):20220080.

Pornsin-Sirirak, T. N., Tai, Y., Nassef, H., and Ho, C. (2001). Titanium-alloy mems wing technology for a micro aerial vehicle application. *Sensors and Actuators A: Physical*, 89(1-2):95–103.

Pratt, B., Deora, T., Mohren, T., and Daniel, T. (2017). Neural evidence supports a dual sensory-motor role for insect wings. *Proceedings of the Royal Society B: Biological Sciences*, 284(1862):20170969.

Pringle, J. (1949). The excitation and contraction of the flight muscles of insects. *The Journal of physiology*, 108(2):226.

Ramananarivo, S., Godoy-Diana, R., and Thiria, B. (2011). Rather than resonance, flapping wing flyers may play on aerodynamics to improve performance. *Proceedings of the National Academy of Sciences*, 108(15):5964–5969.

Ramesh, K., Gopalarathnam, A., Granlund, K., Ol, M. V., and Edwards, J. R. (2014). Discrete-vortex method with novel shedding criterion for unsteady aerofoil flows with intermittent leading-edge vortex shedding. *Journal of Fluid Mechanics*, 751:500–538.

Rao, S. S. (2007). *Vibration of continuous systems*, volume 464. Wiley Online Library.

Reade, J. and Jankauski, M. (2022). Investigation of chordwise functionally graded flexural rigidity in flapping wings using a two-dimensional pitch-plunge model. *Bioinspiration & Biomimetics*.

Reade, J. and Jankauski, M. A. (2020). Deformable blade element and unsteady vortex lattice fluid-structure interaction modeling of a 2d flapping wing. In *International Design Engineering Technical Conferences and Computers and Information in Engineering Conference*, volume 83969, page V007T07A032. American Society of Mechanical Engineers.

Reid, H., Zhou, H., Maxcer, M., Peterson, R. K., Deng, J., and Jankauski, M. (2021). Toward the design of dynamically similar artificial insect wings. *International Journal of Micro Air Vehicles*, 13:1756829321992138.

Reid, H. E., Schwab, R. K., Maxcer, M., Peterson, R. K., Johnson, E. L., and Jankauski, M. (2019). Wing flexibility reduces the energetic requirements of insect flight. *Bioinspiration & Biomimetics*, 14(5):056007.

Rheuben, M. B. and Kammer, A. (1987). Structure and innervation of the third axillary muscle of manduca relative to its role in turning flight. *Journal of experimental biology*, 131(1):373–402.

Roccia, B. A., Preidikman, S., and Balachandran, B. (2017a). Computational dynamics of flapping wings in hover flight: a co-simulation strategy. *AIAA Journal*, 55(6):1806–1822.

Roccia, B. A., Preidikman, S., Massa, J. C., and Mook, D. T. (2013). Modified unsteady vortex-lattice method to study flapping wings in hover flight. *AIAA journal*, 51(11):2628–2642.

Roccia, B. A., Preidikman, S., Verstraete, M. L., and Mook, D. T. (2017b). Influence of spanwise twisting and bending on lift generation in mav-like flapping wings. *Journal of Aerospace Engineering*, 30(1):04016079.

Ryu, S. and Kim, H. J. (2017). Development of a flapping-wing micro air vehicle capable of autonomous hovering with onboard measurements. In *2017 IEEE/RSJ International Conference on Intelligent Robots and Systems (IROS)*, pages 3239–3245. IEEE.

San Ha, N., Truong, Q. T., Goo, N. S., and Park, H. C. (2013). Relationship between wingbeat frequency and resonant frequency of the wing in insects. *Bioinspiration & biomimetics*, 8(4):046008.

Sane, S. P. (2003). The aerodynamics of insect flight. *Journal of experimental biology*, 206(23):4191–4208.

Sane, S. P. and Dickinson, M. H. (2002). The aerodynamic effects of wing rotation and a revised quasi-steady model of flapping flight. *Journal of experimental biology*, 205(8):1087–1096.

Sane, S. P., Dieudonné, A., Willis, M. A., and Daniel, T. L. (2007). Antennal mechanosensors mediate flight control in moths. *Science*, 315(5813):863–866.

Santhanakrishnan, A., Robinson, A. K., Jones, S., Low, A. A., Gadi, S., Hedrick, T. L., and Miller, L. A. (2014). Clap and fling mechanism with interacting porous wings in tiny insect flight. *Journal of Experimental Biology*, 217(21):3898–3909.

Schmitz, S. (2020). *Aerodynamics of wind turbines: a physical basis for analysis and design*. John wiley & sons.

Schwab, R., Johnson, E., and Jankauski, M. (2019a). A novel fluid–structure interaction framework for flapping, flexible wings. *Journal of Vibration and Acoustics*, 141(6):061002.

Schwab, R., Johnson, E., and Jankauski, M. (2021). Reduced-order modeling and the physics governing flapping wing fluid-structure interaction. *bioRxiv*.

Schwab, R., Reade, J., and Jankauski, M. (2022). Quasi three-dimensional deformable blade element and unsteady vortex lattice reduced-order modeling of fluid–structure interaction in flapping wings. *Physics of Fluids*, 34(12).

Schwab, R., Reid, H., and Jankauski, M. (2019b). Reduced-order modeling and experimental studies of two-way coupled fluid-structure interaction in flapping wings. In *ASME 2019 International Design Engineering Technical Conferences and Computers and Information in Engineering Conference*. American Society of Mechanical Engineers Digital Collection.

Schwab, R. K., Reid, H. E., and Jankauski, M. (2020). Reduced-order modeling and experimental studies of bilaterally coupled fluid-structure interaction in single-degree-of-freedom flapping wings (in press). *Journal of Vibration and Acoustics*.

Sedov, L. I., Chu, C., Cohen, H., Seckler, B., and Gillis, J. (1965). Two-dimensional problems in hydrodynamics and aerodynamics. *Physics Today*, 18(12):62.

Shahzad, A., Tian, F.-B., Young, J., and Lai, J. C. (2018). Effects of flexibility on the hovering performance of flapping wings with different shapes and aspect ratios. *Journal of Fluids and Structures*, 81:69–96.

Shen, C., Liu, Y., and Sun, M. (2018). Lift and power in fruitflies in vertically-ascending flight. *Bioinspiration & biomimetics*, 13(5):056008.

Shyy, W., Aono, H., Chimakurthi, S. K., Trizila, P., Kang, C.-K., Cesnik, C. E., and Liu, H. (2010). Recent progress in flapping wing aerodynamics and aeroelasticity. *Progress in Aerospace Sciences*, 46(7):284–327.

Shyy, W., Berg, M., and Ljungqvist, D. (1999). Flapping and flexible wings for biological and micro air vehicles. *Progress in aerospace sciences*, 35(5):455–505.

Shyy, W. and Liu, H. (2007). Flapping wings and aerodynamic lift: the role of leading-edge vortices. *AIAA journal*, 45(12):2817–2819.

Silva, R. C. and Bueno, D. D. (2024). On the dynamics of flexible wings for designing a flapping-wing uav. *Drones*, 8(2):56.

Smith, J. M. and Jones, A. B. (2012). *Book Title*. Publisher, 7th edition.

Sridhar, M. and Kang, C.-k. (2015). Aerodynamic performance of two-dimensional, chordwise flexible flapping wings at fruit fly scale in hover flight. *Bioinspiration & biomimetics*, 10(3):036007.

Srygley, R. and Thomas, A. (2002). Unconventional lift-generating mechanisms in free-flying butterflies. *Nature*, 420(6916):660–664.

Stanford, B., Kurdi, M., Beran, P., and McClung, A. (2012). Shape, structure, and kinematic parameterization of a power-optimal hovering wing. *Journal of Aircraft*, 49(6):1687–1699.

Taha, H. E., Hajj, M. R., and Beran, P. S. (2014). State-space representation of the unsteady aerodynamics of flapping flight. *Aerospace Science and Technology*, 34:1–11.

Takizawa, K., Tezduyar, T. E., and Kostov, N. (2014). Sequentially-coupled space–time fsi analysis of bio-inspired flapping-wing aerodynamics of an mav. *Computational Mechanics*, 54(2):213–233.

Tanaka, H. and Wood, R. J. (2010). Fabrication of corrugated artificial insect wings using laser micromachined molds. *Journal of Micromechanics and Microengineering*, 20(7):075008.

Tang, J., Chimakurthi, S., Palacios, R., Cesnik, C., and Shyy, W. (2008). Computational fluid-structure interaction of a deformable flapping wing for micro air vehicle applications. In *46th AIAA Aerospace Sciences Meeting and Exhibit*, page 615.

Tang, L., Paı, M. P., et al. (2007). On the instability and the post-critical behaviour of two-dimensional cantilevered flexible plates in axial flow. *Journal of Sound and Vibration*, 305(1-2):97–115.

Terze, Z., Pandža, V., Andrić, M., and Zlatar, D. (2022). Reduced coupled flapping wing-fluid computational model with unsteady vortex wake. *Nonlinear dynamics*, 109(2):975–987.

Tian, F.-B., Dai, H., Luo, H., Doyle, J. F., and Rousseau, B. (2014). Fluid–structure interaction involving large deformations: 3d simulations and applications to biological systems. *Journal of computational physics*, 258:451–469.

Tian, F.-B., Luo, H., Song, J., and Lu, X.-Y. (2013). Force production and asymmetric deformation of a flexible flapping wing in forward flight. *Journal of Fluids and Structures*, 36:149–161.

Traub, L. W. and Coffman, C. (2019). Efficient low-reynolds-number airfoils. *Journal of Aircraft*, 56(5):1987–2003.

Trimmer, W. S. (1989). Microrobots and micromechanical systems. *Sensors and actuators*, 19(3):267–287.

Tu, M. S. and Daniel, T. L. (2004). Submaximal power output from the dorsolongitudinal flight muscles of the hawkmoth manduca sexta. *Journal of Experimental Biology*, 207(26):4651–4662.

Tu, Z., Fei, F., Zhang, J., and Deng, X. (2019). Acting is seeing: Navigating tight space using flapping wings. In *2019 International Conference on Robotics and Automation (ICRA)*, pages 95–101. IEEE.

Usherwood, J. R. and Ellington, C. P. (2002). The aerodynamics of revolving wings i. model hawkmoth wings. *Journal of Experimental biology*, 205(11):1547–1564.

Valdez, M. F., Balachandran, B., and Preidikman, S. (2020). Comparative study on analytical and computational aerodynamic models for flapping wings mavs. *The Aeronautical Journal*, 124(1280):1636–1665.

Vanella, M., Fitzgerald, T., Preidikman, S., Balaras, E., and Balachandran, B. (2009). Influence of flexibility on the aerodynamic performance of a hovering wing. *Journal of Experimental Biology*, 212(1):95–105.

Vest, M. S. and Katz, J. (1996). Unsteady aerodynamic model of flapping wings. *AIAA journal*, 34(7):1435–1440.

Vincent, J. and Wegst, U. (2004). Design and mechanical properties of insect cuticle. *Arthropod structure & development*, 33 3:187–99.

Walker, J. A. (2002). Rotational lift: something different or more of the same? *Journal of Experimental Biology*, 205(24):3783–3792.

Walker, S. M. and Taylor, G. K. (2021). A semi-empirical model of the aerodynamics of manoeuvring insect flight. *Journal of the Royal Society Interface*, 18(177):20210103.

Wang, H., Zeng, L., Liu, H., and Yin, C. (2003). Measuring wing kinematics, flight trajectory and body attitude during forward flight and turning maneuvers in dragonflies. *Journal of Experimental Biology*, 206(4):745–757.

Wang, Q., Goosen, J., and van Keulen, F. (2017). An efficient fluid–structure interaction model for optimizing twistable flapping wings. *Journal of Fluids and Structures*, 73:82–99.

Wang, Z. J. (2005). Dissecting insect flight. *Annu. Rev. Fluid Mech.*, 37(1):183–210.

Wang, Z. J., Birch, J. M., and Dickinson, M. H. (2004). Unsteady forces and flows in low reynolds number hovering flight: two-dimensional computations vs robotic wing experiments. *Journal of Experimental Biology*, 207(3):449–460.

Ward, T. A., Fearday, C. J., Salami, E., and Binti Soin, N. (2017). A bibliometric review of progress in micro air vehicle research. *International Journal of Micro Air Vehicles*, 9(2):146–165.

Warrick, D. R., Tobalske, B. W., and Powers, D. R. (2005). Aerodynamics of the hovering hummingbird. *Nature*, 435(7045):1094–1097.

Whitney, J. P. and Wood, R. J. (2010). Aeromechanics of passive rotation in flapping flight. *Journal of Fluid Mechanics*, 660:197–220.

Willis, D., Israeli, E., Persson, P.-O., Drela, M., Peraire, J., Swartz, S., and Breuer, K. (2007). A computational framework for fluid structure interaction in biologically inspired flapping flight. In *25th AIAA Applied Aerodynamics Conference*, page 3803.

Willmott, A. P. and Ellington, C. P. (1997a). The mechanics of flight in the hawkmoth manduca sexta. i. kinematics of hovering and forward flight. *The Journal of experimental biology*, 200(21):2705–2722.

Willmott, A. P. and Ellington, C. P. (1997b). The mechanics of flight in the hawkmoth manduca sexta. ii. aerodynamic consequences of kinematic and morphological variation. *The Journal of experimental biology*, 200(21):2723–2745.

Willmott, A. P., Ellington, C. P., and Thomas, A. L. (1997). Flow visualization and unsteady aerodynamics in the flight of the hawkmoth, manduca sexta. *Philosophical Transactions of the Royal Society of London. Series B: Biological Sciences*, 352(1351):303–316.

Winslow, J., Otsuka, H., Govindarajan, B., and Chopra, I. (2018). Basic understanding of airfoil characteristics at low reynolds numbers (10 4–10 5). *Journal of aircraft*, 55(3):1050–1061.

Wold, E. S., Lynch, J., Gravish, N., and Sponberg, S. (2023). Structural damping renders the hawkmoth exoskeleton mechanically insensitive to non-sinusoidal deformations. *Journal of the Royal Society Interface*, 20(202):20230141.

Wood, R., Nagpal, R., and Wei, G.-Y. (2013). Flight of the robobees. *Scientific American*, 308(3):60–65.

Wootton, R. J. (1981). Support and deformability in insect wings. *Journal of Zoology*, 193(4):447–468.

Xiao, Q. and Zhu, Q. (2014). A review on flow energy harvesters based on flapping foils. *Journal of fluids and structures*, 46:174–191.

Xiao, S., Hu, K., Huang, B., Deng, H., and Ding, X. (2021). A review of research on the mechanical design of hoverable flapping wing micro-air vehicles. *Journal of Bionic Engineering*, 18:1235–1254.

Yamada, T. and Yoshimura, S. (2008). Line search partitioned approach for fluid-structure interaction analysis of flapping wing. *Computer Modeling in Engineering and Sciences*, 24(1):51.

Yi-Bao, C., Wang, Z.-K., and Tsai, G.-C. (2015). Two-way fluid-structure interaction simulation of a micro horizontal axis wind turbine. *International Journal of Engineering and Technology Innovation*, 5(1):33.

Yin, B. and Luo, H. (2010). Effect of wing inertia on hovering performance of flexible flapping wings. *Physics of Fluids*, 22(11):111902.

Young, J., Walker, S. M., Bomphrey, R. J., Taylor, G. K., and Thomas, A. L. (2009). Details of insect wing design and deformation enhance aerodynamic function and flight efficiency. *Science*, 325(5947):1549–1552.

Zakaria, M. Y. (2021). Unsteady aerodynamics of highly maneuvering flyers. In *Biomimetics*. IntechOpen.

Zheng, L., Hedrick, T. L., and Mittal, R. (2013). A multi-fidelity modelling approach for evaluation and optimization of wing stroke aerodynamics in flapping flight. *Journal of Fluid Mechanics*, 721:118–154.

Zhu, Q. (2011). Optimal frequency for flow energy harvesting of a flapping foil. *Journal of fluid mechanics*, 675:495–517.

Zhu, Q. and Peng, Z. (2009). Mode coupling and flow energy harvesting by a flapping foil. *Physics of Fluids*, 21(3):033601.

Zufferey, R., Tormo-Barbero, J., Guzmán, M. M., Maldonado, F. J., Sanchez-Laulhe, E., Grau, P., Pérez, M., Acosta, J. Á., and Ollero, A. (2021). Design of the high-payload flapping wing robot e-flap. *IEEE Robotics and Automation Letters*, 6(2):3097–3104.

Zuo, D., Peng, S., Chen, W., and Zhang, W. (2007). Numerical simulation of flapping-wing insect hovering flight at unsteady flow. *International Journal for numerical methods in fluids*, 53(12):1801–1817.